

AN ABSTRACT OF THE THESIS OF

Nicholas C. Cappello for the degree of Master of Science in Mechanical Engineering
presented on August 15, 2013.

Title: The Experimental Characterization of Membrane Behavior in Two-phase
Gas Extraction

Abstract approved: _____

Deborah V. Pence

James A. Liburdy

Understanding the behavior of hydrophobic membranes is important for applications where separating a gas from a liquid-gas mixture is beneficial. For example, *in-situ* vapor extraction can be used in microscale heat sinks to improve heat transfer and flow stability. In this study, gas is experimentally evaluated flowing through flexible polytetrafluoroethylene nanofiber membranes. The gas is extracted from liquid-gas combinations of liquid water, water vapor and air. For single-phase flow such as superheated vapor and air, an applied pressure difference across the membrane results in structural changes affecting properties including the membrane thickness, which restricts the flow rate. Two existing models predicting fluid transport in porous media are found to be insufficient to predict gas extraction flow rates from two-phase mixtures, even when accounting for membrane compaction and a proposed estimated reduced extraction area. The proposed estimated extraction area insufficiently accounts for bubble kinetic energy, bubble dynamics and the existence of thin liquid

films. The thin liquid film must be ruptured to open membrane pores to extract the gas in the bubbles. At greater applied pressure differences, film rupture and three phase contact are accelerated and bubbles are extracted more quickly resulting in a reduced gas-membrane contact area. If the bubbles have too much energy associated with them, it may take multiple collisions with the membrane for the bubbles to establish stable three phase contact. To account for the hydrodynamics near the membrane surface, empirical parameters are developed as a function of thermophysical properties of the mixture near the membrane and the applied pressure differences across the membrane. In the case of liquid-air mixtures with high void fractions, bubbles are not completely extracted due to hydrodynamics near the membrane surface. For saturated liquid-vapor studies, full vapor extraction is achieved even at high void fractions due to different bubble energy and behavior than the liquid-air studies. One implication with liquid-vapor mixtures is that changes in the membrane flow resistance can be induced if the extraction vacuum pressure is cycled.

© Copyright by Nicholas C. Cappello
August 15, 2013
All Rights Reserved

The Experimental Characterization of Membrane Behavior in
Two-phase Gas Extraction

by

Nicholas C. Cappello

A THESIS

submitted to

Oregon State University

in partial fulfillment of
the requirements for the
degree of

Master of Science

Presented August 15, 2013
Commencement June 2014

Master of Science thesis of Nicholas C. Cappello presented on August 15, 2013.

APPROVED:

Co-Major Professor, representing Mechanical Engineering

Co-Major Professor, representing Mechanical Engineering

Head of the School of Mechanical, Industrial, and Manufacturing Engineering

Dean of the Graduate School

I understand that my thesis will become part of the permanent collection of Oregon State University libraries. My signature below authorizes release of my thesis to any reader upon request.

Nicholas C. Cappello, Author

ACKNOWLEDGEMENTS

Without the guidance of my advisors Dr. Deborah Pence and Dr. James Liburdy, I would not have been able to produce this thesis; aside from aiding in the production of this work, I am glad to have worked under Deb and Jim because they gave me the freedom to broaden my horizons. I would like to thank my parents because I am slowly realizing how difficult it is to balance a career and a lifestyle, yet you have always been there for me; I hope you see your values in me. I am grateful for the Milosh & Jeanne Popovich Fellowship, the Arthur E. Hitsman Student Excellence fund and financial support from the Office of Naval Research. I would like to thank my colleagues for their positivity, encouragement and help over the past two years. I would also like to thank Jerry Jones of J&J Porous Metals, Jim Temple of 3M, Mark Varney of American Durafilm as well as Nancy Trogani and Tom Hoffmann of GE - you made my time at OSU that much easier! Finally, I'd like to thank the teachers, professors and managers of my past for without you I would not have made the decisions I did. I look forward to thanking my friends by being around more!

TABLE OF CONTENTS

	<u>Page</u>
1 Introduction	1
1.1 Motivation	2
1.2 Background	2
2 Literature Review	5
2.1 Application of Hydrophobic Membranes	5
2.1.1 Single-phase Transport	6
2.1.2 Two-phase Separation	8
2.2 Physics of the Liquid-gas Interface	9
2.2.1 Laplace Equation	10
2.2.2 Contact Angle	12
2.3 Gas Transport Physics	15
2.3.1 Phenomena Limiting Gas Transport	16
2.3.2 Porous Media Flow Models	19
2.3.3 Three Phase Contact Models	25
2.4 Major Conclusions of Two-phase Vapor Extraction Studies	26
3 Problem Statement and Approach	28
3.1 Study of Single-phase Gas Flow	29
3.2 Study of Two-phase Gas Extraction	31
4 Experimental Apparatuses and Procedures	34
4.1 Properties of the Membrane	35
4.2 Extraction Chamber	38
4.3 Single-phase Experiments	39
4.3.1 Air Apparatus	40
4.3.2 Vapor Apparatus	40
4.4 Two-phase Experiments	42
4.4.1 Liquid-Vapor Apparatus	42
4.4.2 Liquid-Air Apparatus	44
4.5 Procedures	48
4.5.1 Pre-test Operations	49
4.5.2 Single-phase Air	52

TABLE OF CONTENTS (Continued)

	Page
4.5.3 Single-phase Vapor	53
4.5.4 Liquid-Vapor	55
4.5.5 Liquid-Air	59
4.6 Cases Studied	62
4.7 Thermo-physical Fluid Properties	63
5 Data Reduction and Analysis	64
5.1 Gas Available For Extraction	65
5.2 Extracted Gas	69
5.3 Trans-membrane Pressure Drop	73
5.4 Pressure Cycles	75
5.5 Existing Model Modifications for Single-phase Flow	77
5.5.1 Darcy Permeability	79
5.5.2 Membrane Compaction	81
5.6 Existing Model Modifications for Two-phase Gas Extraction	84
5.6.1 Theoretical Effective Extraction Area	85
5.6.2 Empirical Effective Extraction Area	87
5.7 Image Analysis	88
6 Results and discussion	90
6.1 Existing Model Validation for Single-Phase Flow	91
6.1.1 Darcy's Law	91
6.1.2 Dusty Gas Model	97
6.2 Modified Models for for Two-phase Gas Extraction	101
6.2.1 Darcy's Law	103
6.2.2 Dusty Gas Model	110
6.3 Generalized Models for Two-phase Gas Extraction	113
6.3.1 Model Considerations	114
6.3.2 Modified Dusty Gas Model	130
6.3.3 Modified Darcy's Law	140
6.4 Constraints of Generalized Models	146
6.4.1 Summary of Non-dimensional Models	159
6.4.2 Recommended Models	163

TABLE OF CONTENTS (Continued)

	<u>Page</u>
7 Conclusions	167
8 Recommendations	170
Bibliography	172
Appendices	178

LIST OF FIGURES

Figure	Page
2.1 Sketch of the meniscus geometry assumptions applied to Eq. (2.2) showing the original (dashed line) and deformed (solid line) meniscus shape with applied pressure difference across the liquid-gas interface representing (a) the actual meniscus deformation and (b) the assumed spherical meniscus deformation. Gas is in the pore and is shown shaded and the pore wall is shown hatched.	11
2.2 Sketch of the contact angle of a liquid drop on a solid surface surrounded by gas, as measured with the Sessile drop method.	13
3.1 Representation of reduced porosity as a result of compaction	30
3.2 Representation of reduced tortuosity as a result of compaction	31
3.3 Representation of reduced porosity as a result of droplet entrapment, arrows represent gas streamlines, circles represent trapped liquid drops and the mesh represents the pore structure.	32
4.1 Photograph of the PP scrim backing which supports the PTFE nanofibers laminated to it, the PTFE is the material in the ovals. Image is about 3.2 mm wide, viewed with an optical microscope.	35
4.2 Scanning electron microscope image of $0.45\mu m$ diameter pore size. The width of the image, the horizontal field width (HFW), is $10.2\mu m$. . .	36
4.3 Scanning electron microscope image of $0.45\mu m$ diameter pore size. The width of the image (HFW) is $2.33\mu m$	37
4.4 Photograph of the extraction chamber with window removed showing NiCr heater coils to keep the gas from condensing. The smaller compression fittings spaced about 120° from each other are holding the heater coil. Only one compression fitting is used for thermocouple mounting (not shown).	38
4.5 Drawing of the superheated vapor and single-phase air apparatus geometry, shown to scale but shown smaller than actual size.	39
4.6 Photograph of the superheated vapor apparatus.	41
4.7 Cross-section of the liquid-vapor apparatus, shown to scale.	43

LIST OF FIGURES (Continued)

Figure	Page
4.8 Photograph of the upper half of the liquid-vapor apparatus in operation, liquid supply is on the right and excess is on the left.	43
4.9 Drawing of the liquid-air apparatus cross-section, shown to scale but smaller than actual size.	44
4.10 Photograph of the liquid-air apparatus main block. The top hole press fits the membrane around the extraction chamber (pin).	45
4.11 Photograph of the liquid-air apparatus showing membrane visibility from the front window allowing high speed camera to focus on the face of the membrane.	46
4.12 Photograph of the liquid-air apparatus in operation, excess liquid drips out of the reservoir.	46
4.13 Photograph of the relative humidity sensor and mounting chamber for in-line measurement of vapor content in air.	47
4.14 Photograph of the membrane support shown adhered to the shoulder of the extraction chamber as seen in Fig. 4.15. Also showing Teflon [®] tape which mates to the scrim integrated backing of the membrane.	48
4.15 Schematic of the membrane mounting method showing the hole and pin forming a press fit to mount the membrane.	49
4.16 Photograph of the extraction chamber after removal from an apparatus to show membrane press fit and vacuum grease on shoulder.	51
4.17 Schematic of the single-phase air flow loop.	52
4.18 Single-phase superheated vapor flow loop	54

LIST OF FIGURES (Continued)

Figure	Page
4.19 Photographs of liquid-vapor extraction chamber showing water on the porous support, this condition only existed in transients between data points; the liquid had to be evaporated before capturing steady state data. The extraction chamber thermocouple is shown protruding into the chamber (out of focus). (a) Reference image for point of view; note that liquid drops on the window only showed up when there was a small pool of liquid; (b) start-up condition if extraction heater is not turned on prior to extracting vapor; (c) liquid layer at the perimeter of the support.	56
4.20 Schematic of the liquid-vapor flow loop.	57
4.21 Photograph of the liquid-vapor apparatus in operation showing the extraction pressure transducer in a location which results in drops of water on the membrane support.	58
4.22 Photograph of the liquid-air apparatus in operation showing sensors and power supplies, measuring extracted air with flow meter transducer upstream of a rotameter.	60
4.23 Schematic of the liquid-air flow loop; single-phase air flow loop is similar but does not include desiccant filters or 0.01 μm filter (just 1 μm filter).	61
5.1 Extraction volume flow rate of air as a function of time calculated with an image analysis program of a video of the rotameter output.	71
5.2 Pressure difference across the membrane support with curve fit of the form in Eq. (5.17). (a) Room temperature air $C_{1,sup} = 1.17 \times 10^{-2} \text{ min/g}$, $C_{2,sup} = 3.86 \times 10^{-1} \text{ min}^2/\text{g}^2$ (b) Saturated vapor $C_{1,sup} = 1.81 \times 10^{-2} \text{ min/g}$, $C_{2,sup} = 6.92 \times 10^{-1} \text{ min}^2/\text{g}^2$	74
5.3 Single-phase air data showing the pressure drop across the support (dash-dot line) and the pressure drop across the active layer of membrane (PTFE), \square	75
5.4 Knudsen number as a function of pressure difference across the membrane where the high pressure side is at 1 atm.	79
6.1 Single-phase empirical Darcy values for air: (a) Darcy permeability $\bar{K}_D = 7.5 \times 10^{-15} \text{ m}^2$ and (b) Darcy resistance $\bar{R}_D = 2.1 \times 10^9 \text{ 1/m}$	92

LIST OF FIGURES (Continued)

Figure	Page
6.2 Single-phase superheated vapor Darcy values (“x” markers) superimposed with single-phase air (“+” markers): (a) Darcy permeability $\bar{K}_D = 6.2 \times 10^{-15} \text{ m}^2$ and (b) Darcy resistance $\bar{R}_D = 2.5 \times 10^9 \text{ 1/m}$. . .	93
6.3 Single-phase air flow rate measured data (“+” markers) and predictions using Darcy’s Law Eq. (2.9) with constant permeability and membrane thickness (solid line).	94
6.4 (a) Single-phase air flow rate predictions using Darcy’s Law with constant permeability and membrane thickness (solid line) and accounting for compaction (dashed line) with $\delta'_{D,air} = 2.7 \times 10^{-9} \text{ m/kPa}$; (b) resultant reduction in thickness with increasing pressure difference.	95
6.5 Single-phase superheated vapor predictions using Darcy’s Law Eq. (2.9) (a) mass flow rate with constant permeability and membrane thickness (solid line) and accounting for compaction (dashed line) with $\delta'_{D,vap} = 2.25 \times 10^{-8} \text{ m/kPa}$ and (b) membrane thickness (dashed line) and that for air (solid line)	96
6.6 (a) Measured single-phase air data (“+” markers) compared to predictions using the dusty gas model not accounting for compaction (solid line) Eq. (2.19) and accounting for compaction (dashed line) where $\delta'_{air} = 4.0 \times 10^{-8} \text{ m/kPa}$ and (b) resulting membrane thickness versus pressure differential.	98
6.7 Single-phase superheated vapor flow rate predictions using the dusty gas model (a) not accounting for compaction (solid line) Eq. (2.19) and accounting for compaction (dashed line) with $\delta'_{vap} = 1.35 \times 10^{-7} \text{ m/kPa}$ and (b) membrane thickness (dashed line) and that for air (solid line).	99
6.8 Predicted membrane thickness based on Darcy’s Law (thin lines) and the DGM (thick lines) for superheated vapor (dashed line) and air (solid line); curves are defined by Eq. (5.20).	101
6.9 Two-phase Darcy permeabilities: (a) Liquid-air and (b) Liquid-vapor; symbols correspond to Table 6.1 on pg. 90.	104
6.10 Two-phase Darcy resistances: (a) Liquid-air and (b) Liquid-vapor; symbols correspond to Table 6.1 on pg. 90.	105

LIST OF FIGURES (Continued)

Figure	Page
6.11 Liquid-vapor flow rate predictions from Darcy’s Law accounting for compaction with Eq. (5.20) where $\delta' = \delta'_{D,vap}$ and flow area is scaled by the annular Armand-corrected void fraction; symbols correspond to Table 6.1 on pg. 90.	107
6.12 Liquid-air flow rate predictions from Darcy’s Law accounting for compaction with Eq. (5.20) where $\delta' = \delta'_{D,air}$ and the flow area is scaled by the annular Armand-corrected void fraction α_{AA} listed in Table 6.5; symbols correspond to Table 6.1 on pg. 90.	109
6.13 Liquid-vapor flow rate predictions from the dusty gas model accounting for compaction with Eq. (2.19) and Eq. (5.20) where $\delta' = \delta'_{vap}$ and flow area is scaled by the annular Armand-corrected void fraction; symbols correspond to Table 6.1 on pg. 90.	111
6.14 Liquid-air flow rate predictions from the dusty gas model accounting for compaction with Eq. (2.19) and Eq. (5.20) where $\delta' = \delta'_{air}$ and flow area is scaled by the annular Armand-corrected void fraction α_{AA} listed in Table 6.5; symbols correspond to Table 6.1 on pg. 90.	112
6.15 Two-phase images at the maximum pressure difference in the first cycle of each data case from high speed video scaled consistently: horizontal field of view is 15 mm. (a)-(e) are liquid-vapor and (f)-(i) are liquid-air; the grid lines are the outlines of the membrane ribs underneath the PTFE laminate, only visible because of the applied pressure difference across the membrane. Note that camera angle varies for each case. . .	117
6.16 Air bubble interaction with membrane; images are from 0.26 g/min liquid-air case with 32 kPa pressure difference across membrane. Gravity is in the negative y-direction perpendicular to the face of the membrane. See Table 6.7 for a detailed description of collision times. . . .	119
6.17 Air bubble forming an immobile air pocket with another bubble approaching colliding, image is from 0.26 g/min liquid-air case with 1 kPa pressure difference across membrane.	121
6.18 Filled data points are those considered to determine the two-phase extraction area correction term Φ_m for (a) liquid-vapor and (b) liquid-air. Criteria for selected data points is to be less than 90% of the experimental plateau, including the next point.	126

LIST OF FIGURES (Continued)

Figure	Page
6.19 Extraction area correction term Φ_m^* as a function of void fraction: (a) exponential curve fit of the form Eq. (6.4) with $C = 1.7 \times 10^6$ and $n = -4$ (b) applied to liquid-vapor (c) applied to liquid-air and (d) compared to measured data with a $\pm 25\%$ error band. Symbols correspond to Table 6.9 on pg. 129.	132
6.20 Extraction area correction term Φ_m^* as a function of pressure: (a) exponential curve fit of the form Eq. (6.5) with $C = 7$ and $n = 0.4$ (b) applied to liquid-vapor (c) applied to liquid-air and (d) compared to measured data with a $\pm 25\%$ error band. Note: top solid line in (b) is the prediction for the “o” markers. Symbols correspond to Table 6.9 on pg. 129.	135
6.21 Extraction area correction term Φ_m^* as a function of pressure: (a) exponential curve fit of the form Eq. (6.5) with $C = 9 \times 10^{11}$ and $n = 0.36$ (b) applied to liquid-vapor (c) applied to liquid-air and (d) compared to measured data with a $\pm 25\%$ error band. Note: the top solid line in (b) corresponds to the “o” markers and the dash-dot line corresponds to the “□” markers. Symbols correspond to Table 6.9 on pg. 129. . .	137
6.22 Extraction area correction term Φ_m^* as a function of pressure: (a) exponential curve fit of the form Eq. (6.5) with $C = 2.8 \times 10^{-3}$ and $n = 0.34$ (b) applied to liquid-vapor (c) applied to liquid-air and (d) compared to measured data with a $\pm 25\%$ error band. Symbols correspond to Table 6.9 on pg. 129.	139
6.23 Darcy’s Law best fit area correction term scaled with the same variables which collapsed the two-phase DGM data in Fig. 6.22a.	141
6.24 Extraction area correction term Eq. (6.10) as a function of pressure: (a) exponential curve fit of the form Eq. (6.4) with $C = 4.1$ and $n = 0.09$ (b) applied to liquid-vapor (c) applied to liquid-air and (d) compared to measured data with a $\pm 25\%$ error band. Symbols correspond to Table 6.9 on pg. 129.	142
6.25 Liquid-vapor and liquid-air data scaled according to Eq. (6.11). Scaling values shown in Table 6.9, curve fit defined by Eq. (6.5) with $C = 2.7 \times 10^{-3}$ and $n = 0.32$. Symbols correspond to Table 6.9 on pg. 129.	144

LIST OF FIGURES (Continued)

Figure	Page
6.26 Darcy's Law <i>without compaction or area corrections</i> scaled according to Eq. (6.11). Showing measured and curve fit values for (a) and (b) liquid-vapor and (c) and (d) liquid-air. (a) and (c) are permeability and (b) and (d) are extracted mass flow rate. Symbols correspond to Table 6.9 on pg. 129.	145
6.27 Non-dimensional two-phase permeability as a function of pressure compared to measured data with a $\pm 25\%$ error band. Symbols correspond to Table 6.9 on pg. 129.	146
6.28 Sketches of observed cycling effects: (a) No cycling effects, bubble dynamics and reduced gas-membrane area in two-phase experiments (b) Temporary cycling effects, $\uparrow \Delta P$ cycles disregarded, determined to be caused by apparatus geometry (c) Permanent cycling effects, likely due to droplet entrapment and/or condensation.	147
6.29 All single-phase pressure cycling data, gas extraction versus applied pressure difference. Symbols correspond to Table 6.10.	148
6.30 Effects of pressure cycling for all liquid-air data for the following mass flow rate of available humid air (g/min): (a) 0.13 (b) 0.26 (c) 1.67 and (d) 2.37. Symbols correspond to Table 6.10 on pg. 148.	149
6.31 Total <i>water species (vapor)</i> in the extracted humid air minus the available vapor mass flow rate measured in the gas supply line versus applied pressure difference. Symbols correspond to Table 6.10 on pg. 148. Available humid mass flow rates of humid air are (g/min): (a) 0.13 (b) 0.26 (c) 1.67 and (d) 2.37	151
6.32 All liquid-vapor pressure cycling data, gas extraction versus applied pressure difference for the following mass flow rate of available vapor (g/min): (a) 0.26 (b) 0.72 (c) 0.98 (d) 1.38 and (e) 1.55. Symbols correspond to Table 6.10 on pg. 148.	154
6.33 1.38 g/min available vapor cycling reproduced	155
6.34 Darcy's Law extraction predictions using Eq. (6.12) showing the impact of (a) omitting and (b) including the full extraction criteria as defined by the maximum extraction rate in (a) or the available gas flow rate, whichever is lower.	166

LIST OF TABLES

<u>Table</u>	<u>Page</u>
4.1 Membrane properties and other details about the membrane stack-up.	38
4.2 Single-phase and two-phase cases, some cells are empty because these variables are not applicable to the specific data case. Values are averaged over all data points in test.	62
4.3 Thermophysical properties at nominal temperatures.	63
5.1 Contact angle and liquid entry pressure of 0.45 μm pore diameter PTFE membranes.	77
5.2 Flow regime ranges to determine contributing interactions which resist gas transport through membrane. Mean free path is calculated at 1 atm.	78
6.1 List of symbols and their corresponding data cases used in figures . .	90
6.2 Summary of single-phase mean Darcy values based on Eq. (2.9) . . .	94
6.3 Summary of single-phase Darcy values assuming a mean permeability and accounting for compaction	97
6.4 Summary of single-phase results using the dusty gas model, Eq. (2.19), accounting for membrane compaction and holding thickness constant.	100
6.5 Armand-corrected void fraction for all two-phase experiments, calculated with Eq. (5.32).	103
6.6 Bubble diameters and void fraction for all two-phase experiments. Note: the 0.26 g/min available vapor case disregards tiny bubbles from the mean bubble diameter calculation, these can be seen in the background of Fig. 6.15a	118
6.7 Bubble collision times corresponding to Fig. 6.16	119
6.8 Experimental plateau as determined from Eq. (6.2) compared to the theoretical plateau i.e. the available gas.	126
6.9 Select mixture-specific thermophysical properties used to collapse data presented with a repeated list of symbols from Table 6.1.	129
6.10 New list of symbols for cycling data.	148

LIST OF TABLES (Continued)

Table	Page
6.11 MAE of extraction predictions comparing the effects of compaction with no reduced area. MAE percent values are in bold, are <i>only representative of data in the partial extraction region</i> and exclude data points with measured pressure differences less than 0.5 kPa.	160
6.12 MAE of non-dimensional extraction predictions accounting for compaction and reduced area. MAE percent values are in bold, are <i>only representative of data in the partial extraction region</i> and exclude data points with measured pressure differences less than 0.5 kPa. Non-dimensional area correction models are in the Φ_m^* column.	161
6.13 MAE of non-dimensional extraction predictions accounting for compaction and reduced area. MAE percent values are in bold, are <i>representative of data in the partial and full extraction regions</i> and exclude data points with measured pressure differences less than 1.5 kPa. Non-dimensional area correction models are in the Φ_m^* column.	162
6.14 Summary of non-dimensional area corrections for the DGM and Darcy's Law.	163

LIST OF APPENDICES

	<u>Page</u>
A Laplace Equation	179
B Estimated Liquid-vapor Contact Angle	182
C Two-phase Effective Extraction Area	184
D Uncertainty	188
E List of Equipment	192
F Calibration	196
F.1 Pressure Transducers	196
F.2 Thermocouples	197
F.3 High Speed Camera	198
F.4 Relative Humidity Sensors	201
F.5 Volume Flow Meters	203
G Parts Drawings	206

LIST OF APPENDIX FIGURES

Figure	Page
A.1 Sketch of meniscus geometry consistent with the assumption applied to Eq. (A.2)	180
C.1 Spherical bubbles (grey) arranged in a cubic unit control volume of liquid representing a 9% void fraction, bubbles are equally spaced in a $i \times i \times i$ grid where i is (a) 1 (b) 2 and (c) 3	184
C.2 Cross-section area (πx_b^2) of a spherical bubble with radius r_b	185
C.3 Coordinate system used to integrate the cross-section area of a bubble as it passes through a horizontal plane perpendicular to the page . . .	185
C.4 2D representation of variables used to integrate the cross-section area of a bubble as it passes through a horizontal plane perpendicular to the page, $r_b^2 = x_b^2 + y^2$	186
C.5 Sketches of a 9% void fraction unit cube sliced at half the height, showing (a) a spherical bubble and (b) the equivalent average extraction area	187
F.1 Geometry and variables for Eq. (F.3) to Eq. (F.11)	199
F.2 Pivoting the angled grid lines (membrane ribs) about the horizontal to account for perspective, see Eq. (F.3) to Eq. (F.11)	199
F.3 Measuring the camera angle with reference to horizontal which is parallel to membrane face, this image is for the calibration test	200
F.4 Test image, camera angle 29.1 degrees	200

LIST OF APPENDIX TABLES

<u>Table</u>	<u>Page</u>
F.1 Pressure transducer calibration curves	197
F.2 Thermocouple calibration, $U_{TC}=0.81^{\circ}\text{C}$ which is the maximum uncertainty in heater block (HB) thermocouple “a” HB_a as seen in Fig. 4.20 when calibrated separately in an oil bath. The calibration of this transducer shown here is that from the two-point calibration to be consistent.	197
F.3 Test image calculations, camera angle $\alpha =29.1$ degrees as measured with PicPick’s protractor from Fig. F.3, top three highlighted sections are user input	201
F.4 Relative Humidity Calibration Verification	202
F.5 Calibration coefficients as determined by Pace Scientific	203
F.6 Rotameter calibration curves for polynomial fit	204

NOMENCLATURE

Greek Letters and Symbols

α	Void fraction
β	Volumetric flow ratio
χ	Independent variable
Δ	Change in subsequent variable
δ	Membrane thickness, distance if subscript exists
δ'	Compaction coefficient
ϵ	Porosity
γ	Electrical conductivity
λ	Mean free path
μ	Dynamic viscosity
ω	Humidity ratio
Φ	Relative humidity
Φ_m	Fraction of membrane contacting gas (two-phase area correction)

Φ_s	Fraction of solid under a liquid
ρ	Density
σ	Surface tension
τ	Tortuosity
θ	Contact angle (liquid/vapor interface)
ζ	Dimensional variable with a value of unity

Roman

A	Area
B	Geometric correction factor for pore size, gas transfer coefficient
Bo	Bond Number
C_A	Armand coefficient
d	Diameter
E	Energy
g	Gravity
h	Enthalpy
k	Thermal conductivity
K	Permeability

k_B	Boltzman constant
Kn	Knudsen number
L	Length
M	Molar mass
m	Mass
\dot{m}	Mass flow rate
P	Pressure
px	Pixels
Q	Volume flow rate
q''	Heat flux
R	Resistance, major radius, ideal gas constant
r	Radius
Re	Reynold's Number
T	Temperature
V	Volume
W	Width
x	Quality

Subscripts

○ Initial or non-compacted

a Air

AA Armand, annular flow regime

al Aluminum

atm Atmospheric

c Capillary

const Constant

D Darcy

E Equilibrium

eff Effective

f Fluid, liquid

fg Difference between gas and liquid

g Gas

i Specie

IorII Bulk fluid number

int Intrinsic (associated with smooth surface), interface

l Liquid

lg Liquid-gas

mix Mixture

mol Molecular collision

p Pore

PTFE Active layer of membrane

sat Saturated

sg Solid-gas

sg, d Critical for solid-gas

sl Solid-liquid

sup Support

TC Thermocouple

v Vapor

var Variable

w Water

wall Heater surface in contact with liquid

Superscripts

' Modifying

* Non-dimensional

K Knudsen

P Poiseuille

t Transition

ABBREVIATIONS

CFD	Computational fluid dynamics
CHF	Critical heat flux
DCMD	Direct contact membrane distillation
DGM	Dusty Gas Model
DLVO	Derjaguin-Landau-Verwey-Overbroek, long range hydrodynamic force theory
DMFC	Direct methanol fuel cell
HSHR	High speed, high resolution camera
LEP	Liquid entry pressure, also termed breakthrough pressure (pore wetting pressure)
LRHF	Long range hydrophobic forces (possible cause of film rupture)
MAE	Mean absolute error
MD	Membrane distillation
PP	Polypropylene (material of integrated membrane scrim backing)
PTFE	Polytetrafluoroethylene (DuPont's Teflon [®] brand)
PVDF	Polyvinylidene fluoride
RH	Relative humidity
RMS	Root mean squared
RTV	Room Temperature Vulcanizing silicone
TPC	Three phase contact (solid-liquid-gas)
VMD	Vacuum membrane distillation

Chapter 1 – Introduction

Improvements in cooling technology are continuously being developed to increase the performance and life of temperature-sensitive technology. With a recent increased focus on micro-scale heat transfer devices, issues are arising which did not affect macro-scale device performance. In two-phase heat sinks, one of these problems is coolant instability due to the large volume increase as liquid changes to vapor. Associated with the introduction of vapor is the critical heat flux at which point the heat transfer capabilities diminish and temperatures increase uncontrollably leading to system failure. There are publications which show extraction can delay critical heat flux [1] and prevent instabilities [1,2] by removing the vapor phase from the coolant mixture. Extraction is typically achieved with commercially available hydrophobic membranes [2–4] with either passive venting or vacuum-driven extraction, but the technicalities of mass transfer of the gas phase are generally disregarded in these papers and heat transfer is the main topic of focus. Therefore, this study is intended to promote the understanding of vapor separation from a two-phase mixture by means of vacuum-driven extraction.

1.1 Motivation

As heat emitting devices are miniaturized and advanced, cooling demands tend to increase. These devices typically require a narrow operating temperature to achieve maximum performance, so high performance cooling is necessary. Some examples of high heat flux devices are supercomputers, lasers and fusion reactors among others as Mudawar [5] discusses. Localized, small form factor cooling devices are also desired for applications such as avionics where higher heat flux cooling methods are necessary to reduce volume and weight.

Microchannel heat sinks and jet impingement devices are common geometries for demanding cooling applications. Fluids with low ($<40^{\circ}\text{C}$) boiling points are useful in applications where computer chips need to be cooled because the chips typically operate below 85°C . When heat fluxes are on the order of $1 \times 10^3 \text{ W/cm}^2$ water is the only working fluid that is economical [5]. Due to the interest in water as a working fluid and the potential need for vapor separation to reduce the onset of critical heat flux, this study focuses on vapor separation from two-phase water.

1.2 Background

As pointed out by Salakij et al. [6], multiple researchers have looked into less complicated methods of reducing vapor instabilities than vapor extraction. Examples of the other methods used are expanding channels, inlet restrictions and artificial nucleation sites. While some of these methods alleviate the target issues, they also have setbacks such as high pressure requirements, reliability issues or temperature

variations in the object being cooled. Therefore vapor separation has been an area of focus in micro-scale heat sinks.

Vapor separation is being studied because it provides benefits in heat transfer applications [6] and is not well understood because researchers are typically more concerned with heat transfer at the wall to be cooled than mass transport through the membrane. The study most similar to the result of this thesis is that of Alexander and Wang [7] who developed a non-dimensional model to predict air extraction rates from water-air mixtures using low pressure differences. Their study used a custom manufactured silicon membrane with large pore sizes ($10 \mu m$) and therefore a low liquid entry pressure (LEP) of 9 kPa. Their model is specific to microchannel flows and vapor was not studied. Fang et al. [1] who developed a CFD model which was found to predict experimental data well by David et al. [2]. These studies did not produce a model to predict the flow rate through a membrane.

To better understand the phenomena affecting gas extraction from two-phase mixtures, the nature of the membranes used must first be considered. Membranes are a form of a porous media, but they are different than packed beds of spheres or sand because of the low thickness to flow area ratio. In engineering applications, membranes are typically used to filter fluids to reduce contaminants and volatiles for health reasons or for achieving more pure working fluids. Some of these membranes allow liquids to wet the pores and therefore flow through, whereas other membranes restrain liquid at the pore entrance as a result of surface tension forces. The membranes that restrain liquids are termed hydrophobic, their defining characteristic is quantified by the contact angle of a droplet being greater than 90° . Whether a membrane is hydrophobic

or not depends on the material with which it is made. Polymers are common materials used to manufacture hydrophobic membranes but there are coating methods to hydrophobize other materials. Hydrophobic membranes made from polymers are typically less expensive than other types of membranes with similar characteristics, especially when the cost of power to force fluid through the membrane is considered. Hydrophobic membranes are therefore used for their filtering capabilities or energy benefits in many applications, and the fact that they are hydrophobic makes no difference. For example, Gibson et al. [8] show that polytetrafluoroethylene (PTFE, the material used in DuPont's Teflon[®]) membranes are extremely effective at protecting humans from biological weapons and the flexibility of this type of membrane makes for a more protective garment.

Chapter 2 – Literature Review

Presented in this chapter is the current state of research applicable to gas transport through porous media and gas extraction from liquid-gas mixtures. Broad topics and applications are first considered, then topics relevant to the phenomena affecting gas extraction are presented. Phenomena that are outside the scope of this study are also introduced to give the reader some insight into the details impacting the overall effects to which they contribute.

2.1 Application of Hydrophobic Membranes

There are various applications where the hydrophobic nature of the membranes is useful such as where a gas is desired to permeate through the membrane but liquid needs to be restrained. A common example of this is in waterproof, breathable clothing. In fact, the well known clothing manufacturer Gore-Tex[®] was one of the first companies to produce economical hydrophobic membranes in the early 1980s [9]. In this application, body heat, wind and diffusion allow vapor and air to pass through the membrane, but droplets of liquid water remain on one side.

In addition to heat sinks, other applications that are relevant to this study include membrane distillation and fuel cell venting. These studies typically use the same types of membranes that were initially marketed for micro-filtration purposes [9].

Membrane distillation (MD) is a process in which evaporation occurs from a liquid feed. MD is different from the heat transfer and separation fuel cell studies because it does not have gas bubbles mixed with the liquid; therefore, MD consists of single-phase transport.

2.1.1 Single-phase Transport

Hydrophobic membranes are known to have been used since at least 1963 to remove contaminants from fluids [10]. However, not many studies were published on this subject until the 1980s. Prior to this time, membranes were not as thin as they are today and high pressure differences were required to produce the same end product as less expensive alternatives. Applications of membranes such as reverse osmosis and nanofiltration will not be discussed here, but they are single phase pressure-driven processes.

2.1.1.1 Membrane Distillation

The goal of membrane distillation (MD) is to remove volatiles from solutions. This can be done in a number of different ways depending on the components to be removed from the aqueous mixture. The difference between the types of MD is the process which drives the evaporation process. The most similar MD process to the separation process for heat transfer applications is vacuum membrane distillation (VMD). VMD is the least studied MD process with only about 15% of all published

MD studies focusing on it [11]. This method is not studied frequently because it requires a condenser to convert the purified vapor into a liquid, whereas direct contact membrane distillation (DCMD) inherently condenses the vapor.

Researchers who conduct MD studies provide a detailed analysis of the membranes being used and sometimes even manufacture their own [9, 12–18]. The membranes are characterized by a number of different variables depending on the nature of the study and the model being used. In a majority of the MD studies, especially those published after the late 1990s, a detailed model is used which does not require any empirical constants, the dusty gas model. Many other studies rely on Darcy’s Law [19] which was developed in the mid-1800s and is still useful, but not purely theoretical like the dusty gas model. Some of the variables that are used to describe each membrane are the thickness, tortuosity, porosity, permeability and surface roughness and fluid contact angle.

The VMD studies are concerned with the effectiveness of removing volatile organic components (VOC) from mixtures or separating traces of a solute from water, including condensed gases. In MD studies, pure water is typically considered as a basis for comparison, which makes the studies useful when describe some of the phenomena relating to extraction. VMD requires high pressure differences to promote evaporation from the liquid on the one side of the membrane; therefore, liquid entry pressure (LEP) and compaction are sometimes a key focus. These phenomena will be discussed further in section 2.3.1.

2.1.2 Two-phase Separation

When a mixture of liquid and gas is on one side of the membrane, the gas can be selectively removed if the pressure in the mixture is higher than the pressure on the other side of the membrane or if a pressure difference is applied with a vacuum. If a vacuum is not used, the venting is termed “passive” and otherwise the venting is “active.” This study, like VMD, relies on active venting to separate the phases.

2.1.2.1 Microchannel Heat Sinks

Recent studies have focused on the application of hydrophobic membranes in thermal management, which benefit from two-phase separation processes. Apreotesi [4] studied a micro-scale branching fractal-like network with vapor extraction and others have studied more conventional geometries such as rectangular cross-section micro-channels [1, 2, 20] and impinging jets [21]. The majority of these studies were experimental and focused on aspects of the system other than the membrane, such as flow regime in the channel (in addition to heat transfer) [1, 2, 20]. In these studies, the membrane is typically supported with a perforated plate contacting the low pressure side of the membrane, because without it the membrane would deform significantly.

There were also two-phase liquid-air studies performed [7, 20, 22] to better visualize the extraction behavior in flows where bubbles are confined and move parallel to the membrane. This type of flow is typically seen in micro-scale heat transfer applications because a small channel cross section results in a higher heat transfer coefficient than larger channels. Alexander et al. [7] attributed the mechanisms for film rupture in a

small channel to bubble size and bubble velocity for air flowing with a liquid. Xu et al. [20] found that bubbles smaller than the channel diameter could not be extracted. They found that as the superficial liquid flow rate was increased, the bubble changed from a circular shape to a nearly triangular shape as viewed perpendicular to the flow. This is due to the surface tension forces at the channel walls and was related to the Weber number (relating surface tension to inertia).

2.1.2.2 Micro-scale Fuel Cells

Meng et al. [23] studied the feasibility of separating carbon dioxide (CO_2) gas from a stream of liquid methanol in a micro-direct methanol fuel cell ($\mu DMFC$), where passive venting of CO_2 is achieved with a microporous membrane above a set of vapor traps to encourage the bubbles to remain separate instead of agglomerating. One benefit of this type of system is that a liquid-gas interface can be sustained if the extraction rates are low enough. This would eliminate the need to rupture a thin film at the membrane interface. Meng et al. [23] developed a differential equation to describe the shrinkage rate of a gas slug in a confining tube.

2.2 Physics of the Liquid-gas Interface

It is important to understand the liquid-gas interface as viewed from a molecular level because the models that are to be used in the present study depend on molecular interaction. When gas bubbles are submerged in a liquid, the greatest number of

atoms have balanced charges when the surface area is reduced, and therefore they tend to form spherical shapes. The atoms at the interface are not balanced because the molecular spacing varies in the radial direction of the bubble. A more detailed analysis of the interface is given in Carey [24] and de Gennes [25]. A general understanding of these interface properties are useful in understanding the physics at the pore interface, is discussed next.

2.2.1 Laplace Equation

The Laplace equation Eq. (A.1) relates the pressure difference across a liquid-gas interface to the interfacial tension between the phases. Therefore, the liquid entry pressure (LEP) is defined by the Laplace equation. The LEP is also referred to as the breakthrough or pore-wetting pressure. When implementing this equation to predict LEP, it is assumed there is a significant amount of liquid on the low pressure side of the membrane. This assumption is valid when liquid is the only phase on the low pressure side of the membrane, but when bubbles exist in the liquid the LEP in the thin films between the bubble and membrane is likely not the same as is predicted by the traditional form of the LEP equation as described in this section. The purpose of describing the Laplace equation is to provide an understanding of how the liquid can be selectively retained, and also provides insight on the effect of a thin liquid on the low pressure side of the membrane.

The Laplace equation can be used to estimate the pressure at which the liquid-gas interface (the meniscus) will no longer be supported by the capillary forces of the pores

of the membrane. Assuming the pore is cylindrical, the meniscus can be approximated as a semi-spherical interface when the pore radius is an order of magnitude less than the capillary length, L_c , as defined by

$$L_c = \left[\frac{\sigma}{(\rho_l - \rho_g) g} \right]^{1/2} \quad (2.1)$$

To assess the validity of the spherical interface, the manufacturer's specified pore size is compared to the capillary length of saturated liquid water in contact with its vapor. If the pore radius is much less than the capillary length, then the assumption is valid. Letting the surface tension equal 0.05891 N/m as indicated in Vargaftik et al. report [26], the capillary length is calculated to be 2035 μm which is typically much greater than the pore radius. As can be seen in Fig. 2.1, this approximation is visually reasonable.

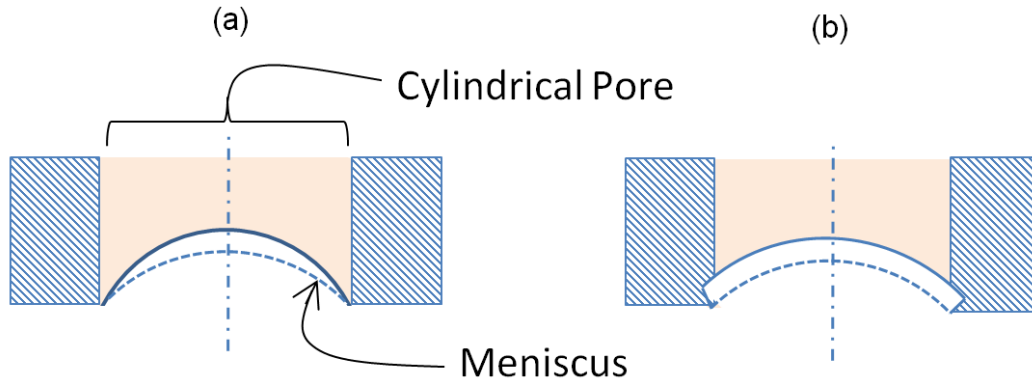


Figure 2.1: Sketch of the meniscus geometry assumptions applied to Eq. (2.2) showing the original (dashed line) and deformed (solid line) meniscus shape with applied pressure difference across the liquid-gas interface representing (a) the actual meniscus deformation and (b) the assumed spherical meniscus deformation. Gas is in the pore and is shown shaded and the pore wall is shown hatched.

As described in appendix A, the Laplace equation simplifies to

$$\Delta P_{max} = \frac{-2\sigma \cos(\theta)}{r_p} \quad (2.2)$$

which is implemented to determine the liquid entry pressure of the pores in the membrane.

2.2.2 Contact Angle

The contact angle, θ , shown in Figs. 2.2 and A.1 is a measure of hydrophobicity. The contact angle can be measured with one combination of liquid, gas and solid to predict the contact angle of another combination of fluids and the same solid. This is useful if the contact angle of water is desired when in equilibrium with its vapor because it is much easier to measure the contact angle of water in equilibrium with air at temperatures lower than saturation. The contact angle depends on Young's Law

$$\cos\theta = \frac{\sigma_{sg} - \sigma_{sl}}{\sigma_{lg}} \quad (2.3)$$

which is a balance of surface tension forces between the solid and gas, σ_{sg} , the solid and liquid, σ_{sl} , and the liquid and gas, σ_{lg} .

The contact angle can be measured with the Sessile drop method as shown in Fig. 2.2. This method requires a drop of liquid to be placed on the surface of interest surrounded by the gas of interest, then a camera is focused such that it is in

plane with the surface and the radius of curvature can be seen. The vertex of the contact angle is at the liquid-gas-solid point of intersection and a line is pivoted until it is tangent to the edge of the drop; the other line is the face of the solid. The contact angle is measured through the liquid phase, so a liquid water drop on a leaf will result in a high contact angle. If the contact angle is greater than 90° then it is considered hydrophobic. If the contact angle is greater than 140° it is typically considered superhydrophobic.

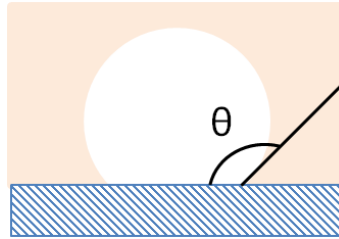


Figure 2.2: Sketch of the contact angle of a liquid drop on a solid surface surrounded by gas, as measured with the Sessile drop method.

The polymer PTFE (Teflon[®]) in contact with water is intrinsically a hydrophobic surface with a published value of $\theta_{int} = 108^\circ$ at 20°C [24]. Any surface roughness will increase the contact angle for the same fluid and temperature, as described by Wenzel's Law and the Cassie-Baxter model [24, 25]. The Wenzel Law only applies when the solid is fully wetted. When a surface is wetted, the liquid phase is in contact with the solid underneath a drop. If the surface is not fully wetted, gas is trapped in the cavities of the solid under the liquid.

Whether or not a solid wets depends on the critical surface tension, $\sigma_{sg,d}$, of the solid and the surface tension of the liquid-gas combination, σ_{lg} - assuming the liquid

is immersed in a gas (such as the air of the atmosphere). The critical surface tension is evaluated by determining when the spreading coefficient of the solid-liquid-gas combination becomes positive, which indicates a wetting condition. The spreading coefficient depends on the surface tension of the system and the fully wetting contact angle, which is 180° . Consequently, the relationship of the intrinsic contact angle, θ_{int} , to the properties of the solid and liquid is [24]

$$\cos\theta_{int} = 2 \left(\frac{\sigma_{sg,d}}{\sigma_{lg}} \right)^{1/2} - 1 \quad (2.4)$$

Eq. (2.4) is applicable when $\sigma_{lg} > \sigma_{sg,d}$. This equation is derived with the assumption that dispersion forces between the solid and liquid dominate in the process defining equilibrium; therefore, it is meant to be used with non-polar liquids where electrostatic forces are less significant. Electrostatic forces are either attractive or repulsive depending on molecular orientation. Water is polar, but the water employed in two-phase heat exchangers is at saturation, so dispersion forces dominate because phase change is controlled by attractive dispersion forces not repulsive electrostatic forces [24]. This can be visualized by realizing that as liquid approaches its saturation temperature, the density decreases; less dense molecules have greater molecular spacing which causes the electrostatic interaction potential to diminish in proportion to the dispersion potential. Therefore, it is assumed to be reasonable to estimate the contact angle of water at saturation with Eq. (2.4). This will be discussed further in section 5.4.

The Cassie-Baxter model [24, 25] estimates the apparent contact angle of a rough

surface when the surface tension of the liquid is greater than the critical surface tension of the solid. When this occurs, the Wenzel model [24, 25] no longer holds because the surface roughness results in partial wetting of the solid where the voids in the roughness are occupied by a separate specie such as gas. The pores trap gas because it is energetically more favorable based on the surface tension force balance. As discussed in other work [25], the Cassie-Baxter model accounts for the influence of the 180° liquid-gas contact angle and simplifies to

$$\cos\theta = 1 - \Phi_s(1 + \cos\theta_{int}) \quad (2.5)$$

where Φ_s is the fraction of solid in contact with the liquid. Eq. (2.5) is used because it applies to the extraction process.

2.3 Gas Transport Physics

The present state of research provides well validated models describing single fluid phases through porous media. These models have been shown to account for some phenomena which limit gas transport such as membrane compaction. There are additional phenomena associated with gas transport when the gas is supplied from two-phase flow.

2.3.1 Phenomena Limiting Gas Transport

There are a few different phenomena that can limit gas transport, some of which have already been studied in the literature. The topics which have been studied to date are fouling, liquid entry pressure (LEP), membrane temperature dependence and pore size distribution. Fouling is caused by prolonged membrane use allowing particles or corrosion to build up on the surface of the membrane. It is generally accepted that fouling with distilled water as a working fluid is not an issue, as pointed out by El Bourawi et al. [11] stating that after two months of transport there was no decrease in mass transfer across a membrane. Even though fouling is likely not an issue, the fluids used in this study were filtered sufficiently to reduce its chance of occurring.

Liquid entry pressure (LEP) has been studied by many authors as a verification of the theoretical pressure needed for the liquid meniscus to no longer be supported by the pore, this is predicted by the Laplace equation Eq. (2.2). In addition to quantifying the LEP, fluid transport following LEP has been studied as a function of pressure cycling by Peña et al. [12] and Sarti et al. [27]. In their pressure cycling study, Peña et al. [12] found that when one side of a $0.45 \mu\text{m}$ pore diameter PTFE membrane was exposed to liquid water and a 90 kPa pressure difference was applied across the membrane, LEP occurred. Subsequently, if the pressure difference was increased to about 200 kPa, there was a substantial increase of liquid transport through the membrane. Once this maximum pressure differential was reached, half of a cycle was achieved and the pressure was decreased for the second half of the cycle. In the subsequent cycle, the same maximum pressure was reached and the measured fluid

transport followed the previous curve to a pressure difference of approximately 60 kPa then continued to increase. This trend shows that if breakthrough were to occur, a significant increase in mass transport should be measured.

Membrane temperature dependence is important here because the typical application of PTFE membranes is at room temperature or slightly higher. The temperature dependence has been studied by a few authors [18, 28] including Saffarini et al. [29]. Saffarini et al. [29] were specifically looking at the microstructure evolution of the PTFE as temperature increased from 25°C to 75°C and discovered that the major changes due to temperature occurred closer to room temperature. Their study showed that for interwoven PTFE nanofibrous pores with an average pore diameter of about $0.2 \mu m$, the breakthrough pressure was lower than that predicted by the Laplace equation. The Laplace equation assumes a circular pore opening, so it is expected that the actual breakthrough will be different than the theoretical one. To make the theoretical prediction more accurate, Saffarini et al. [29] calculate a geometric pore factor which approaches 0.6 at elevated temperatures. This factor was determined using 70°C deionized water so is not completely accurate for saturated water at atmospheric pressure (100°C), but at least improves the LEP estimation.

Pore size distribution was studied by a few researchers including Saffarini et al. [29], but Martinez et al. [16] studied the same membrane which is used in extraction studies [2, 22]. Martinez et al. [16] found that the pores in the membrane vary in a narrow Gaussian-type distribution ranging from $0.36 \mu m$ to $0.60 \mu m$ in diameter with a mean pore diameter of $0.47 \mu m$.

One of the first compaction studies was performed by Persson et al. [13] using

Darcy's Law to capture the effects of compaction. When Darcy's Law is used, all of the possible effects limiting mass transport are lumped into one variable. In the case of the Persson et al. [13] study, this variable was the membrane resistance which is the inverse of the permeability multiplied by the membrane's thickness. The resistance was found to be linearly related to the pressure difference across the membrane by a power of 0.8. In later studies by Lawson et al. [30], the dusty gas model was modified to let the membrane thickness be a linear function of pressure. This model was also used by Zhang et al. [31] and provides a good explanation for the membrane behavior.

Condensation within the membrane has been mentioned by researchers studying the use of membranes in heat transfer applications [1,32] and by researchers studying MD [9,10]. This phenomenon would be caused by a change in saturation temperature or pressure therefore causing vapor within the pores to condense and clog parts of the membrane. The MD papers such as the review by Lawson and Lloyd [10] typically note that when calculating empirical permeation variables, non-condensable gases such as nitrogen must be used to avoid problems with water vapor. In MD applications, the liquid feed is heated but kept below the saturation temperature. If there are reductions in mass flux in MD systems, they are said to be a result of phenomena other than condensation.

A phenomenon similar to condensation which could be limiting mass flux is droplet entrapment. Droplet entrapment is likely in two-phase systems with gas extraction because before a gas bubble can be transported through the membrane, the thin liquid film between it and the membrane must be removed. The liquid will drain as a result of the bubble's buoyant force if the membrane is above the fluid as is typically the case.

Furthermore, since the membrane is hydrophobic it has an affinity for the gas and therefore a more stable system will result if the gas is in contact with the membrane. This process will occur without the aid of an extraction pressure as is described in section 2.3.3. The bubble comes into contact with the membrane due to instabilities, and if those instabilities are artificially induced by the pressure difference across the membrane, it is likely that some of the film will get sucked into the membrane. The author here is not aware of any published accounts of this phenomenon.

2.3.2 Porous Media Flow Models

Theoretical models predicting gas flow through porous media as a function of the applied pressure difference rely on fluid properties and membrane characteristics. Two models are presented in the following sections, both include the thickness of the membrane. Only the dusty gas model includes the porosity and tortuosity, and is entirely theoretical. Tortuosity is a description of the path a molecule must take to pass through the membrane. Tortuosity can be calculated by taking the ratio of electrical conductivities with and without the porous media as described by

$$\tau = \frac{\gamma_o}{\gamma_w \epsilon} \quad (2.6)$$

where γ_o is the conductivity of a pure ionic solution saturating the non-conductive porous media, γ_w is the conductivity of the same fluid measured across the same thickness as the porous media and ϵ is the porosity of the porous media. This experimental method is described in detail by Liu and Masliyah [33] who also describe how tortu-

osity can be measured with sound waves. Liu and Masliyah [33] also provide many equations relating porosity to tortuosity for a given type of porous skeleton. However, assumptions are typically made to estimate the tortuosity of thin porous media such as membranes. In this section, models which are able to predict flow through randomly oriented nanofibers such as those produced through electro-spinning [8] and stretching are discussed.

2.3.2.1 Darcy's Law

One of the first models used to predict flow characteristics through porous media was Darcy's Law. Darcy's law is commonly used because it is a simple equation and can describe flows through many types of porous media. It has a single empirical variable, the permeability, K_D , which accounts for any phenomenon inhibiting flow through the porous media. Therefore, Darcy's Law is only useful if the permeability has been empirically determined using a similar flow regime as the fluid of interest. Since the permeability is a constant value, Darcy's Law requires a linear relationship between volume flow rate and the pressure difference to predict the flow rate,

$$Q_D = \frac{K_D A \Delta P}{\mu \delta} \quad (2.7)$$

The Darcy resistance is the inverse of the Darcy permeability then multiplied by the membrane thickness, δ . Therefore, Darcy's Law can be modified to

$$Q_D = \frac{A\Delta P}{R_D\mu} \quad (2.8)$$

where the resistance, R_D , is specific to a membrane or packed bed with a certain thickness. The advantage of using the resistance over the permeability is that there is typically a high uncertainty associated with the measurement of the membrane thickness if it is thin, because the total thickness can be on the order of 15 μm . When this uncertainty is included in the permeability, flow rate predictions are less accurate than when using the same membrane and the resistance. The volume flow rate, Q , can be converted to the mass flow rate, \dot{m} , by multiplying by the fluid's density, ρ

$$\dot{m}_D = \frac{K_D}{\delta} \frac{A\Delta P\rho}{\mu} = \frac{1}{R_D} \frac{A\Delta P\rho}{\mu} \quad (2.9)$$

It is common to assume a constant value for permeability or resistance, however if the relationship between flow rate and pressure difference is non-linear, this has limited applicability.

2.3.2.2 Dusty Gas Model

The dusty gas model is an electric circuit analogy accounting for flow resistances due to Knudsen (molecule-wall), Poiseuille (viscous, molecule-molecule) and diffusion (species interaction). Since vapor is a single specie and air can be approximated as a single specie, the diffusion resistance can be assumed to have negligible influence on

the total gas transport. This same assumption is relevant to VMD applications [9]. This leaves two flow regimes which can contribute to resisting the gas flow through the membrane. Depending on the pore size for gas flows, the Knudsen effect can potentially be considered negligible. This is determined by analyzing the Knudsen number,

$$Kn = \frac{\lambda_i}{\bar{d}_p} \quad (2.10)$$

which relates the mean free path of a specie

$$\lambda_i = \frac{k_B T}{\sqrt{2\pi P} d_{col}^2} \quad (2.11)$$

to the wall-to-wall spacing of the solid it is passing. In the case of membranes, this spacing is taken as the mean pore diameter, \bar{d}_p . The mean free path depends on the Boltzmann constant k_B ($1.38 \times 10^{-23} J/K$) and the collision diameter d_{col} of the species considered. The collision diameter of water vapor [9] and air [34] are 2.64×10^{-10} m and 3.66×10^{-10} m respectively.

The Knudsen number can be used as an indication of the flow regime. As is discussed in section 5.5, there is a range in which both flows need to be considered, because the flow regime is in “transition.”

For transition between Knudsen and Poiseuille flows, the total resistance to gas flow is described by the contribution of each regime’s resistance in parallel. This results in an equation with the general relationship analogous to the electrical relationship, $V = IR$:

$$\Delta P \propto QR_{tot} \quad (2.12)$$

where R_{tot} is the total resistance to the volume flow rate, Q , and the driving potential is the pressure difference, ΔP . Considering the two resistances to flow are in parallel as described by Khayet [9], Eq. (2.12) expands to

$$\Delta P \propto Q \left(\frac{1}{R^K} + \frac{1}{R^P} \right)^{-1} \quad (2.13)$$

where the Knudsen and Poiseuille resistances are R^K and R^P , respectively. When Eq. (2.13) is rearranged to isolate the volume flow rate, the inverse resistances are summed which can be converted to the sum of conductances, B :

$$Q \propto \Delta P \left(\frac{1}{R^K} + \frac{1}{R^P} \right) \propto \Delta P (B^K + B^P) \quad (2.14)$$

Therefore, the total conductance is the transition conductance, B^t , for the gas specie of interest, i ,

$$B_i^t = B_i^K + B_i^P \quad (2.15)$$

because the Knudsen and Poiseuille resistances are in parallel. While Khayet et al. [17] define this conduction, B_i , as a ‘‘VMD coefficient’’ which they also refer to as an ‘‘experimental water vapor transfer coefficient,’’ these descriptions are for their specific MD application. Therefore, B_i will be simply referred to here as the ‘‘gas transfer coefficient.’’ The mathematical equation is the same as that in the

literature, but the description is different. The Knudsen contribution to the gas transfer coefficient is

$$B_i^K = \frac{1}{RT\delta} \frac{2\epsilon\bar{r}_p}{3\tau} \left(\frac{8RT}{\pi M_i} \right)^{1/2} \quad (2.16)$$

and the Poiseuille contribution is

$$B_i^P = \frac{1}{RT\delta} \frac{\epsilon\bar{r}_p^2}{8\tau\mu_{v,i}} \bar{P} \quad (2.17)$$

where i is the gas species, M is the molecular weight and the exponents of the gas transfer coefficient (B) designate the flow regime (“t” is “transition”).

To estimate the resulting flow rate due to an applied pressure difference across the membrane ΔP , Eqs. (2.16) and (2.17) are substituted into Eq. (2.15) to give the gas transfer coefficient B_i^t . The gas transfer coefficient is then multiplied by the pressure difference to predict the molar flux ($mol/(m^2s)$) through the membrane when the gas is in the Knudsen-Poiseuille transitional flow regime. This can be converted to mass flow rate

$$\dot{m}_i = \Delta P B_i^t M_i A \quad (2.18)$$

Substituting Eq. (2.15) into Eq. (2.18) results in

$$\dot{m}_i = \frac{\Delta P M_i A \epsilon}{RT\tau\delta} \left[\frac{2\bar{r}_p}{3} \left(\frac{8RT}{\pi M_i} \right)^{1/2} + \frac{\bar{r}_p^2}{8\mu_{v,i}} \bar{P} \right] \quad (2.19)$$

The membrane porosity ϵ is multiplied by the flow area A which corrects the total flow area to the area of the membrane face available for flow. This model is often

introduced in regard to a single pore where the flow area is the area of a circle with radius equal to the pore radius. This single-pore equation can be summed over a range of pore sizes, however the pore distribution must be known. Khayet et al. [9] report that multiple authors found insignificant differences between flux predictions for mean \bar{r}_p and distributed r_p pore sizes.

2.3.3 Three Phase Contact Models

The phenomenon of a solid, liquid and gas phase contacting each other is known as three phase contact (TPC). Related to this is the study of thin films rupture which is the mechanism which allows TPC to take place. When a bubble approaches a surface, the liquid separating the gas and solid phase is forced out of the way due to buoyant and other forces. When the liquid drains to the point where the liquid separating the gas and solid is much smaller than the radius of the gas phase, the liquid layer is considered a “thin film” [35]. At this point, the film is typically on the order of ten nanometers, at which point it begins to become instable. Radoev et al. [35] explain how the Reynold’s equation (based on the Navier-Stokes equations) can be used to predict thin film draining and it is shown to include an electrostatic and van-der-Waals term by Schulze et al. [36]. The van-der-Waals component is only effective for a thickness of about 1 nm [36], so it adds little contribution to the thinning.

The phenomena behind thin film rupturing is ultimately caused by wave instabilities in the thin film, which can be induced by thermal fluctuations or long range hydrophobic forces (LRHF). A common theory which is relied on for film rupture is

the Derjaguin-Landau-Verwey-Overbeek (DLVO) theory but it only considers capillary pressure as a driving force for thinning. Shulze et al. [36] found that forces other than LRHF, termed “non-DLVO forces,” are present when the solid is hydrophobic. It is believed that the dominating rupture process is due to nano-scale gas bubbles near the hydrophobic surface. These “Harvey nuclei” are believed to be flat bubbles and therefore can remain stable despite their high pressure [36].

Liquid-air interaction has been studied by Krasowska et al. [37] with hydrophobic surfaces of varying roughness. They found that the approach velocity of a bubble has a strong influence on the TPC behavior. If the velocity is higher, the kinetic energy of the bubble is great enough such that a collision with the membrane does not dissipate enough energy to allow for stable contact formation. Even if contact with the solid is initiated, the bubble could still disassociate, possibly leaving behind a small bubble at the solid surface. Krasowska et al. [37] studied bubbles of 1.5 mm diameter traveling through water and approaching rough Teflon[®] plates. There are no known studies of film rupturing on porous media where a pressure difference is applied to the liquid-membrane interface.

2.4 Major Conclusions of Two-phase Vapor Extraction Studies

Most of the two-phase separation studies are limited to one-dimensional flows where the bubble is confined to movement along the length of a channel until the film it is sliding on ruptures. Xu et al. [20] developed a relationship to calculate the critical velocity for film rupture and found that for this to occur, bubbles must be the

same diameter as the channel. Alexander and Wang [7] developed a non-dimensional model to predict the maximum volume flow rate of air which could be extracted from a microchannel with $10 \mu m$ pores, low extraction pressures and a rigid membrane. Meng et al. [23] studied gas separation from liquid in a clear tube and developed a specific equation to estimate bubble shrinkage characteristics due to extraction.

There are some specific studies which were offshoots of heat transfer studies to better understand commercially available membrane limitations. Fang et al. [1] numerically simulated condensation by adding a heat sink to the membrane surface and found that vapor did get trapped in the membrane. The membrane's behavior when the heat sink is removed is not mentioned. David et al. [32] looked into condensation with boiling water in microchannels, they found that additional heat was removed from the system when air was employed to clear condensed liquid off the low pressure side of the membrane. In regards to the phenomena improving the cooling when air was clearing the liquid, their facility did not allow them to identify the individual contribution of (i) liquid removal on the low pressure side of the membrane and (ii) possible evaporation of liquid trapped within the membrane pores.

Chapter 3 – Problem Statement and Approach

This study was designed to better understand the behavior of vacuum-driven flow of saturated vapor through a hydrophobic membrane when bubbles are smaller in diameter than the membrane surface. Existing models to estimate flow rates are assessed, limitations with extraction are determined and operating procedures for predictable behavior are defined.

Extraction phenomena need to be studied because film rupture studies are limited to solid surfaces, some of which are rough and few of which are both rough and hydrophobic. Eventually, theoretical models for film rupture need to be coupled with existing transport models; these transport models are well developed for fluids which remain in the same phase as they pass through the membrane. An experimental study will help verify the major contributing phenomenon impacting gas flow through membranes in extraction applications.

There are multiple factors which have a significant contribution to the gas flow rate through membranes, therefore it would be best to use multiple fluids and phases to draw relevant conclusions. Studying single-phase gas transport allows for isolation of the phenomena which directly affect the membrane. These phenomena also exist in two-phase flows, so the knowledge from the single-phase studies can be used to isolate the phenomena which are introduced in gas extraction from two-phase mixtures. The expected phenomena contributing significantly to a reduction in mass flow rate are

presented in the the following sections.

3.1 Study of Single-phase Gas Flow

Phenomena restricted to single-phase gas transport are considered first because there are existing models to describe this type of flow. The models predicting single-phase gas transport through porous media account for the flow regime, but other phenomena influencing the transport are membrane-dependent such as fouling, compaction and the membrane support structure. Fouling is eliminated by filtering the fluids. Membrane compaction occurs as a result of the applied pressure difference driving gas transport. This pressure difference is applied across the thin sheet-like membrane area resulting in a compressive force and therefore a reduced membrane thickness. The membranes are flexible enough to require a support structure on the low pressure side of the membrane so the membrane does not deform as a diaphragm does. Supports are often perforated plates with holes larger than the pores of the membrane, and therefore compaction will result in non-uniform changes in membrane thickness. If the membrane consists of an active microporous layer adhered to a scrim backing for improved durability, the holes of the perforated support should be kept smaller than the holes of the scrim. This will ensure the microporous layer of the membrane will remain as planar as possible. The scrim backing and membrane support are described in more detail in sections 4.1 and 4.5. As pointed out by Lawson et al. [30], membrane compaction depends on the structure of the membrane which is temperature dependent. Therefore, both vapor and air will need to be tested for

empirical compaction fits because they are studied at different temperatures.

Compaction affects the properties of the membrane including thickness, porosity and tortuosity. These three properties mathematically describe the membrane. These properties are schematically introduced in this section and calculations are described in detail in section 5.5.2. As seen in Fig. 3.1, compaction will reduce the membrane thickness which in turn reduces the porosity. The solid material making up the pore structure retains its volume, but the void making up the pores decreases.

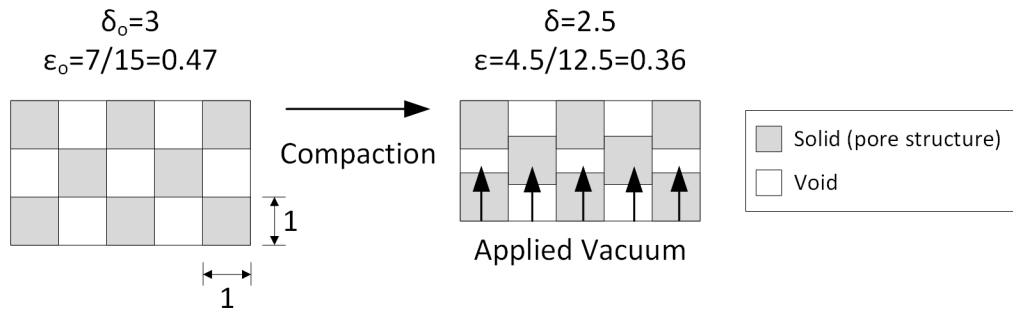


Figure 3.1: Representation of reduced porosity as a result of compaction

As depicted in Fig. 3.1, some membranes do not have straight-through pores, but rather have interconnected pores. Therefore, the gas flowing from one side of the membrane to the other must take a tortuous path. As the membrane is compacted, the pore placement does not change, but the length of the pores (the thickness of the membrane) does, so the tortuosity reduces as shown in Fig. 3.2. Note that the tortuosity is likely a function of porosity, and if it is assumed to be the inverse of the porosity (section 5.5.2), then tortuosity decreases with increased porosity unlike Fig. 3.2 shows. Aside from Fig. 3.2, a brief description of tortuosity is in section 2.3.2, but the reader is referred to Liu and Masliyah [33] for more detail.

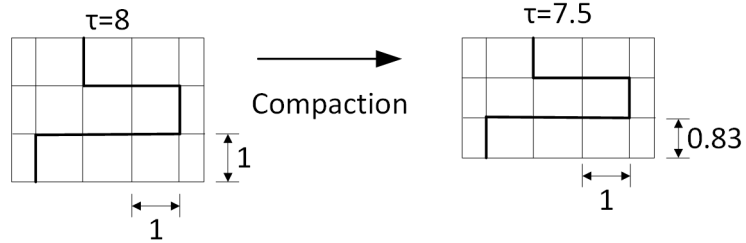


Figure 3.2: Representation of reduced tortuosity as a result of compaction

When gas is the only phase in the system, phenomena restricting its flow rate can be described by Darcy's Law or the dusty gas model when compaction is accounted for. When a liquid and gas phase are in contact with the membrane on the high pressure side, other phenomena restrict the flow rate.

3.2 Study of Two-phase Gas Extraction

The phenomena restricting gas transport when liquid and gas are contacting the membrane consist of phenomena within the membrane and phenomena in the two-phase mixture external to the membrane. Hydrodynamics and a resulting reduced extraction area occur external to the membrane (exo-membrane). Pore wetting, droplet entrapment and condensation are phenomena occurring within the membrane (intra-membrane). The droplet entrapment is on the scale of the pore sizes as depicted in Fig. 3.3, where the droplets decrease the effective porosity and increase the tortuosity of the membrane.

Once compaction is quantified from the single-phase tests, it is accounted for in liquid-air extraction where condensation is unlikely but droplet entrapment is possi-

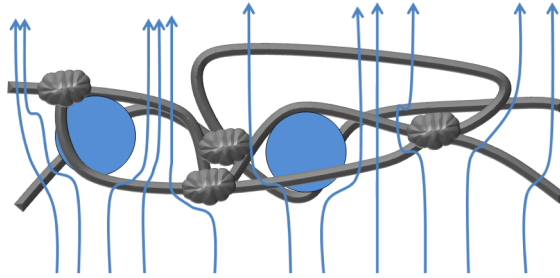


Figure 3.3: Representation of reduced porosity as a result of droplet entrapment, arrows represent gas streamlines, circles represent trapped liquid drops and the mesh represents the pore structure.

ble. However, if existent, the effects of droplet entrapment are assumed to be temporary because the liquid drops may diffuse into the dry air flowing through the pores. After applying the compaction predictions, the effective extraction area is evaluated. Related to the effective extraction area is three phase contact (TPC) formation, bubble velocity and film rupture. The two-phase tests include high speed videos of the membrane-bubble interface to analyze TPC and are used to draw conclusions about any unexpected results that arise in the post-processing. The combination of evaporation at the liquid-membrane interface, droplet suction and vapor diffusion into bubbles as they pass through the liquid are quantified to evaluate the contribution of diffusion in the gas transport process.

Pore wetting, which occurs when liquid entry pressure (LEP) is achieved, is influenced by the pore size distribution, contact angle and geometric pore factor. Many of these factors are already accounted for by other authors [16, 29] and a membrane is selected which has a LEP higher than the pressures which is applied in the tests. Therefore, the only intra-membrane phenomena limiting the flow rate are condensa-

tion and droplet entrapment, however droplet entrapment may be a result of partial pore wetting and LEP of thin films.

Condensation and droplet entrapment are studied with liquid-vapor experiments. This is accomplished by cycling the pressure difference and therefore changing the saturation temperature of the vapor traveling through the membrane. When cycling the pressure, the thermal time response of the solid material making up the pore structure of the membrane may be slow enough to induce condensation.

Finally, the two-phase data is empirically fit to correct single-phase porous media transport models to provide accurate extraction predictions. Developing these corrections will help determine the dominating forces influencing extraction.

Chapter 4 – Experimental Apparatuses and Procedures

Four experimental apparatuses were employed to isolate the phenomena affecting gas transport in extraction systems. The single-phase devices were most simple and test times could be shorter than the two-phase tests due to higher flow rates. The two-phase devices are more complicated because of increased variables and variations of flow rate due to bubble dynamics. For all apparatuses, the same extraction chamber is used and therefore the membrane flow area remains the same. All experiments consider the same type of membrane, which is always new when an experiment is started.

When referring to the different sections of the device, the following nomenclature is used (see Figs. 4.7 and 4.15 for pictorial representations):

- (a) “Collar pin” and “collar hole” refer to the two parts of the apparatuses which hold the membrane by means of a press fit: the extraction chamber and bore in the main block of the apparatus, respectively.
- (b) “Supply” refers to the liquid prior to being introduced to the inlet plenum
- (c) “Available gas” refers to the gas introduced to the inlet plenum.
- (d) “Inlet” refers to the cylindrical volume formed by the bore extending the collar hole, the membrane and the boiling surface or bubbler.
- (e) “Extraction” refers to the volume formed by the bore of the collar shaft,

the back of the membrane (integrated scrim) and a Lexan window.

- (f) “Excess” refers to the fluid exiting to a reservoir or drain tube and subsequently to the atmosphere.
- (g) “Stackup” refers to the membrane layers in the apparatus. The porous stainless steel support, polypropylene integrated backing, and the nanofibrous PTFE are each layers as described in section 4.1.

4.1 Properties of the Membrane

Flat sheet membranes were purchased from Sterlitech (Kent, WA USA) and are marketed as a “laminated” PTFE membrane. The laminated membranes consist of a thin layer of polytetrafluoroethylene (PTFE) which contains the pores and is therefore the active layer. The PTFE is not structurally robust and is therefore bonded to a scrim polypropylene (PP) integrated backing which is in the form of a grid as seen in Fig. 4.1. This image shows the back side of the membrane. Through an image analysis

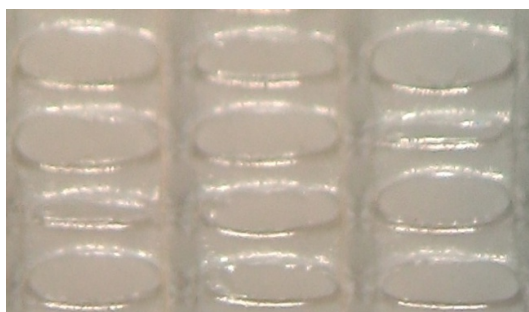


Figure 4.1: Photograph of the PP scrim backing which supports the PTFE nanofibers laminated to it, the PTFE is the material in the ovals. Image is about 3.2 mm wide, viewed with an optical microscope.

code written in the standalone coding platform MATrix LABratory (MATLAB[®]), it was determined that the open area ratio to total area ratio of $28\% \pm 3\%$. Ribs of the membrane are spaced approximately 1.08 mm from rib center-to-center. The web center-to-center spacing is approximately 0.45 mm. Gas flowing through the membrane exits at the integrated backing side.

As seen in Fig. 4.2, the active layers of these membranes are stretched to produce a reasonably uniform pore size, which have specifically been studied by researchers such as Martinez et al. [16] and Saffarini et al. [29]. The fibers between the nodes are about 30-100 nm in diameter as seen in Fig. 4.3. The thickness of the active layer

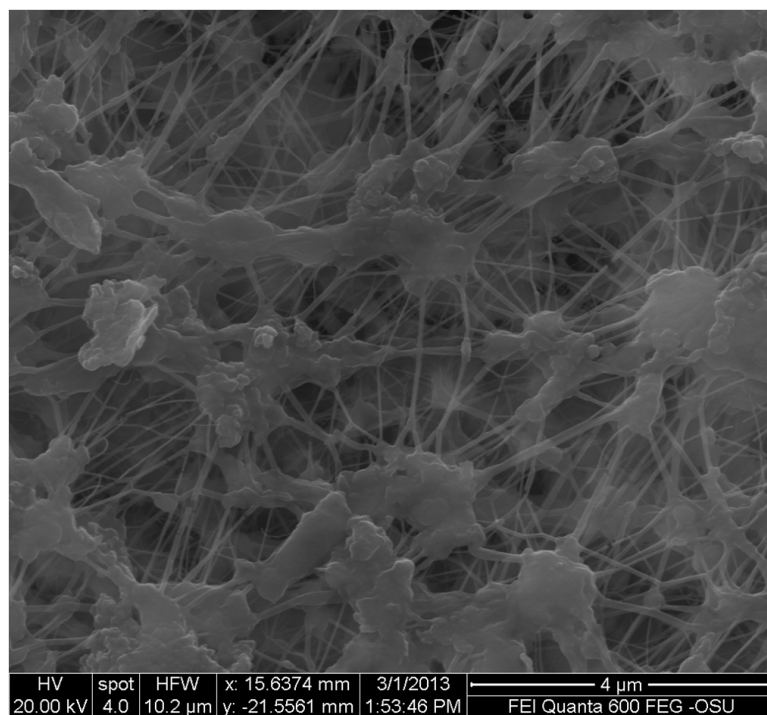


Figure 4.2: Scanning electron microscope image of $0.45\mu m$ diameter pore size. The width of the image, the horizontal field width (HFW), is $10.2\mu m$.

of the membrane is $15.6 \mu\text{m}$. Although a cross-sectional analysis was not conducted, as seen by Adnan et al. [18], assuming the fibers can be approximated as a cubic grid of fibers spaced $0.45 \mu\text{m}$ (equivalent to the pore diameter), there are about 35 layers of pores. The pores are interconnected unlike other types of membranes where each pore remains separate from the others such as that employed by Alexander and Wang [7]. This interconnectivity results in a tortuous path for gas to get from one side of the active layer to the other as will be described in chapter 5. Membranes with interconnected pores have a greater void volume which results in greater porosity. The membrane properties are summarized in Table 4.1.

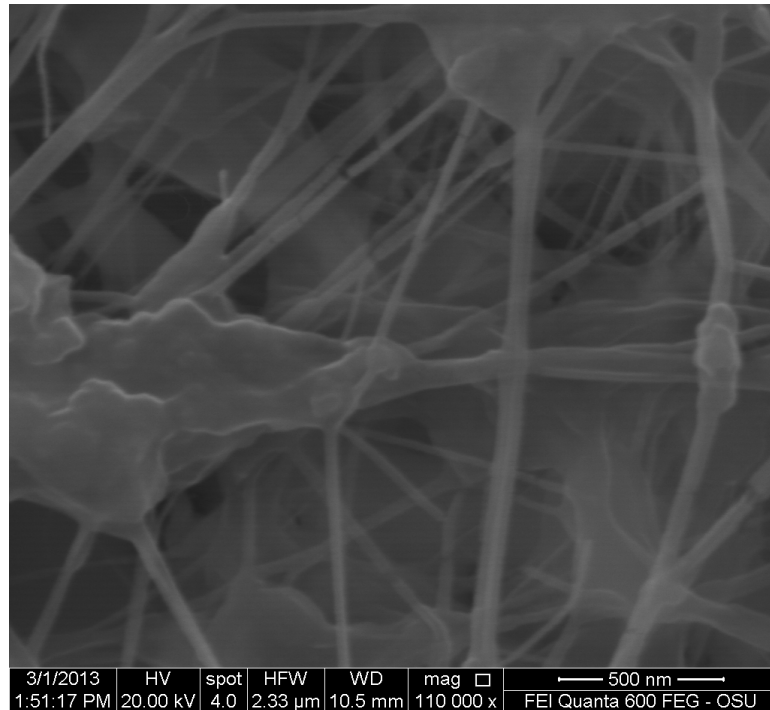


Figure 4.3: Scanning electron microscope image of $0.45 \mu\text{m}$ diameter pore size. The width of the image (HFW) is $2.33 \mu\text{m}$.

Table 4.1: Membrane properties and other details about the membrane stack-up.

Membrane Supplier	d_p (μm) ^a	ϵ_{PTFE}	τ	δ_{PTFE} (μm)	B^b	Integrated Backing
Sterlitech	0.47	0.55	1.82	15.6	0.6	Scrim Polypropylene

a As determined by Martinez et al. [16]

b As determined by Saffarini et al. [29]

4.2 Extraction Chamber

One extraction chamber was used for all types of experiments. As seen in Fig. 4.4, the extraction chamber has multiple fittings in it. Most of these fittings were used to

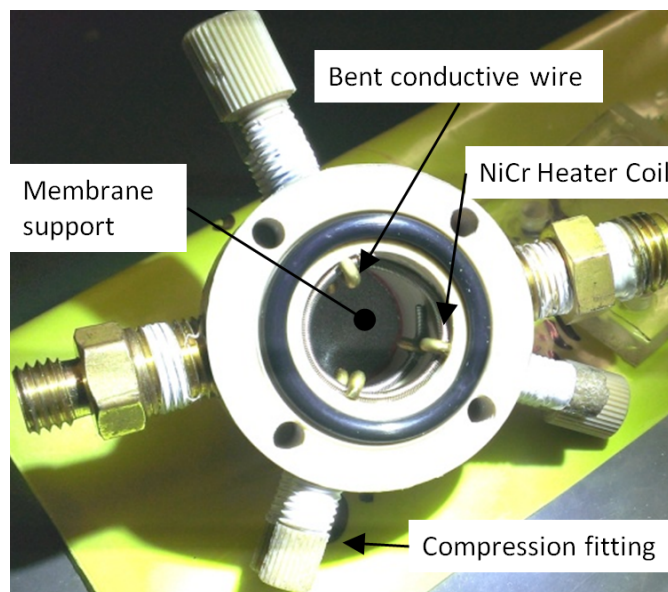


Figure 4.4: Photograph of the extraction chamber with window removed showing NiCr heater coils to keep the gas from condensing. The smaller compression fittings spaced about 120° from each other are holding the heater coil. Only one compression fitting is used for thermocouple mounting (not shown).

hold conductive wire which were bent to wrap around a nickel-chromium (NiCr) resistance heater. There were two wraps of a single NiCr heater coil, and the conductive wire holding the heater extended through the compression fittings so electricity could be supplied to the heater. The conductive wire acted as the male half of the electrical connector; the female half was made of a standard unsheathed crimp connector. The two adapters with hex drives were used for pressure measurements and connection to the condenser, flow meter and vacuum generator.

4.3 Single-phase Experiments

The air and vapor single-phase experimental apparatuses were nearly identical, but made of different materials. The air device was made from acrylic and the vapor device was made from alloy 6061 (A6061) aluminum. As seen in Fig. 4.5, there is an inlet port supplying gas perpendicular to the flow direction through the membrane. There is a

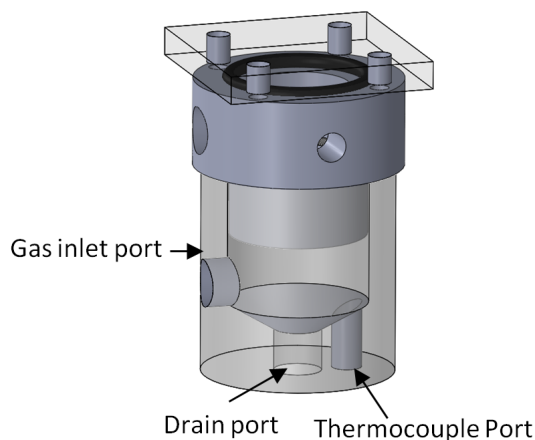


Figure 4.5: Drawing of the superheated vapor and single-phase air apparatus geometry, shown to scale but shown smaller than actual size.

thermocouple port on the bottom of the device tapped to accept a compression fitting, this port is off-axis. There is a drain port which is only open for the superheated vapor case.

4.3.1 Air Apparatus

Of the four apparatuses, the air device is the only truly closed apparatus from supply to extraction. This is achieved by plugging the drain port and is done to ensure the supply air is filtered to reduce the possibility of fouling. The air is filtered to $1\ \mu\text{m}$ in the single-phase air tests, but is filtered more finely with the liquid-air system. The pressure at the inlet plenum is adjusted by means of a pressure regulator fed from a compressed air tank.

4.3.2 Vapor Apparatus

The superheated vapor apparatus was made from a higher melting temperature material than the air device because it had to be heated to keep the vapor from condensing within the apparatus. If condensation formed in the inlet plenum, it dripped out through the drain port which was connected to a short pipe. Not only did the drain port allow for liquid to escape the system, but it also allowed excess supply vapor to “blow-off,” maintaining the pressure in the inlet plenum. This way there was always excess vapor available for extraction and air was not getting pulled in through the drain port. The superheated vapor apparatus in operation is shown

in Fig. 4.6. The vapor was supplied from a boiler and a blow-off valve was cracked open to relieve the pressure in the supply line. The strip heater was powered with alternating current (AC) and a 110 VAC variable transformer. The supply vapor was filtered with an $0.2\ \mu\text{m}$ filter mounted in-line between the boiler and apparatus.



Figure 4.6: Photograph of the superheated vapor apparatus.

4.4 Two-phase Experiments

The two-phase apparatuses required additional sensors and ports to allow liquid to mix with a set amount of gas. These devices have windows to allow visualization of the bubble-membrane interaction. There is a window on each side of the apparatuses. One of the windows was for a light source and the other was for the a high speed camera. There is a port which allows for excess liquid and vapor to exit the inlet plenum. This port was drilled in the apparatus such that when the extraction chamber was installed, the face of the membrane is on-axis with the port. The supply liquid was filtered with an $0.2 \mu m$ filter.

4.4.1 Liquid-Vapor Apparatus

The liquid-vapor device is essentially a pool boiling apparatus. A cross-section of this device is shown in Fig. 4.7. There is an aluminum A6061 heater block at the bottom of the inlet plenum. The circular face of the heater block forms the bottom wall of the inlet plenum and heats the water directly. The heater block is an axis-symmetric part that has six 80 W cartridge heater cavities. The cartridge heaters are resistive elements wired in parallel and powered by an autotransformer. There are three thermocouples in the heater block near the liquid to calculate the heat flux and losses. These thermocouples are far from the cartridge heaters and spaced by 12.7 mm (0.5 in) to reduce the uncertainty in heat flux and wall temperature measurements. The top thermocouple is 2.4 mm (3/32 in) from the boiling surface and the losses are evaluated by a thermocouple at the same depth as the thermocouple closest to the

cartridge heaters, but radially offset 7.6 mm (0.3 in). The material of the main block is Teflon[®]. The liquid-vapor device in operation is seen in Fig. 4.8.

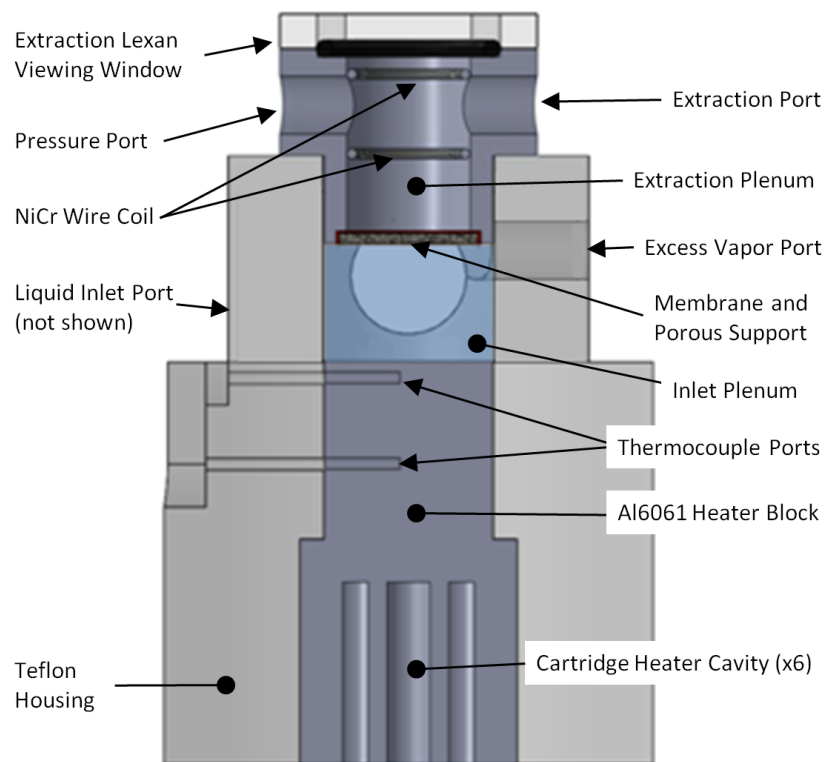


Figure 4.7: Cross-section of the liquid-vapor apparatus, shown to scale.

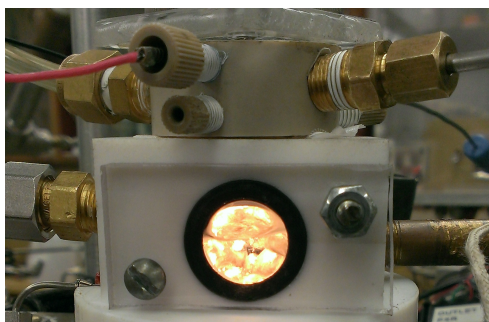


Figure 4.8: Photograph of the upper half of the liquid-vapor apparatus in operation, liquid supply is on the right and excess is on the left.

4.4.2 Liquid-Air Apparatus

The liquid-air device is similar to the liquid-vapor device in the sense that the gas is introduced to the pool at the bottom of the inlet plenum opposite from the face of the membrane. As seen in Fig. 4.9, air is forced through a porous sintered stainless steel bubbler which is very similar to the sintered stainless steel membrane support. The bubbler has a $10\ \mu\text{m}$ mean pore diameter and is 25 mm (1 in) in diameter and 3 mm (1/8 in) thick. Since the available air is measured upstream of the “air inlet port,” the flow path must be sealed until the gas is in the inlet plenum. This is achieved by surrounding the bubbler with an o-ring (inner diameter, ID = 25 mm) which sits in a shoulder in the plate compressing the bubbler. This plate is held against the bubbler by means of two bolts.

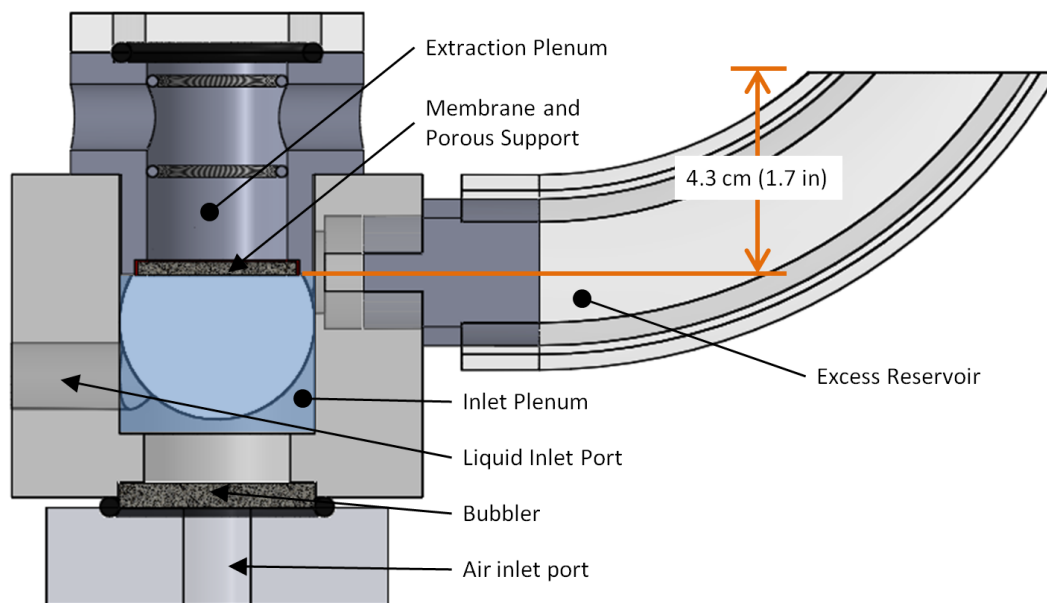


Figure 4.9: Drawing of the liquid-air apparatus cross-section, shown to scale but smaller than actual size.

The main block of the liquid-air apparatus is shown in Fig. 4.10 directly after machining. The bore which forms the hole to press fit the membrane was subsequently sanded and polished. This was important for this device in particular because the block was made of A6061 aluminum and the excess port comes in contact with the membrane. The combination of a hard, sharp surface results in a torn membrane if the excess port had not been smoothed properly. When installing the membrane, it was necessary to twist the extraction chamber as it was seated in the hole and this process could tear the membrane if the hole was not smooth. It should be noted that the excess port in this device was bored to a larger diameter than that of the liquid-air device for reasons explained in section 5.2.

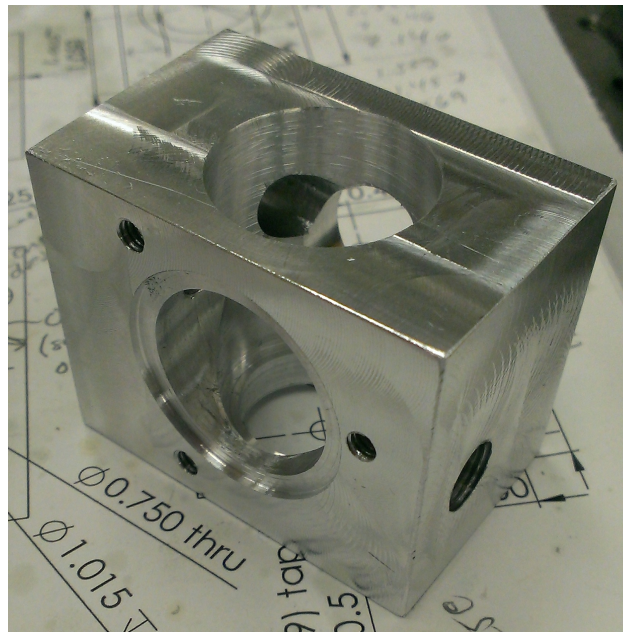


Figure 4.10: Photograph of the liquid-air apparatus main block. The top hole press fits the membrane around the extraction chamber (pin).



Figure 4.11: Photograph of the liquid-air apparatus showing membrane visibility from the front window allowing high speed camera to focus on the face of the membrane.

The assembled liquid-air device prior to operation is shown in Fig. 4.11. The extraction heater is powered and the relative humidity sensor is also heated, but to a lower temperature of 45°C to accurately measure the air mixture's water content by avoiding condensation. The flexible tube between the extraction chamber and the extraction relative humidity sensor also has a rope heater around it during operation. The device in operation is shown in Fig. 4.12. The reservoir is a clear 25 mm (1

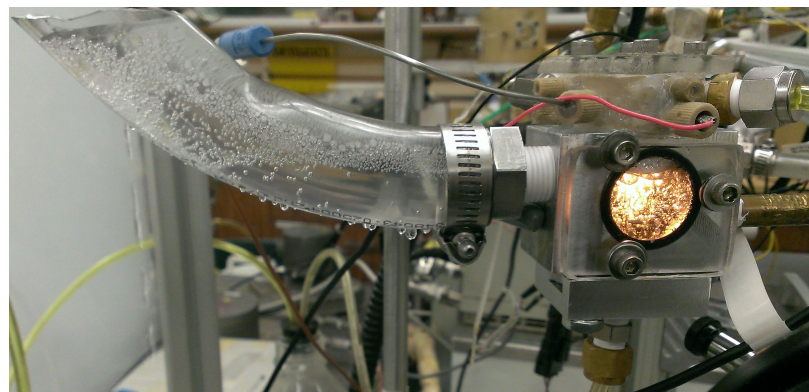


Figure 4.12: Photograph of the liquid-air apparatus in operation, excess liquid drips out of the reservoir.

in) ID vinyl tube which allows the experimenter to see when there is excess gas not being extracted. The reservoir is necessary to eliminate the possibility of air being introduced to the membrane from sources other than the available air. The pressure induced by the height of the water in the reservoir is on the order of 0.5 kPa.

The relative humidity (RH) sensors are capacitive sensors with an accuracy of $\pm 3\%$ RH. These sensors also have a thermistor on their circuit board to correct the relative humidity for temperature. The RH sensors are mounted and sealed in-line by means of custom made sensor blocks as seen in Fig. 4.13 and drawn in appendix G. These sensor blocks suspend the sensing element (under the protective porous stainless steel cap) in the center of the air flow. The sensors are mounted with a compression fitting and was cured adhesive to seal the signal wires. Vacuum grease was applied over the adhesive to eliminate leaks.

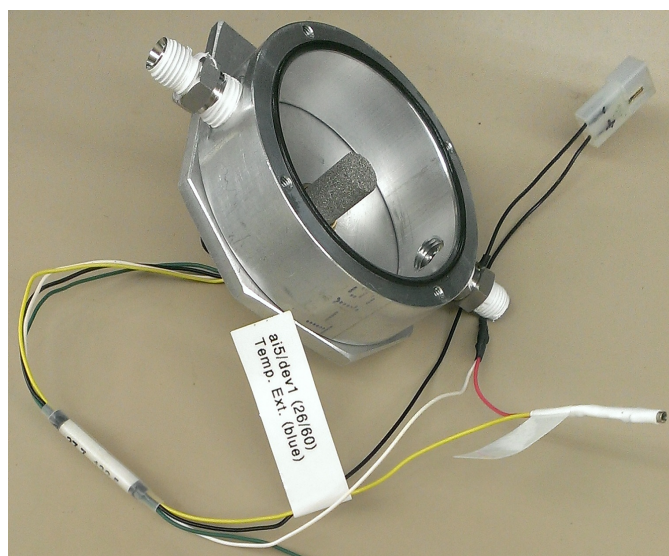


Figure 4.13: Photograph of the relative humidity sensor and mounting chamber for in-line measurement of vapor content in air.

4.5 Procedures

Presented here are a list of procedures for each test device. It was important to assure that neither compaction nor condensation were induced before taking data. All tests employed distilled water as the working fluid; it was commercial grade and purchased in one gallon volumes. The maximum pressure difference across the membrane for all cases was nominally 30 kPa after correcting for the pressure difference in the support as described in section 5.3. The same support was used in all tests, the average pore size of the sintered stainless steel was $10\mu m$ and the thickness was 0.16 cm (1/16 in) with a 1.9 cm (3/4 in) diameter. Some of the area on the support's face was sealed with room temperature vulcanizing (RTV) silicon to form an impermeable barrier between the support and shoulder it rests on as seen in Fig. 4.14. It is assumed that the superficial flow area was equal to the inner diameter of the shoulder, which

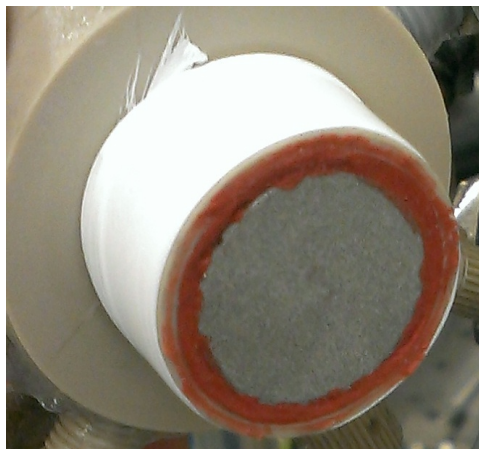


Figure 4.14: Photograph of the membrane support shown adhered to the shoulder of the extraction chamber as seen in Fig. 4.15. Also showing Teflon[®] tape which mates to the scrim integrated backing of the membrane.

was the same diameter as the bore of the extraction chamber. This assumption was visually verified as the RTV did not migrate significantly toward the center of the support.

4.5.1 Pre-test Operations

For all four apparatuses, leak testing was performed before taking data. Leaks in systems are typically tested with a soapy solution that bubbles when the system is pressurized. Since a soapy solution can not be seen bubbling when it is pulled into the system of opaque tubes and fittings, a rotameter with a range of 320 mL/min was placed in-line between the extraction plenum and the vacuum generator. To seal the inlet plenum, the devices were leak tested with liquid blocking flow through the

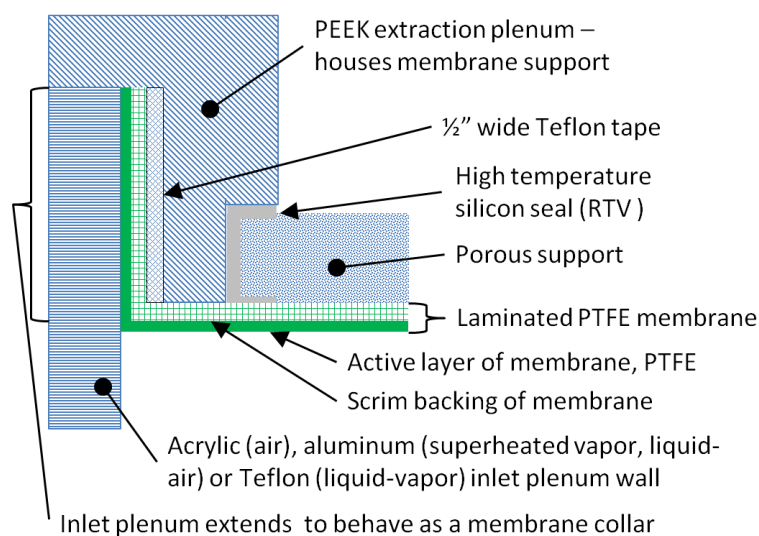


Figure 4.15: Schematic of the membrane mounting method showing the hole and pin forming a press fit to mount the membrane.

membrane. The liquid was deaerated prior to leak testing by boiling vigorously for at least 30 minutes. If the water is not deaerated, a VMD scenario exists and gas will be extracted from the single-phase liquid resulting in gas flow [38]. This flow will be measured by the rotameter and will cause the experimenter to misinterpret a leak. Fittings were tightened with Teflon[®] tape between the male and female threads. The shaft mounting the membrane was wrapped in 3-5 layers of Teflon[®] tape which mated to the integrated backing of the microporous membrane as seen in Fig. 4.15. Once the membrane was installed and deaerated water filled the inlet plenum, a vacuum was applied to the line and if the rotameter read a flow rate, vacuum grease was applied to the most susceptible areas for leaks until the rotameter read zero flow rate. This is not a convenient method since the user must guess where the leak originates, but it was found that the most susceptible areas for leaks are the following:

1. Between the shoulder of the extraction chamber and the top of the main block of the apparatus
2. The signal wires leading out of the relative humidity sensors
3. Improperly deaerated water
4. Flow meters - the transducer was found to have a limit of about 40 kPa before flow was detected

Once leaks were removed from the system, the leak testing membrane was replaced with a new membrane in case there were changes due to compaction or condensation. When installing the new membrane, vacuum grease was re-applied to the susceptible areas found in the leak testing step. It was crucial to keep the vacuum grease away

from the face of the membrane as would migrate and clog the pores. Furthermore the vacuum grease was kept away from the sintered stainless steel support.

In all of the experiments, data was continuously recorded, but a steady state start and end mark for each data point was identified using LabVIEW. There were two computers when working with vapor as the gas because the scales measuring gas extraction were not interfaced with the main computer. Pressure and temperature were measured in the inlet and extraction plenum. Pressure was also measured upstream of all rotameters. Further measurements were required for heat flux and losses calculations as well as for relative humidity. The high speed camera was only used in the two-phase experiments, but was set up such that it did not move through the test. It looked up at the membrane at a 30° angle.



Figure 4.16: Photograph of the extraction chamber after removal from an apparatus to show membrane press fit and vacuum grease on shoulder.

4.5.2 Single-phase Air

The single-phase air flow loop is shown in Fig. 4.17. The pressure measured at P_1 is held at 1 atm. using a regulator. This pressure was set after adjusting the venturi to increase or decrease the vacuum. Once the pressures stabilized, the flow rate was visually measured with the rotameter and recorded in Microsoft[®] Excel. The steady state data case was started in LabVIEW to measure temperatures and pressures. After at least 30 seconds of data capture, the steady state marker was set to an end point in LabVIEW and the vacuum pressure was adjusted for the next data point. This continued until the pressure difference across the active layer of

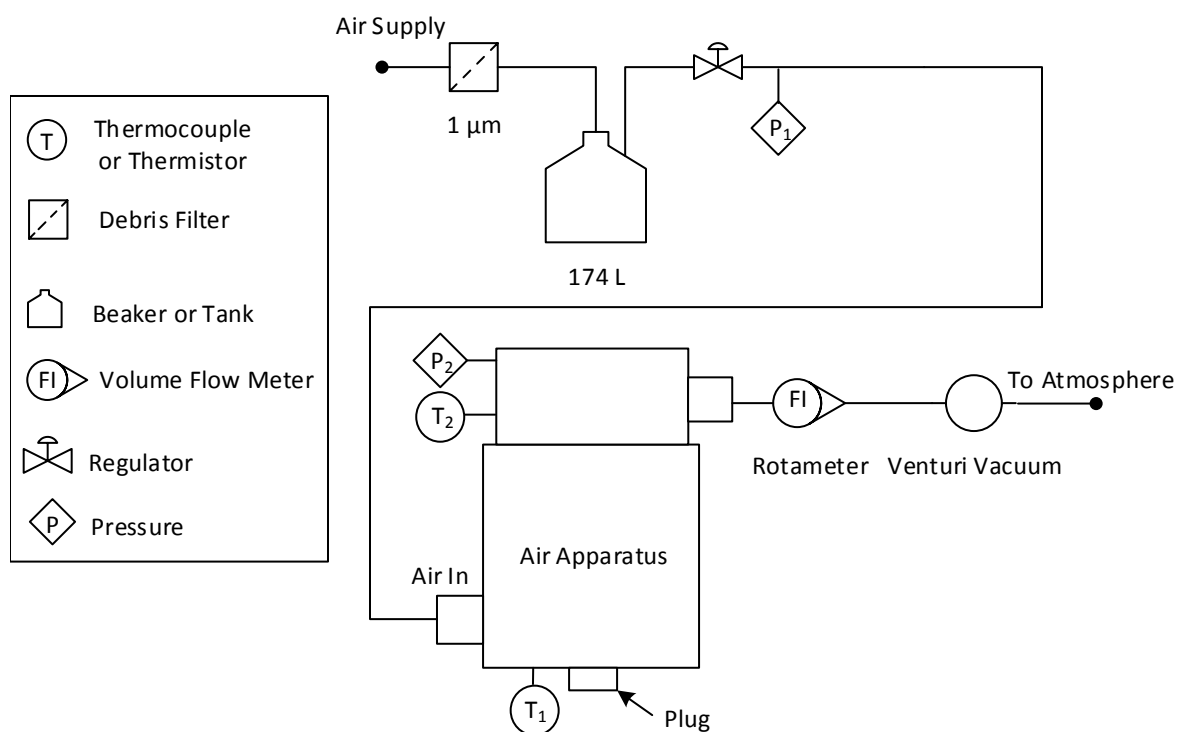


Figure 4.17: Schematic of the single-phase air flow loop.

the membrane increased from 0 kPa to 30 kPa. The pressure difference across the active layer of the membrane is determined by subtracting the pressure difference through the support from the total pressure difference across the membrane stackup as described in section 5.3. The pressure difference was then decreased to 0 kPa to complete a pressure cycle. This pressure cycling was repeated to determine if compaction resulted in permanent changes in the membrane's structure as described in section 5.5.2.

4.5.3 Single-phase Vapor

As seen in the flow loop of Fig. 4.18, the superheated vapor test had sensors similar to those in the single-phase air test. The major difference was that the vapor needed to be condensed and collected in a beaker to determine the mass flow rate of extraction. Therefore, steady state times were longer than those for air. Once the boiler was up to temperature and water boiled such that vapor was being released at the boiler-to-atmosphere valve, the operating procedures were as follows:

1. Flow coolant through condenser (tap water)
2. Turn supply vapor strip heater on
3. Turn extraction chamber coil heaters on and set extraction temperature to 120°C
4. Open vapor supply line blow-off valve completely
5. Introduce steam to the "Vapor In" line by opening the in-line valve and closing

the boiler-to-atmosphere valve

6. Once steam is flowing out of the drain port:
 - (a) Adjust strip heater power to evaporate liquid off thermocouple T_1 and get temperature to 110°C
 - (b) Close blow-off valve or leave it cracked
 - (c) Pull vacuum for maximum pressure difference required

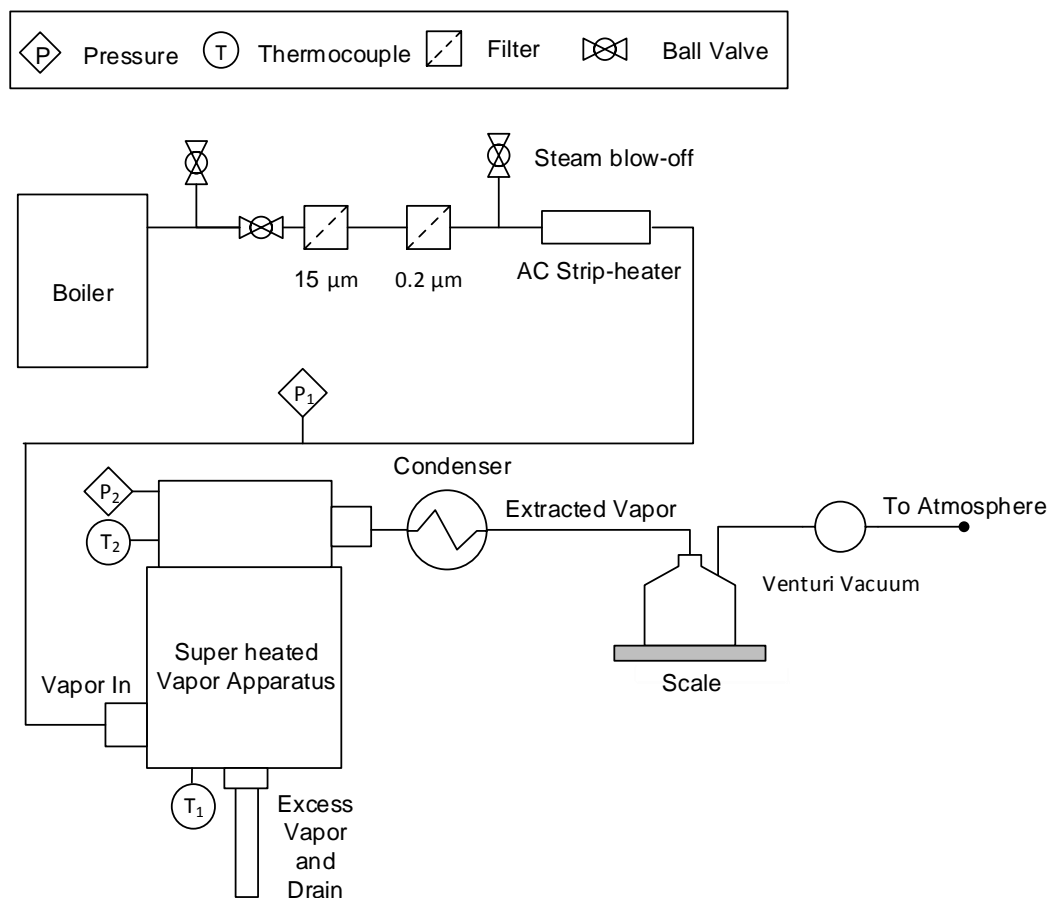


Figure 4.18: Single-phase superheated vapor flow loop

(d) Open blow-off valve such that steam is slowly exiting the drain port

7. Start taking data

8. When pressure is adjusted, the power to the extraction heater needs to be adjusted to keep the chamber at 120°C

Note that this procedure either required previous knowledge of the blow-off valve setting to make sure there was excess vapor when the maximum pressure difference was applied so air was not pulled into the apparatus from the atmosphere. The experimenter could also omit the first cycle of data by starting at the highest pressure difference as described in the list of procedures above.

4.5.4 Liquid-Vapor

As was mentioned previously, the liquid used for the supply needed to be deaerated. Once this was complete, these steps were followed:

1. Flow coolant through condenser (tap water)
2. Turn on hot water bath and liquid pre-heaters
3. Turn extraction chamber coil heaters on and get chamber to 120°C
4. Introduce liquid flow to the system, set mass flow rate at 10 g/min with needle valve
5. Supply power to cartridge heaters in heater block; experimenter estimates the power required based on energy balance, measure power with oscilloscope or multimeter

6. Once temperatures in heater block have stabilized, start taking data
7. When pressure is adjusted, the power to the extraction heater needs to be adjusted to keep the chamber at 120°C
8. Steady state times will need to be longer at lower flow rates (at low pressure differences), sometimes as long as 10 minutes

During transients between steady state data points, the absence of liquid build-up on the stainless steel support was visually verified. If there was liquid build-up on the support as seen in Fig. 4.19, the thermocouple would show a temperature decrease on the live LabVIEW program. The power to the coil heaters (typically 10-15 W) was increased to evaporate the liquid if this occurred. The temperature only decreased when the pressure difference was increased, because the vapor flow rate increased which resulted in a higher heat transfer coefficient.

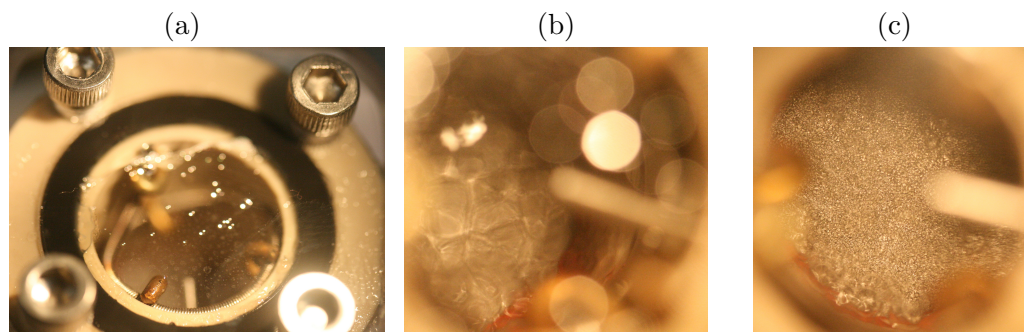


Figure 4.19: Photographs of liquid-vapor extraction chamber showing water on the porous support, this condition only existed in transients between data points; the liquid had to be evaporated before capturing steady state data. The extraction chamber thermocouple is shown protruding into the chamber (out of focus). (a) Reference image for point of view; note that liquid drops on the window only showed up when there was a small pool of liquid; (b) start-up condition if extraction heater is not turned on prior to extracting vapor; (c) liquid layer at the perimeter of the support.

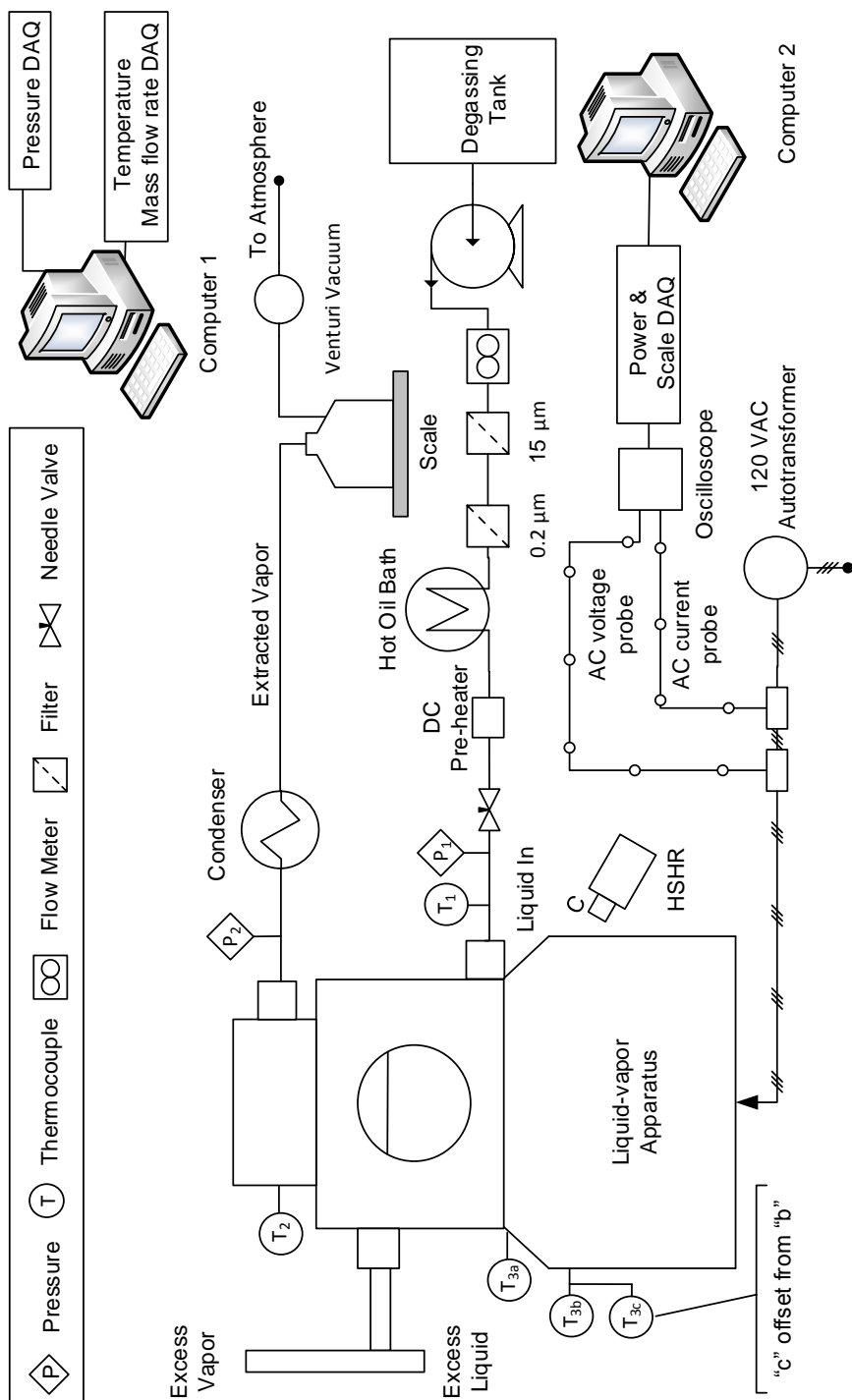


Figure 4.20: Schematic of the liquid-vapor flow loop.

Note that in Fig. 4.21, the extraction pressure transducer is mounted in the extraction port opposite from the extraction line instead of in-line with it. When the liquid-vapor extraction pressure is monitored with this transducer here, liquid condenses in the flexible tube leading the the transducer. This only occurs in the liquid-vapor case because the extraction plenum is filled with vapor. This was found to result in a drop of liquid falling onto the membrane support when the pressure difference increased, so the system was not to set up this way. The extraction pressure transducer P_2 was placed between the extraction chamber and the condenser, in-line with the extraction line. The port opposite the condenser port was plugged.

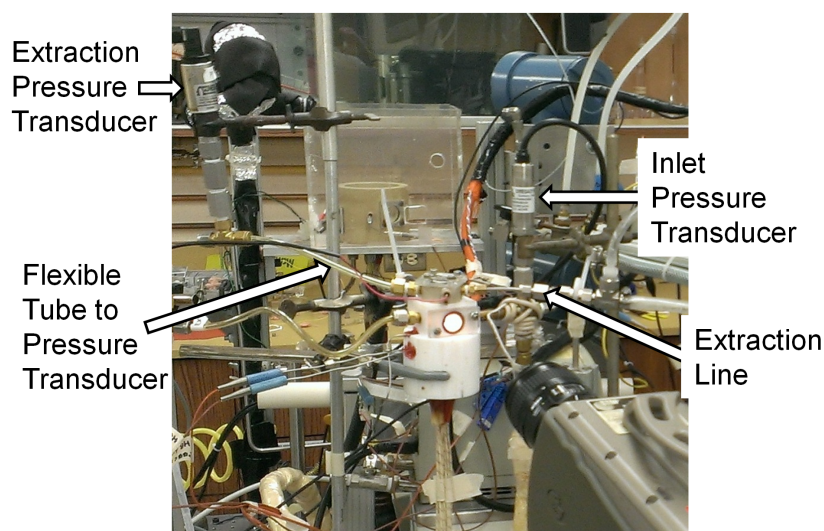


Figure 4.21: Photograph of the liquid-vapor apparatus in operation showing the extraction pressure transducer in a location which results in drops of water on the membrane support.

4.5.5 Liquid-Air

The flow loop for liquid-air tests is seen in Fig. 4.23. The liquid-air procedures are similar to those of the liquid-vapor tests except the liquid was not heated prior to entering the apparatus. The liquid-air procedures were as follows:

1. Turn extraction chamber coil heaters on and get chamber to 85°C
2. Introduce liquid flow to the system, set mass flow rate to 10 g/min with needle valve
3. Set the inlet rotameter to desired flow rate, adjust for pressure (typically 110 kPa); this rotameter will need to be monitored through test as the bubbler resistance changes due to bubble dynamics
4. Once relative humidity values have stabilized, start taking data
5. When pressure is adjusted, the power to the heaters needs to be adjusted
 - (a) Extraction heater adjusted to keep the chamber at 85°C
 - (b) Rope heater around RH_3 adjusted to keep the sensor at 45°C
6. Record steady state data; if recording the extraction flow rate with a rotameter, take videos (320 x 240 pixels is sufficient) of the of the float

Part of the physical liquid-air flow loop is seen in Fig. 4.22. In this picture, the flow rate transducer is seen with a ribbon carrying the signal data to the monitor above the power supplies. The extraction relative humidity sensor (RH_3) is more visible here, it is shown with insulation around it. Rope heaters are between the insulation and the aluminum housing of the sensor block. The white tube exiting this

relative humidity sensor is a desiccant filter. The high speed camera is shown angled up at the membrane at approximately 30° .

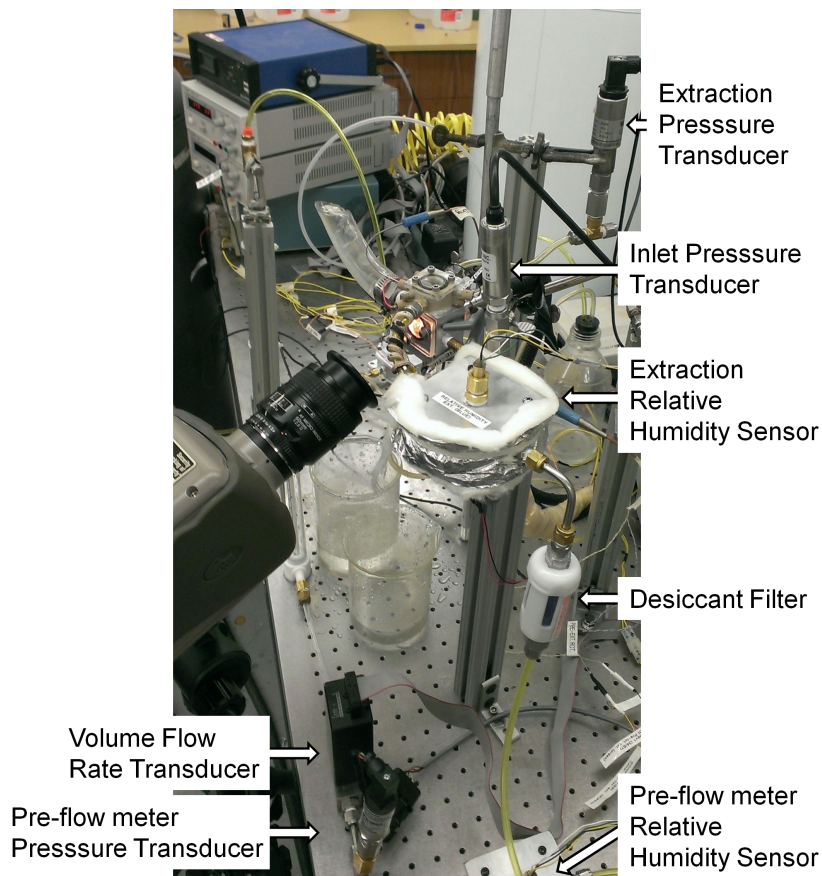


Figure 4.22: Photograph of the liquid-air apparatus in operation showing sensors and power supplies, measuring extracted air with flow meter transducer upstream of a rotameter.

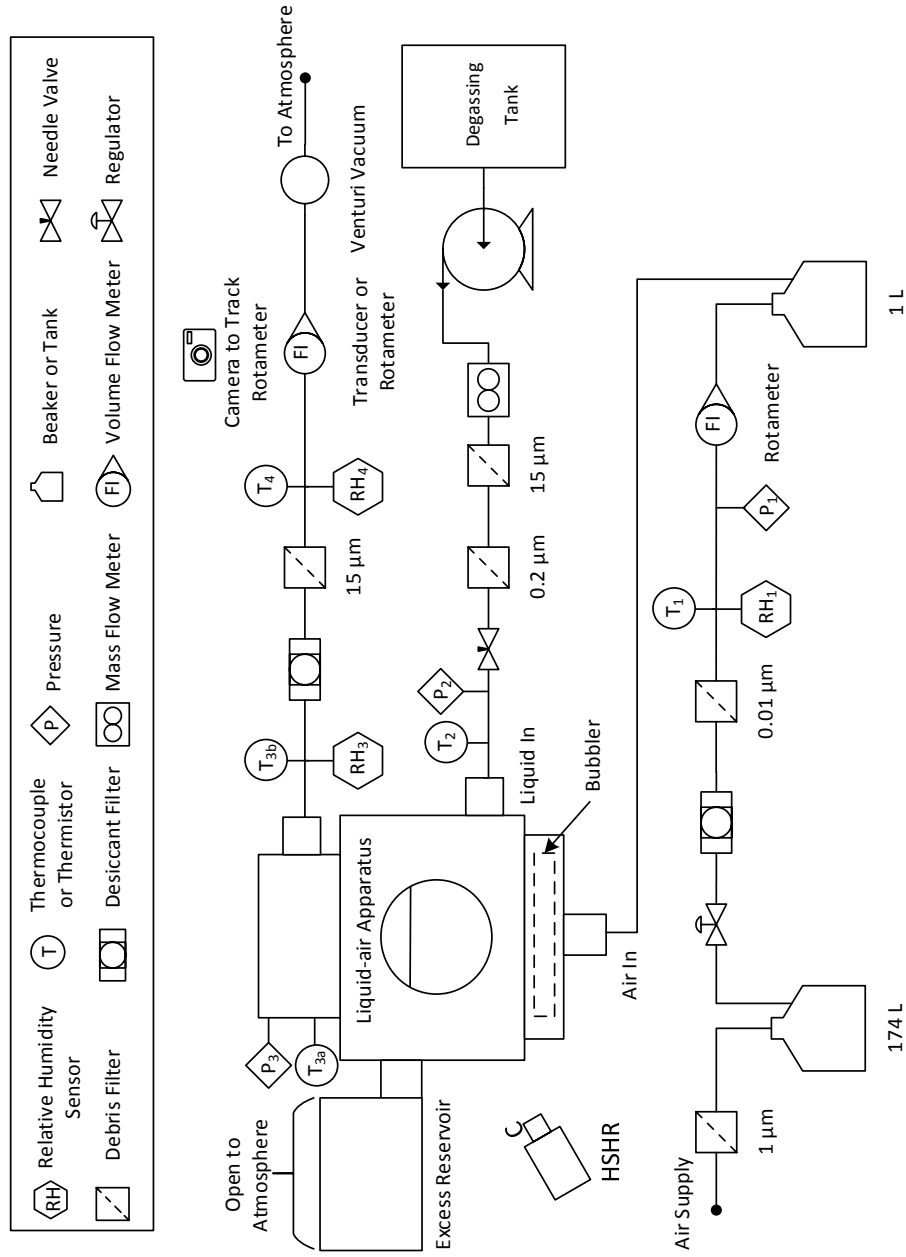


Figure 4.23: Schematic of the liquid-air flow loop; single-phase air flow loop is similar but does not include desiccant filters or 0.01 μm filter (just 1 μm filter).

4.6 Cases Studied

Table 4.2: Single-phase and two-phase cases, some cells are empty because these variables are not applicable to the specific data case. Values are averaged over all data points in test.

Phases	Available Flow Rate			Fluid Temp. (°C)				$\dot{m}_{v,avail.}$ (g/min)	RH _{avail.} (%)	$\dot{m}_{i,supply}$ (gpm)	P _{inlet} (kPa)	T _{g,ext.} (°C)	T _{g,RH ext.} (°C)
	$\dot{m}_{avail.}$ (gpm)	Q _{avail.} (mL/min)	T _{i,supply}	T _{g,avail.}	T _{i,supply}	T _{g,avail.}	T _{g,ext.}						
Air, Support				25	25	102	20-50						
Air				22	22	102	20-50						
Liquid-Air	0.13	99	24	20	84	101	17	3.0E-04	10	10	101	45	45
Liquid-Air	0.26	195	26	21	85	101	18	6.6E-04	10	10	101	46	46
Liquid-Air	1.63	1208	22	18	83	101	14	2.6E-03	10	10	101	45	45
Liquid-Air	2.37	1733	31	19	82	100	16	4.6E-03	10	10	100	46	46
	$\dot{m}_{avail.}$ (gpm)	Q _{avail.} (mL/min)	T _{i,supply}	T _{g,avail.}	T _{g,ext.}	P _{inlet} (kPa)	$\dot{m}_{i,supply}$ (gpm)	q'' (W/cm ²)	Quality	T _w (°C)			
Vapor, Support				100	98	101							
Vapor				110	120	102							
Liquid-Vapor	0.26	436	76	100	119	100	10	5.6	10	10	100	110.6	110.6
Liquid-Vapor	0.72	1208	72	100	118	100	10	9.4	10	10	100	113	113
Liquid-Vapor	0.98	1644	75	100	118	99	10	11.1	10	10	99	115.7	115.7
Liquid-Vapor	1.38	2315	74	100	120	100	4	12.2	4	4	100	111.7	111.7
Liquid-Vapor	1.55	2601	71	100	120	100	10	16	10	10	100	118.4	118.4

4.7 Thermo-physical Fluid Properties

The fluid properties used are listed in Table 4.3. These constants were used to predict flow rates from Darcy's Law and the dusty gas model. When post-processing data in MATLAB[®], table lookups, the Sutherland law and ideal gas law were used to determine fluid properties.

Table 4.3: Thermophysical properties at nominal temperatures.

	Inlet Plenum			
Fluid:	Vapor	Liquid-vapor	Air	Liquid-air
Temperature:	110°C	100°C	25°C	25°C
μ_l (N-s/m ²)		2.82E-04		8.90E-04
μ_v (N-s/m ²)	1.26E-05	1.23E-05	1.83E-05	1.83E-05
ρ_l (kg/m ³)		958		998
ρ_g (kg/m ³)	0.58	0.6	1.2	1.2
σ (N/m)		0.059		0.072

	Extraction Plenum			
Fluid:	Vapor	Liquid-vapor	Air	Liquid-air
Temperature:	120°C	120°C	25°C	85°C
μ_v (N-s/m ²)	1.30E-05	1.30E-05	1.83E-05	2.10E-05
ρ_g (kg/m ³)	Table values	Table values	Ideal Gas	Ideal Gas

Chapter 5 – Data Reduction and Analysis

As shown in the flow loops (Figs. 4.20 and 4.23) there were data obtained with pressure transducers, thermocouples, flow meters and relative humidity sensors. One computer with a data acquisition board (DAQ) was used to record the majority of the signals from these sensors using a program written in LabVIEW. More details on the structure of the program can be found in Sabo's thesis [39]. Data were recorded at approximately 10 Hz such that all sensors had the same number of data points recorded. Since steady state values are desired, all of the data points within each steady state period were averaged. Single-phase steady state and two-phase liquid-air periods of steady state data collection were typically at least one minute. However, liquid-vapor steady state periods were at least five minutes because the flow rate was lower and must be determined using the catch-and-weigh method. The scale data for catch-and-weigh was recorded with a second computer. The scales used to calculate the mass flow rate of extracted vapor were precise enough to require reasonably short steady state periods on the order of one minute, but the vapor formed slugs of water when moving from the extraction chamber to the scale through the condenser. These slugs of water were not spaced very far from each other, but since they moved slowly, they resulted in a stepped mass-time response. Therefore, longer periods of data were taken to provide a better linear curve fit when calculating the mass flow rate.

5.1 Gas Available For Extraction

The mass flow rate of gas available for extraction was held constant for each experiment. For the liquid-air and single-phase air studies, a rotameter was installed upstream of the gas inlet port as seen in Figs. 4.17 and 4.23. The pressure and relative humidity were monitored at the inlet of the rotameter in the case of liquid-air tests. The humid volume flow rate was determined by correcting the flow rate reading for the higher pressure with

$$Q_{actual} = Q_{read} \sqrt{\frac{P_{atm}}{P_{inlet}}} \quad (5.1)$$

where the volume flow rate of the float at atmospheric pressure (P_{atm}) and non-atmospheric pressure (P_{inlet}) are Q_{actual} and Q_{read} , respectively. Since the rotameter's calibration curves are based on a 1 atm. inlet pressure. The volume flow rate was then converted to a mass flow rate by multiplying by the density of the mixture. The density depends on the vapor content in the air, as measured with the relative humidity sensors. With the relative humidity known, the humidity ratio, ω , was calculated with

$$\omega = \frac{m_v}{m_a} = 0.622 \frac{p_v}{P - p_v} \quad (5.2)$$

where P is the pressure of the mixture and the mass of water vapor and air are m_v and m_a , respectively. The water vapor partial pressure, p_v , was calculated knowing the relative humidity of the mixture, Φ , with

$$p_v = p_{v,sat} \Phi \quad (5.3)$$

where $p_{v,sat}$ is the saturation pressure of water.

With the humidity ratio known, the specific volume of the mixture, v_{mix} , was calculated with

$$v_{mix} = \frac{V_{mix}}{m_a + m_v} = \frac{V_{mix}}{m_a (1 + \omega)} \quad (5.4)$$

where the ratio of the volume of the mixture to the mass of the air, $\frac{V_{mix}}{m_a}$, is defined with the ideal gas law

$$v_{da} = \frac{V_{mix}}{m_a} = \frac{R_a T}{P - p_v} \quad (5.5)$$

where v_{da} is the specific volume of dry air if it were to take up the total volume of the mixture. The gas constant of air, R_a , is equal to the ideal gas constant, R , divided by the molecular weight of air, M_a . Eq. (5.5) was substituted into Eq. (5.4) to determine the specific volume of the mixture, v_{mix} , and therefore the density, ρ_{mix} , as

$$\rho_{mix} = v_{mix}^{-1} = \left[\frac{R_a T}{(P - p_v) (1 + \omega)} \right]^{-1} \quad (5.6)$$

The humidity ratio, Eq. (5.2), is defined as the mass ratio of vapor to air and therefore was used to determine the mass flow rate of each specie once the mass flow rate of the mixture was known. The mass flow rate of air is

$$\dot{m}_a = \frac{\dot{m}_{mix}}{1+\omega} \quad (5.7)$$

and that of vapor is

$$\dot{m}_v = \dot{m}_{mix} - \dot{m}_a \quad (5.8)$$

The available vapor in the liquid-vapor experiments was calculated with an energy balance

$$\dot{E}_{in} = \dot{E}_{out} \quad (5.9)$$

where the control volume was the inlet plenum. The energy entering and exiting the control volume was determined knowing the enthalpy of the fluid entering the control volume, $h_{f,in}$, and the heat entering the volume, Q_{in} , with

$$h_{f,in}\dot{m}_{in} + Q_{in} = h_{out}\dot{m}_{out} \quad (5.10)$$

where the mass flow rates of fluid exiting and entering the control volume, \dot{m}_{out} and \dot{m}_{in} respectively, were equal to each other. To determine the heat supplied to the control volume, the heat flux entering the control volume from the top face of the heater block (the “wall”) was calculated assuming 1-D conduction between the two thermocouples in the heater block near the wall. This 1-D assumption is reasonable because the thermocouples are sufficiently spaced from the cartridge heaters supplying the heat to the heater block, as seen in Fig. 4.7. The 1-D assumption was verified by monitoring the radial temperature variation (if any) 3/5 of the radius out from the axis

of the heater block. If the temperature at this radial location was slightly lower than the axial temperature at the same distance from the wall, an axis-symmetrical nodal analysis was implemented to approximate the losses. The boundary conditions for the nodal analysis consist of a constant temperature at the wall and linear temperature profiles along the radius and through the height of the cylinder at the perimeter. Accounting for losses results in a lower heat input, Q_{in} , and is substituted directly into Eq. (5.10).

The 1-D conduction equation

$$q'' = \frac{k_{al}(T_1 - T_2)}{\delta_{TCs}} \quad (5.11)$$

requires the thermal conductivity of the (aluminum) heater block, k_{al} ($167 \frac{W}{m \cdot K}$), the thermocouple temperatures, T_1 and T_2 , and the thermocouple spacing, δ_{TCs} to calculate the heat flux, q'' .

The heat flux was simply converted to power with the knowledge of the area it passes through as

$$Q_{in} = q'' A_{wall} \quad (5.12)$$

where A_{wall} is the area of the wall. The energy balance Eq. (5.10) was rearranged to isolate the enthalpy of the mixture leaving the control volume, h_{out} :

$$h_{out} = \frac{h_{f,in} \dot{m}_{in} + Q_{in}}{\dot{m}_{in}} \quad (5.13)$$

The enthalpy of the mixture leaving was used to calculate the quality of the mixture

with the knowledge that there is vapor in the mixture

$$x = \frac{h_{out} - h_{f,sat}}{h_{fg}} \quad (5.14)$$

The quality was simply multiplied by the supply mass flow rate of liquid

$$\dot{m}_{avail.} = x\dot{m}_{in} \quad (5.15)$$

to determine the generated vapor, henceforth referred to as the “available gas.”

5.2 Extracted Gas

The extracted gas was measured because phenomena are limiting the gas transport through the membrane as described in chapter 3. The same measurement method for determining the inlet flow rate of air was used to calculate the extracted flow rate of air. The one difference with the extracted air is that it was more humid. Rotameters are not calibrated to humid air and do not perform optimally when measuring humid air because the float may stick to the tapered tube it is contained in. Therefore, the air must be dried before its flow rate is measured. Referring to the flow loop Fig. 4.23, there must be a desiccant filter in-line upstream of the extraction rotameter. The humid air’s vapor content was measured prior to the desiccant filter and again prior to the extraction rotameter because the filter was not able to remove all of the vapor. To determine the mass flow rate of the humid air, the mass flow rate of the *air alone* before and after the desiccant filter was equated. This value was calculated based

on the rotameter's reading of the dry extracted air with Eq. (5.7) where the pressure after the desiccant filter was used. Then the humidity ratio of the wet extracted air from Eq. (5.2) was used to determine the mass flow rate of the vapor alone with Eq. (5.8) - this was done using the temperature measured in the relative humidity sensor and the pressure of the extraction chamber upstream of the desiccant filter. Based on this, the mass flow rate of the mixture, \dot{m}_{mix} , was determined by simply adding the two species' mass flow rates

$$\dot{m}_{mix} = \dot{m}_a + \dot{m}_v \quad (5.16)$$

In the case of the single-phase air case, the relative humidity was not measured and therefore the density of dry air was used to calculate the mass flow rate of the mixture. As the air passed through the membrane, the water content did not change in this test because it was a closed system. Furthermore, as will be shown later, the *volume* flow rate of the mixture, not the mass flow rate, is of importance in Darcy's Law. Because of this, it was important to use the correct fluid properties when determining the extracted volume flow rate in the liquid-air experiments. Since the air was cooling down as it flowed through the extraction loop, the temperature of the extraction chamber was used to calculate the density using Eq. (5.6). This allowed the volume flow rate at the rotameter to be converted to the volume flow rate through the heated membrane. The pressure in the extraction chamber was assumed equal to the pressure in the relative humidity sensor upstream of the desiccant filter because there was no source of a significant pressure drop such as that induced by

the desiccant filter.

When measuring the extracted air in the liquid-air experiments, the extraction flow rate varies substantially since the rotameters are precise enough to measure the flow rate of individual bubbles. Even though the flow rate of multiple bubbles over the period of time will average to a value, the rotameter provides an instantaneous reading and therefore must be recorded as a function of time. For the 1.67 g/min and the 2.37 g/min liquid-air cases, rotameters are used because a flow rate transducer for the range of extraction flow rates was not available in the facility. To determine the volume flow rate as a function of time, a low resolution video (320x240 pixels) was recorded with a digital camera at 30 fps. The videos are typically longer than 30 s and the rotameter float was tracked with MATLAB[®]. An example of the output was shown in Fig. 5.1. If the float could not be tracked because it was moving too quickly and therefore difficult to place, the data point was omitted from the average flow rate calculation.

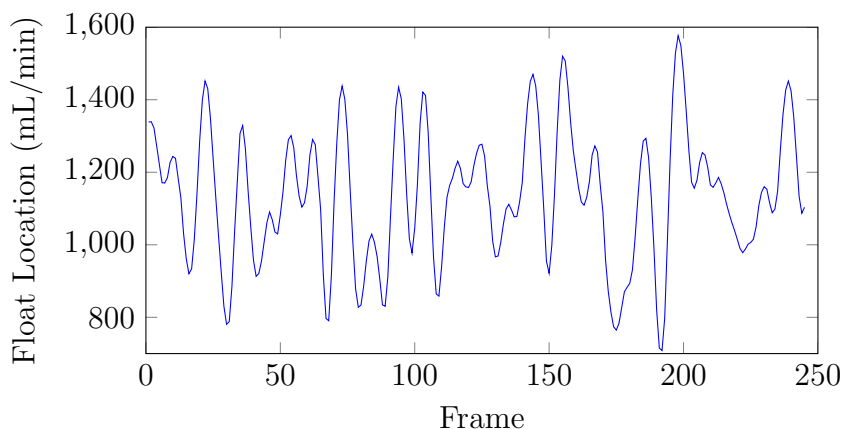


Figure 5.1: Extraction volume flow rate of air as a function of time calculated with an image analysis program of a video of the rotameter output.

In the case of the 0.13 g/min and 0.26 g/min liquid-air experiments, a flow rate transducer was used to produce a curve like the one in Fig. 5.1. The flow rate transducer outputs a voltage which corresponds to the volume flow rate.

The extraction mass flow rate of vapor is a more simple calculation than that for the air because there is only one specie for which to account for. The flow rate measurement method used was catch-and-weigh where a scale recorded the mass of condensed vapor over a period. To determine the mean mass flow rate over a steady state period of data, linear regression analysis was applied to find the slope of the line which corresponded to mass per time. The resulting value was the extracted mass flow rate. For high mass flow rates, approximately one minute of data capture produced a nearly-linear curve when plotting as mass against time. To produce a similar curve at lower flow rates required a longer period of data capture, sometimes up to ten minutes. Even with a long period of data capture, the data could be thrown off by a droplet immediately after or before the data capture region begins or ends respectively. In this case, the steady state period does not account for the droplet in post processing. All cases have some data points at low mass extraction, because for a low pressure difference across the membrane, there was a resulting low extraction rate. Once the extracted mass flow rate was known, it was converted to a volume flow rate using the temperature and pressure in the extraction chamber.

5.3 Trans-membrane Pressure Drop

The active layer of the membrane is termed the “lamine” by the suppliers of microporous nanofibrous membranes. This layer is not rigid and is very thin and therefore must be supported by other layers of material. As more layers are stacked up, the pressure difference increases and therefore the additional (inactive in regards to gas separation) layers must be subtracted from the total recorded pressure difference of the membrane stackup. The pressure difference across the membrane’s polypropylene (PP) integrated backing was found to be negligible as it was within the uncertainty of the pressure transducers. The pressure drop of the porous sintered stainless steel support, ΔP_{sup} , is significant for the flow rates of gas studied here, particularly for the single-phase experiments where mass flow rates are higher. This correction was measured with the sole membrane in the stackup being the porous sintered stainless steel support and a second order polynomial fit was used:

$$\Delta P_{sup} = C_{1,sup}\dot{m}^2 + C_{2,sup}\dot{m} \quad (5.17)$$

where \dot{m} is the mass flow rate of single-phase gas flowing through the support.

When correcting the pressure difference in both the single-phase air and two-phase liquid-air experiments, the pressure drop of gas through the support as a function of mass flow rate was subtracted from the pressure drop of the stackup

$$\Delta P_{PTFE} = \Delta P_{stackup} - \Delta P_{sup} \quad (5.18)$$

where $\Delta P_{stackup}$ is the pressure drop measured during the membrane characterization experiments.

The curve fit as defined by Eq. (5.17) for single-phase air and two-phase liquid-air data corrections is shown in Fig. 5.2a. For both single-phase superheated vapor and saturated liquid-vapor experiments, the pressure drop of *saturated* vapor flowing through the porous support alone is also fit with Eq. (5.17). An example of the resulting correction compared to the pressure difference across only the support is shown in Fig. 5.3.

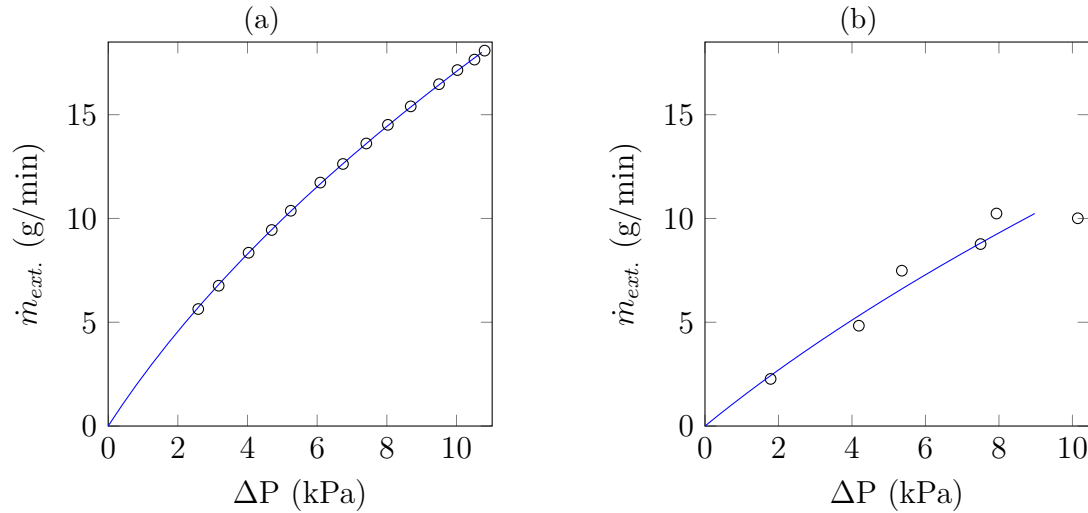


Figure 5.2: Pressure difference across the membrane support with curve fit of the form in Eq. (5.17). (a) Room temperature air $C_{1,sup} = 1.17 \times 10^{-2} \text{ min/g}$, $C_{2,sup} = 3.86 \times 10^{-1} \text{ min}^2/\text{g}^2$ (b) Saturated vapor $C_{1,sup} = 1.81 \times 10^{-2} \text{ min/g}$, $C_{2,sup} = 6.92 \times 10^{-1} \text{ min}^2/\text{g}^2$.

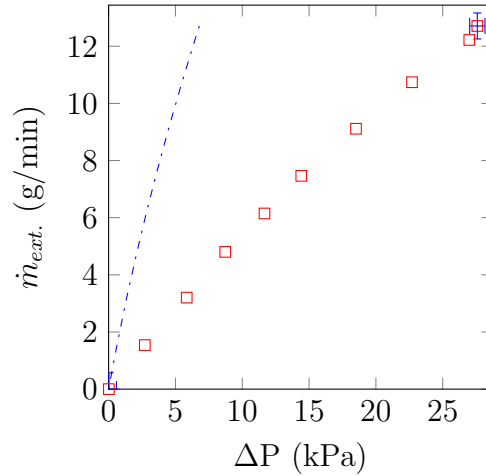


Figure 5.3: Single-phase air data showing the pressure drop across the support (dash-dot line) and the pressure drop across the active layer of membrane (PTFE), \square .

5.4 Pressure Cycles

Data were recorded over two full pressure cycles where the first half of the cycle is defined as an increase in pressure until a maximum is reached. The second half of the cycle begins when the pressure difference begins to decrease from the maximum pressure. Therefore, the minimum pressure defines the beginning or end of the cycle and the maximum pressure is the mid-point of the cycle. To separate the cycles into different sets of data for easier data analysis, the pressure difference across the membrane was monitored in a post-processing code. This was achieved with MATLAB[®] and the code was written to separate and label the data points of each half cycle.

The maximum pressure difference applied to the membrane was less than the LEP. To determine the LEP for liquid-vapor cases, the contact angle was estimated based

on the measured contact angle of liquid-air at 27°C. As introduced in section 2.2.1 and further discussed in appendix B, the contact angle of the liquid-vapor at 100°C was calculated to be 131.9°C which is 2% lower than the liquid-air contact angle at 27°C. A lower contact angle will result in a lower LEP as calculated by the Laplace equation Eq. (2.2) based on the maximum pore size.

Even though Martinez et al. [16] show a pore size distribution which indicates the maximum pore size is about $0.60\mu\text{m}$ in diameter, the pore size distribution is strongly weighted toward the mean pore radius of $0.47\mu\text{m}$ so this value was not used to determine the breakthrough pressure. It should be noted that once the maximum pore size reaches breakthrough, total membrane flooding would not occur unless the pressure was increased to the point where the majority of pores can not withstand the LEP. This is due to the fact that the membrane does not have straight-through pores but instead interconnected fibers. Therefore, if breakthrough does occur, the liquid that enters the membrane will reach what is essentially another pore which has a high probability of being a smaller diameter assuming the pore “layers” are distributed similarly through the thickness of the membrane.

With the pore size for breakthrough established, values can be substituted into the Laplace equation Eq. (2.2) as long as the circular pore shape assumption is accurate. However, as seen in Fig. 4.2, the pores are not circular and therefore a geometric factor B is included in the Laplace equation’s numerator. The geometric factor used here was 0.6 as determined empirically by Saffarini et al. [29] with a similar membrane. Now, an accurate breakthrough pressure can be calculated by substituting the contact angle, surface tension, pore radius and geometric factor into Eq. (2.2). As seen in

Table 5.1, the minimum LEP is over 200 kPa which is much greater than the pressures necessary to achieve full gas extraction and therefore LEP should not be an issue for this study.

Table 5.1: Contact angle and liquid entry pressure of 0.45 μm pore diameter PTFE membranes.

Fluids	$\sigma_{\text{sg,d}}$ (N/m)	σ_{lg} (N/m)	T (°C)	θ_{E} (°)	Φ_{S}	θ^* (°)	B^{b}	$\bar{r}_{\text{p}}^{\text{c}}$ (μm)	LEP (kPa)
Liquid, air	0.0086	0.0718	27.2	108.0	0.43	134.4 ^a	0.6	0.235	257
Liquid, vapor	0.0086	0.0589	100	103.7		131.9			201

a Measured in-house with Sessile drop method

b As determined by Saffarini et al. [29]

c As determined by Martinez et al. [16]

If there are changes in the gas transport as the pressure is cycled, either membrane compaction results in permanent deformation of the fibers or droplets are building up in the pores of the membrane. The droplets could be a result of LEP because when a thin film of liquid exists below a pore, the assumptions applied to the Laplace equation may not be valid.

5.5 Existing Model Modifications for Single-phase Flow

Darcy's Law is an empirical equation, so predicting gas flow rates through microporous membranes is only possible if the membrane permeability is known. The permeability is calculated by rearranging Eq. (2.7) to isolate the permeability shown in Eq. (2.7). This equation makes it evident that if volume flow rates for given pres-

sure differences are provided by the manufacturer, the permeability can be calculated. It is also possible to experimentally generate flow rate - pressure difference curves to calculate the permeability for the specific membrane of interest.

Eq. (2.19) shows that the dusty gas model is not dependent on an empirical coefficient as long as some assumptions are made about the tortuosity as will be discussed shortly. In this study, it is shown later that an empirical coefficient can be implemented to better estimate the mass flux of the extracted gas by accounting for membrane compaction. When applying the DGM, it is important to first determine the flow regime of the gas which is a function of the Knudsen number. When the pore size is large compared to the mean free path of the molecules, the majority of the molecular resistance is due to molecule-molecule interaction which is defined as Poiseuille or viscous flow. When the pore size is small compared to the mean free path of the molecules, the pore-wall interactions dominate and Knudsen flow occurs. As seen in Table 5.2 the Knudsen number ranges have been established for MD applications where diffusion resistance is negligible by [9, 10], as is the case here. As shown in Eq. (2.11), the pore diameter limits increase with decreasing

Table 5.2: Flow regime ranges to determine contributing interactions which resist gas transport through membrane. Mean free path is calculated at 1 atm.

Flow Regime	Kn Range	Pore Diameter (μm)	
		25°C Air	100°C Water Vapor
Knudsen	$\text{Kn} < 0.025$	$\bar{d}_p < 0.005$	$\bar{d}_p < 0.013$
Knudsen-Poiseuille	$0.025 \leq \text{Kn} \leq 25$	$0.005 \leq \bar{d}_p \leq 5.4$	$0.013 \leq \bar{d}_p \leq 12.9$
Poiseuille (ie. viscous)	$25 < \text{Kn}$	$5.4 < \bar{d}_p$	$12.9 < \bar{d}_p$

mean pore pressure as seen in Fig. 5.4. This figure reveals that for air at room temperature and vapor at or just above saturation temperature, the flow regime is in a transition between Knudsen and Poiseuille (viscous) regimes. Therefore, the gas transfer coefficients (B_i^t) of each regime are added together to account for their combined effect on the gas flow (analogous to electrical resistors in parallel, described in section 2.3.2.2) as seen in Eq. (2.19).

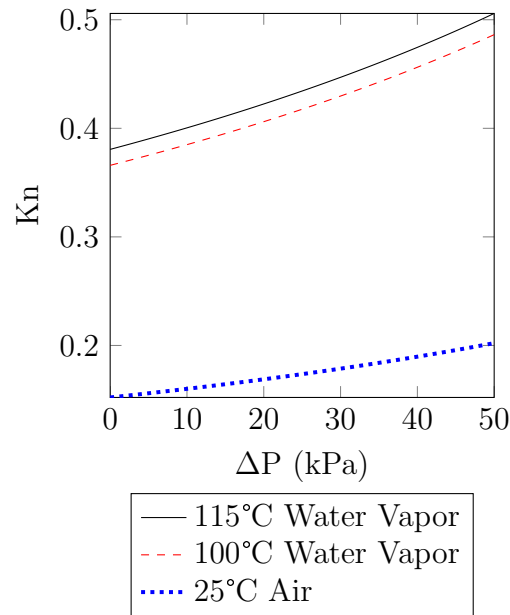


Figure 5.4: Knudsen number as a function of pressure difference across the membrane where the high pressure side is at 1 atm.

5.5.1 Darcy Permeability

When applying Darcy's Law, the only membrane property required is its thickness, which is typically held constant at the non-compacted thickness of the active PTFE

layer ($\delta_o = 15.6\mu m$). To determine the dynamic viscosity of the gas species flowing through the membrane table look-ups are used. For simplicity, when the gas is air the Sutherland equation describes the viscosity well [40], reproduced as

$$\mu_{air} = \mu_o \left(\frac{T}{T_o} \right)^{3/2} \left(\frac{T_o + S}{T + S} \right) \quad (5.19)$$

where $T_o = 273$ K, $S = 110.4$ K and $\mu_o = 1.71 \times 10^{-5}$ kg/(m·s).

The area in Darcy's Law is the flow area. When implementing Darcy's Law to predict flow rates, it is important to use the same reference area, here it is the superficial area as defined by the open area on the face of the porous support in contact with the membrane; it has a diameter of 2.1 cm (13/16 in) which results in a superficial flow area of 3.3 cm². To determine the permeability, the membrane thickness is held constant at $\delta = 15.6 \mu m$. If the membrane does change thickness, those changes will be retained by the permeability. Calculating the permeability is necessary, but less descriptive than capturing changes with other variables as described in section 5.5.2.

The empirical permeability can now be calculated by measuring the volume flow rate Q and pressure difference across the membrane ΔP . While one may be able to find a membrane with the same mean pore diameter as the 0.45 μm PTFE membrane used in this study, without verifying the material or geometry of the pores this permeability could potentially be inaccurate. This is especially true with highly porous polymer membranes like the one used in this study because the modulus of elasticity is low and therefore deformations due to moderate pressures are likely.

5.5.2 Membrane Compaction

Darcy's Law has a membrane thickness parameter which is typically assumed to be constant. If there is a change in permeability as the pressure difference increases, then this change is attributed to compaction. Instead of letting the permeability vary, the thickness can be set as a variable and the permeability can be held constant. This requires an empirical compaction coefficient δ' which is chosen to linearly relate the membrane thickness to the pressure difference applied to the membrane

$$\delta = \delta_o - \delta' \Delta P \quad (5.20)$$

This same relationship was used by Zhang et al. [31] and Lawson et al. [30] as well as Laganà [41] in the studies of DCMD, not VMD. When relevant, the variables with initial "o" subscripts signify the non-compacted values whereas the non-subscripted variables signify a variation which depends on the pressure difference across the membrane.

The constant permeability $K_{D,o}$ is equal to the permeability when there is no compaction. This permeability is determined by fitting a line to the permeability as a function of the pressure difference across the membrane, this is of the form

$$K_D = K_{D,o} + K'_D \Delta P \quad (5.21)$$

A curve fit is required, because the permeability at low pressure differences is typically inaccurate due to the uncertainty in pressure difference. The resulting variable

thickness equation for Darcy's Law converted to a mass flow rate is

$$\dot{m}_D = \frac{K_{D,o} A \Delta P \rho}{\mu(\delta_o - \delta' \Delta P)} \quad (5.22)$$

When implementing the DGM, membrane thickness is required, but the pore size, membrane porosity and tortuosity are also required. The non-compacted porosity ϵ_o was measured in this study. The porosity is a simple calculation based on membrane surface area and mass as

$$\epsilon_o = \frac{V_{void}}{V_o} = 1 - \frac{V_{PTFE}}{V_o} \quad (5.23)$$

where $V_{PTFE} = \frac{m_{PTFE}}{\rho_{PTFE}}$ and the non-compacted volume of the membrane including the void and the pore structure is

$$V_o = \delta_o L W \quad (5.24)$$

The length L and width W of the membrane sample were determined directly with a linear scale. The sample was cut with a shear-type paper cutter which has a paper stop to help produce right angle corners - the sample size was 2.5 cm \times 2.5 cm. The thickness was determined with a 2.5 μm precision micrometer by first measuring the active PTFE layer and the PP scrim backing together. The thickness of these two layers was found to be 120 μm on average. To determine the thickness of the PTFE, an X-ACTO[®] knife was used to separate the two layers and the PP thickness was measured with the micrometer. Knowing the PP thickness, the PTFE layer was

found to be $15.6 \mu m$. The membrane's porosity is limited by the volume of the PTFE layer previously peeled off of the PP. To find this volume, the mass is determined with a digital mass balance having a resolution of 0.0001 g and converted to a volume assuming the density of PTFE, ρ_{PTFE} , is 2.2 g/cm^3 . The resulting porosity of the $0.45 \mu m$ mean pore diameter PTFE layer was found to be 45% PTFE by volume therefore $\epsilon = 0.55$.

The tortuosity is commonly approximated as the inverse of the porosity because it is not easily measured in thin membranes like the one here; its value is $\tau = 1/\epsilon = 1.82$. Although the diameter of the pores in the membrane vary in a narrow Gaussian-type distribution as found by Martinez et al. [16], the mean pore diameter found by Martinez et al. [16] was used for simplicity. They determined the mean pore diameter from the measured distribution, its value is $\bar{r}_p = 0.236 \mu m$.

The variable thickness can be used to approximate the variable porosity and tortuosity by assuming the volume of PTFE making up the nanofibers remains constant through compaction

$$V_{PTFE} = \text{constant} = (1 - \epsilon_o) V_o \quad (5.25)$$

Another assumption used is that the $L \times W$ area of the membrane remains constant. In reality, when a pressure is applied across the membrane the PTFE layer depresses into the ovals of the scrim backing (Fig. 4.1) and therefore the area does change slightly. The remaining variables in the DGM are fluid properties and experimental values.

Substituting Eqs. (5.24) and (5.25) into the porosity equation yields

$$\epsilon = 1 - \frac{V_{PTFE}}{V} \quad (5.26)$$

and allows the area to cancel resulting in the variable porosity being a function of thickness

$$\epsilon = 1 - \frac{\delta_o(1-\epsilon_o)}{\delta} \quad (5.27)$$

Since tortuosity is approximated as the inverse of the porosity, Eqs. (5.20) and (5.26) are sufficient to describe the membrane characteristics as a function of membrane thickness. When substituting the variables which depend on the membrane thickness into the DGM introduced as Eq. (2.19), the rearranged equation is

$$\dot{m}_i = \frac{\Delta P M_i A \left(1 - \frac{\delta_o(1-\epsilon_o)}{\delta}\right)^2}{RT\delta} \left[\frac{2\bar{r}_p}{3} \left(\frac{8RT}{\pi M_i}\right)^{1/2} + \frac{\bar{r}_p^2}{8\mu_{v,i}} \bar{P} \right] \quad (5.28)$$

This expression predicts the mass flow rate for transition flow with compaction where δ depends on the pressure difference and is defined by Eq. (5.20). Comparing the relationship the varying thickness has on the mass flow rate in Darcy's Law of Eq. (5.22) and the DGM of Eq. (5.28), it is evident that the compaction coefficient δ' will likely be different for each model.

5.6 Existing Model Modifications for Two-phase Gas Extraction

When applying theoretical models to the two-phase data, the empirical coefficient δ' was implemented to account for compaction. The only variable that changes in addition to those from the single-phase vapor study is the flow area. This is because

physics captured in Darcy's Law and the DGM are limited to the control volume of the membrane, and the area is the only variable of the existing models which can relate to the hydrodynamics at or near the membrane interface. The extraction area was scaled by an area correction parameter Φ_m to approximate the time-averaged gas-membrane contact area. This scaling parameter accounts for the pores which do not contribute to the overall gas extraction as a result of being blocked by liquid. The area terms in Darcy's Law Eq. (2.7) and the DGM Eq. (2.19) are replaced by an effective extraction area, A_{eff} , as

$$A_{eff} = A_{mem} \Phi_m \quad (5.29)$$

This effective extraction area can be approximated by the void fraction in the inlet plenum when assumptions are made about the gas behavior. The effective extraction area can be approximated empirically to better fit the experimental extraction data.

5.6.1 Theoretical Effective Extraction Area

To approximate the effective extraction flow area, the void fraction α is multiplied by the area of the membrane available for flow. This is an approximation which assumes bubbles are spherical and move at a constant velocity. The average cross-sectional area of gas in contact with the membrane was calculated for a bubble traveling through a unit cell as described in appendix C. If there were no bubble dynamics and instead there were vapor columns in the liquid, this approximation would accurately represent the effective extraction area. In reality, hydrodynamics further

limit the effective extraction area.

The void fraction

$$\alpha = \frac{V_g}{V_g + V_l} \quad (5.30)$$

quantifies the volume of gas compared to the total volume of the liquid and gas. The Drift-Flux model from [42] predicts the void fraction by considering the average void fraction of a planar area perpendicular to the flow (parallel with the membrane here). This model is designed for bubbly flow where the bubbles are isolated, typical for low available gas flow rate cases. However, when the Drift-Flux model is applied to these data, the void fractions are unreasonably low. This is likely a result of various bubble sizes and flow that has not developed to allow the bubbles to reach their terminal velocity.

A more reasonable approximation for void fraction is determined with the Armand coefficient, C_A :

$$\alpha \approx \beta C_A \quad (5.31)$$

specifically for annular flow C_{AA} as shown by Chisholm [43] and reproduced as

$$\frac{1}{C_{AA}} = 1 + \frac{23}{u_H} \left[\frac{\mu_l u_{l,s}}{\rho_g D} \right]^{1/2} \left[1 - \frac{\rho_g}{\rho_l} \right] \quad (5.32)$$

where $u_{l,s}$ is the superficial liquid velocity, Q_l/A_{mem} and u_H is the homogeneous velocity $(Q_l+Q_g)/A_{mem}$. This model is recommended when the volumetric flow ratio, β , is greater than 0.9. The Armand coefficient is multiplied by the volumetric flow ratio

$$\beta = \frac{Q_g}{Q_g + Q_l} \quad (5.33)$$

The volumetric flow ratio is shown only to be accurate for either high mass flux or high pressure, therefore correlations are developed to scale it for specific flow regimes.

Once the void fraction is determined, it is multiplied by the area in Eq. (5.28) which decreases the slope of the mass flow rate vs. pressure difference curve. When the DGM prediction is equal to the available gas mass flow rate, the DGM was no longer used to predict extraction because the gas extraction rate is limited to that which is available. In other words, once the available gas is fully extracted, the predicted gas extraction reaches a plateau.

5.6.2 Empirical Effective Extraction Area

The extraction area correction term, Φ_m , was determined from the experimental extraction data so the compaction-corrected models predict gas extraction accurately. The area correction term is implemented to scale the extraction predictions to more accurately describe extraction rates. After the compaction corrections are included in Darcy's Law and the DGM, the extraction area is the only other variable which limits gas extraction. The area is scaled by the ratio of the measured and predicted mass flow rates with an area correction term

$$\Phi_m = \frac{\dot{m}_{ext,meas}}{\dot{m}_{ext,pred}} \quad (5.34)$$

where the predictions include the effects of compaction.

The experimental data will result in an area correction term which varies for each data point, therefore some type of fit must be applied. This can be done in one of two ways. The first method results in a constant area correction value for a each set of data and its corresponding void fraction. This is accomplished by plotting the experimental data against the predicted data and fitting a line through the origin. The slope of the best fit line is equal to the area correction term. The second method is not a curve fit, but instead a set of individual data points which are a function of pressure. These individual data points influence an exponential curve fit as will be seen in sections 6.3.2 and 6.3.3.

5.7 Image Analysis

To analyze hydrodynamics and explain discrepancies between data sets, high speed videos were taken at 4000-8000 fps which provided about 1 s of data for each steady state point. The videos were post-processed as multipage tagged image file format (TIFF) files. Other than visual observation, the only measurements made for all data cases was the bubble diameter. For low available gas flow rate experiments where uninterrupted bubble-membrane interaction is possible, extraction behavior was also studied. When studying the extraction behavior, bubble velocities were calculated as well as the time to extract individual bubbles.

Before measuring the bubble sizes or velocities, the videos were calibrated so the pixels could be converted to a practical measure of length (meters). To calibrate the

videos, the membrane ribs with a known spacing were measured using a pixel ruler and protractor with the software package PicPick [44]. The only known other than the rib spacing was the camera angle as measured with a plumb weight hanging from a yardstick parallel to the camera's line of sight. Using trigonometry relations to convert the apparent horizontal distance of the membrane's angled grid lines, the pixel-to-mm conversion was determined as described in appendix F.3. These trigonometry relations would be unnecessary if the ribs of the membrane were along the line of sight with the camera, but this depends on the orientation of the membrane which could not be set easily.

With the conversion factor known, the pixel ruler was used to manually measure the bubble *width* which was approximated as the diameter. If measurements of the height were made, the measurements were scaled by the inverse of the cosine of the camera angle. At least 20 bubble diameters were measured for each experiment. When determining the uncertainty of the means, a 95% confidence interval was used.

To determine bubble velocities, Open Source Physics' Tracker software was used [45] and bubbles were manually tracked. Bubble extraction times were based on the frame count and are manually parsed with IrfanView [46]. When select frames were pulled and cropped from the multipage TIFFs, MATLAB[®] was used. To scale these frames, IrfanView was used.

Chapter 6 – Results and discussion

This chapter contains results and discussion of the experiments and model development for membrane transport in two-phase gas extraction. Data are presented starting with single-phase flows to validate existing theoretical models predicting transport behavior through porous media, specifically microporous membranes. The models validated are the dusty gas model (DGM) and Darcy’s Law. Both models are used to predict membrane compaction. The symbols in the figures of sections 6.1 and 6.2 are consistent with the descriptions given in Table 6.1. The single phase tests used the mean properties because there was gas on both sides of the membrane so the thermal conductivity was similar. Fluid properties for two-phase tests are evaluated

Table 6.1: List of symbols and their corresponding data cases used in figures

Fluid	Symbol	Nominal Available Gas	
		$\dot{m}_{avail.}$ (gpm)	$Q_{avail.}$ (mL/min)
Single-phase air	+		
Single-phase super heated vapor	x		
Liquid-vapor	*	0.26	436
	Δ	0.72	1208
	\diamond	0.98	1644
	\square	1.38	2315
	\circ	1.55	2601
Liquid-air	\blacktriangle	0.13	99
	\blacklozenge	0.26	195
	\blacksquare	1.63	1208
	\bullet	2.37	1733

at the average pressure and temperature of the inlet and extraction chamber.

6.1 Existing Model Validation for Single-Phase Flow

The ultimate purpose of the single phase tests is to determine the effects of membrane compaction due to an applied pressure difference across the membrane. The data presented in this section show recorded data starting from an applied high pressure differential (≈ 30 kPa) which incrementally decreases to no applied pressure difference across the membrane. As mentioned in the previous section, volume flow rate, Q , is measured with a rotameter for air and with the catch-and-weigh method for vapor. The presented data points are each mean values averaged over at least one minute of time samples.

The single-phase data consists of one experiment for room temperature air and one experiment for superheated water vapor. For reference, all data conditions are in Table 4.2. The reason for super heating the vapor is that if it were saturated, droplets may form on the membrane and reduce the extraction area. Furthermore, condensation is a phenomenon that could potentially limit gas transport through the membrane, so keeping the vapor near the saturation temperature was avoided.

6.1.1 Darcy's Law

The first model considered for the single phase extraction curves is Darcy's Law where the permeability is calculated with Eq. (2.7) at each steady state data point

knowing the following:

1. The volume flow rate for a given pressure difference across the membrane
2. The superficial flow area, A
3. The non-compacted membrane thickness, δ_o (measured at atmospheric pressure)
4. The gas dynamic viscosity, μ

Air's dynamic viscosity is found with the Sutherland equation, Eq. (5.19), which only depends on temperature. Both (a) and (b) of Fig. 6.1 show empirical variables K_D and R_D of Darcy's Law, respectively, but the resistance (b) does not include the the non-compacted membrane thickness.

It is evident from these figures that there is a trend for increasing permeability

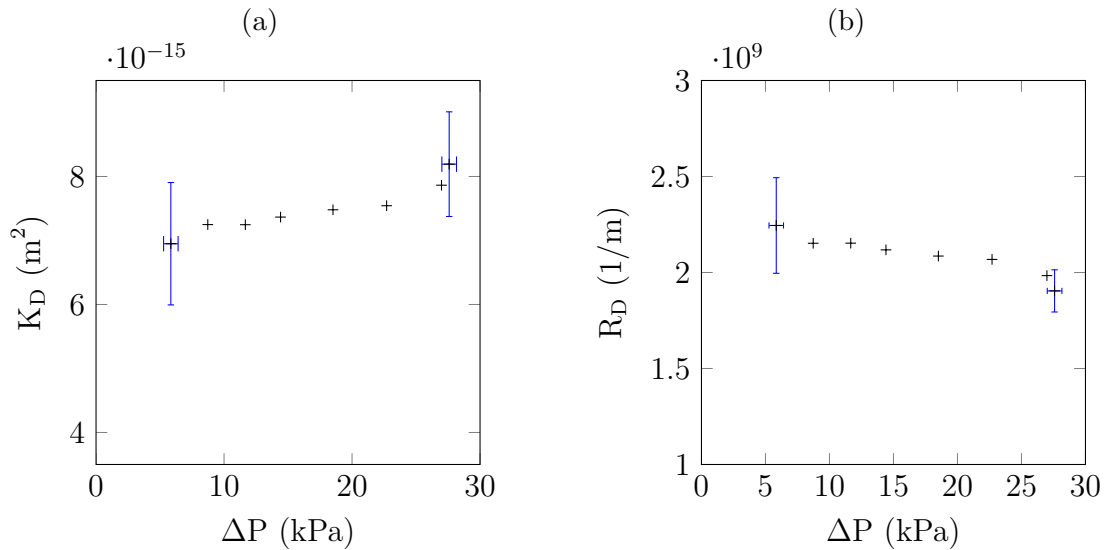


Figure 6.1: Single-phase empirical Darcy values for air: (a) Darcy permeability $\bar{K}_D = 7.5 \times 10^{-15} m^2$ and (b) Darcy resistance $\bar{R}_D = 2.1 \times 10^9 1/m$.

as the flow rate increases which has been found to be expected behavior for porous membranes. Lawson et al. [30] found that for membranes with porosities greater than about 65% the permeability increases with an increase in pressure, then decreases when a certain thickness is reached. Considering the porosity of the membrane studied here is 55%, it is possible the trend is accurate. However, noting the span of the error bars, it is also possible the rotameter used was inaccurate due to the large range of flow rates it covers.

The permeability and resistances of superheated vapor are presented in Fig. 6.2. The flow rate is measured by catch-and-weigh for this fluid which is more accurate over a wider range compared to rotameters. The same trend of increasing permeability with pressure difference is apparent in the superheated vapor study. This reinforces

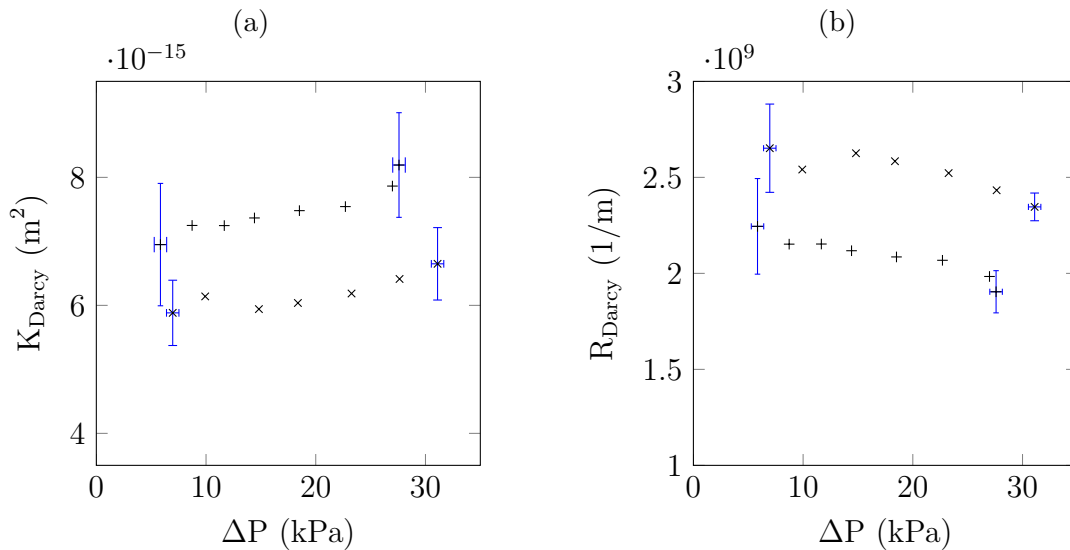


Figure 6.2: Single-phase superheated vapor Darcy values (“x” markers) superimposed with single-phase air (“+” markers): (a) Darcy permeability $\bar{K}_D = 6.2 \times 10^{-15} \text{ m}^2$ and (b) Darcy resistance $\bar{R}_D = 2.5 \times 10^9 \text{ 1/m}$.

Table 6.2: Summary of single-phase mean Darcy values based on Eq. (2.9)

Fluid	Mean Darcy Resistance ($1/m$)	Mean Darcy Permeability (m^2)
Air	2.09×10^9	7.49×10^{-15}
Vapor	2.53×10^9	6.18×10^{-15}

the increasing permeability trend found with the air data.

As described using Eq. (2.9), Darcy's Law can predict the mass flow rate with a constant permeability and membrane thickness in its traditional form. The mean single-phase Darcy values from Figs. 6.1 and 6.2 are summarized in Table 6.2.

When Darcy's Law with a constant permeability equal to the mean value from the single-phase air data Fig. 6.1a is implemented, the extracted mass versus pressure difference relationship seen in Fig. 6.3 is produced.

This curve shows a deviation from the data because the permeability is held con-

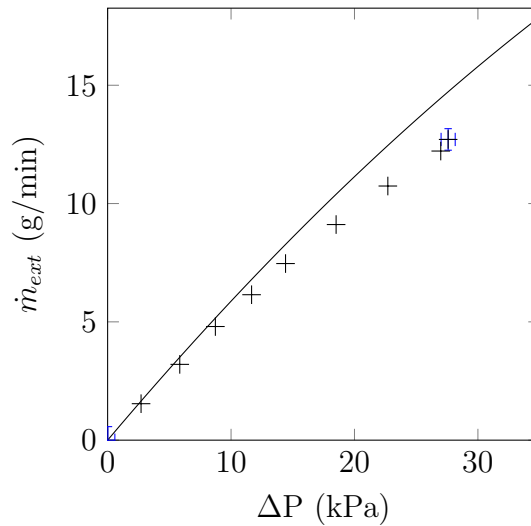


Figure 6.3: Single-phase air flow rate measured data (“+” markers) and predictions using Darcy's Law Eq. (2.9) with constant permeability and membrane thickness (solid line).

stant as the pressure difference increases. This indicates a limitation of the mass flow rate as the pressure difference increases. This decreased mass flow rate is attributed solely to compaction. To account for membrane compaction, the membrane thickness can be described as a function of pressure as captured by Eq. (5.22). The change in permeability can be accounted for with an empirical coefficient relating membrane thickness to the pressure difference. The varying membrane thickness is assumed to have a linear relationship with pressure as seen in Eq. (5.20). To implement this varying thickness, the permeability must be held constant at a value with a known thickness as presented in Eq. (5.22). The constant, initial permeability, $K_{D,o}$, is equal to the extrapolated permeability when there is no compaction. The initial per-

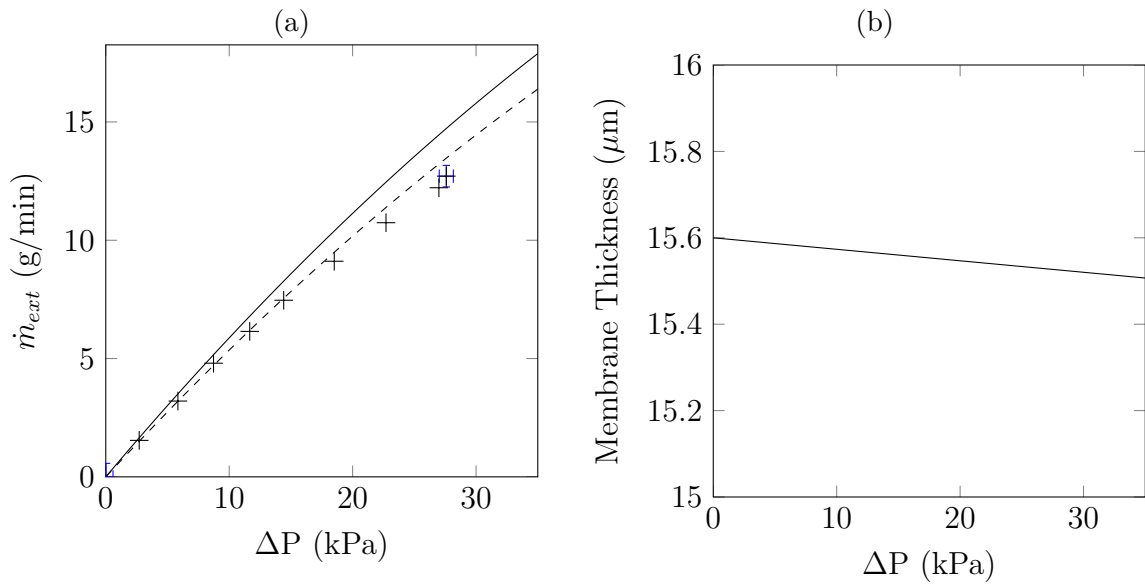


Figure 6.4: (a) Single-phase air flow rate predictions using Darcy's Law with constant permeability and membrane thickness (solid line) and accounting for compaction (dashed line) with $\delta'_{D,air} = 2.7 \times 10^{-9}$ m/kPa; (b) resultant reduction in thickness with increasing pressure difference.

meability is determined by fitting a line to the permeability curves in Fig. 6.2a. To determine the value relating pressure difference to membrane thickness, a compaction coefficient δ' is fit to the measured extraction data as a function of the pressure difference by searching for the least mean absolute error. The Darcy compaction coefficient for air was found to be 2.7×10^{-9} m/kPa and results are shown in Fig. 6.4.

Similarly, the Darcy compaction coefficient for vapor is determined to be $\delta'_{D,vap} = 2.25 \times 10^{-8}$ m/kPa. The comparison between using a mean permeability and a constant permeability with compaction are shown in Fig. 6.5.

The quality of fit for the single-phase compaction corrections is quantified in Table 6.3 which includes the mean absolute error (MAE) as described in appendix D.

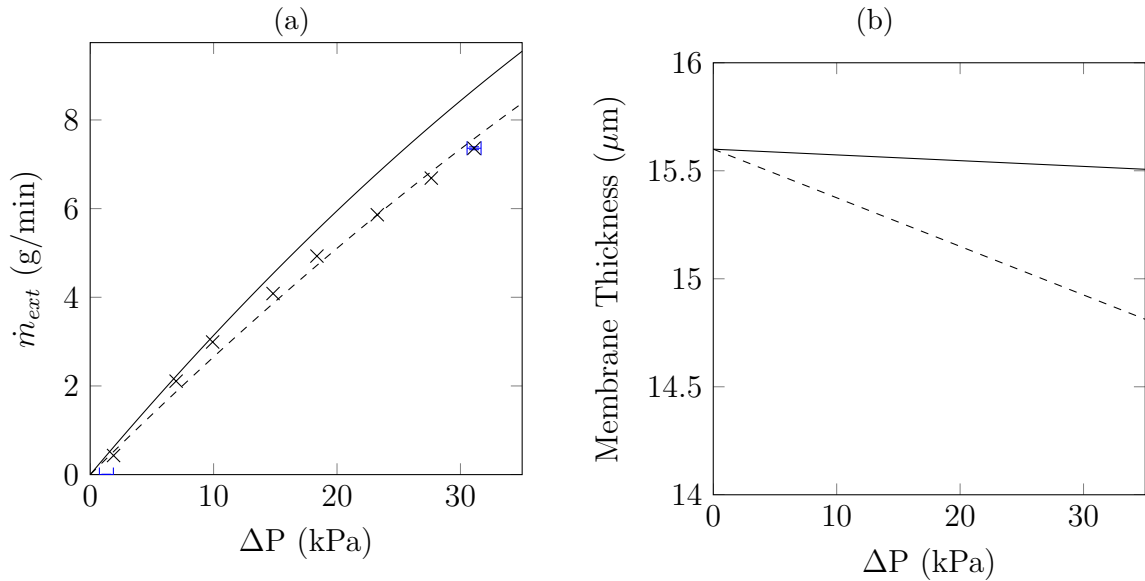


Figure 6.5: Single-phase superheated vapor predictions using Darcy's Law Eq. (2.9) (a) mass flow rate with constant permeability and membrane thickness (solid line) and accounting for compaction (dashed line) with $\delta'_{D,vap} = 2.25 \times 10^{-8}$ m/kPa and (b) membrane thickness (dashed line) and that for air (solid line)

When accounting for compaction, the MAE of Darcy's Law is reduced by 72% and 54% for air and superheated vapor, respectively.

Table 6.3: Summary of single-phase Darcy values assuming a mean permeability and accounting for compaction

Fluid	Darcy's Law					
	With Compaction			No Compaction		
	δ' (m/kPa)	K_o (m ²)	MAE (%)	$\delta = \delta_o$ (μm)	$\bar{K}_{D,g}$ (m ²)	MAE (%)
Air	2.66E-09	6.8E-15	3	15.6	7.49E-15	12
Vapor	2.25E-08	4.9E-15	7	15.6	6.18E-15	16

6.1.2 Dusty Gas Model

The second model employed is the dusty gas model which predicts theoretical mass flux using membrane properties. It was introduced in Eq. (2.19) where δ is defined by Eq. (5.20) and membrane properties are listed in Table 4.1. When the membrane thickness is held constant, a linear curve is produced when comparing the mass flow rate to the applied pressure difference. Similar to the predictions from Darcy's Law, the measured data deviates from this prediction so an empirical compaction coefficient is fit to account for the membrane's decreasing thickness using the same relationship which was used in the compaction-corrected Darcy's Law.

Both forms of the DGM predict air flow rate well and the relation between the raw data and the solid line in Fig. 6.6 resemble the curve for a 70% porous membrane being compacted from Lawson et al. theoretical study [30].

The DGM predictions for superheated vapor mass flow rates over-predict the mea-

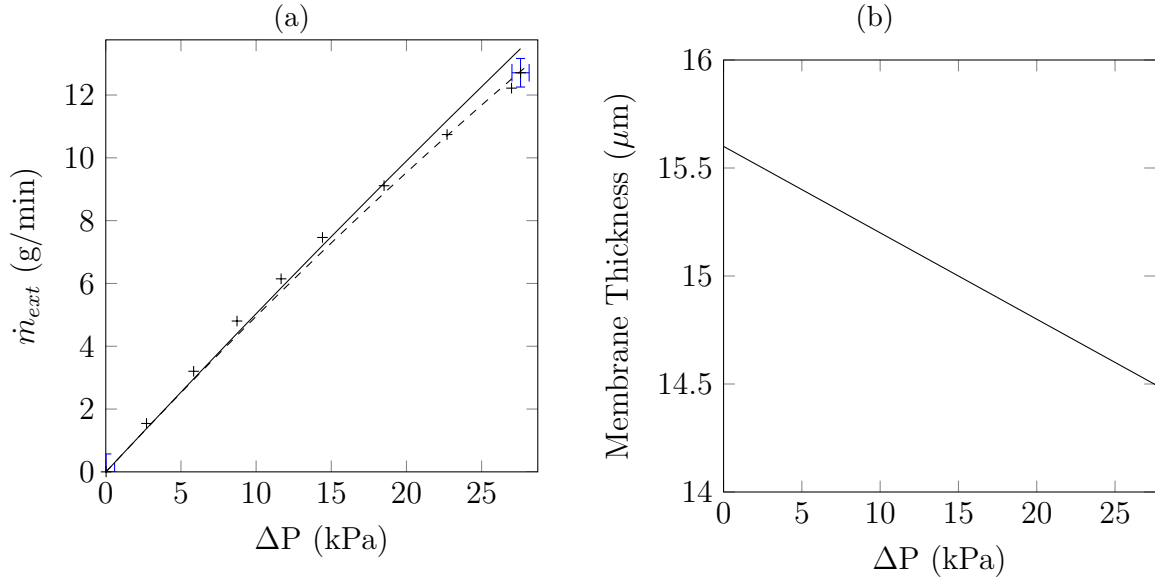


Figure 6.6: (a) Measured single-phase air data (“+” markers) compared to predictions using the dusty gas model not accounting for compaction (solid line) Eq. (2.19) and accounting for compaction (dashed line) where $\delta'_{air} = 4.0 \times 10^{-8}$ m/kPa and (b) resulting membrane thickness versus pressure differential.

sured data as seen in Fig. 6.7. The same membrane properties and DGM flow regimes are used to calculate the vapor curve in Fig. 6.7a, therefore the difference in deviation from the constant-thickness DGM is attributed to the higher temperature resulting in a softer membrane as noted by Lawson et al. [30]. The data are well fit using a new membrane compaction coefficient δ'_{vap} . It should also be noted that the pressure data is corrected with *saturated* steam flowing through the porous stainless steel support which could cause some inaccuracy, see section 5.3. The summary of the single-phase DGM values is presented in Table 6.4. With the knowledge of compaction effects, the modified DGM equations accounting for membrane thickness can be applied to two-phase extraction curves to eliminate the changes due to compaction. It

is important to note that compaction does not result in any cycling effects because the pressure difference applied to the membrane here did not result in plastic (i.e. permanent) deformation, but greater pressures could possibly damage the membrane. The bonds of PTFE are only strong in the sense that they resist chemical reactions from common solutes and fluids but are not mechanically robust. The compaction coefficients are implemented in two-phase flow rate predictions starting with liquid-air in section 6.2.

The compaction coefficients in Table 6.4 are most closely, but not directly, comparable to the studies of Lawson et al. [30] who used a different membrane material. Two of their polypropylene membranes had similar pore sizes (0.4 and $0.51\mu\text{m}$) but

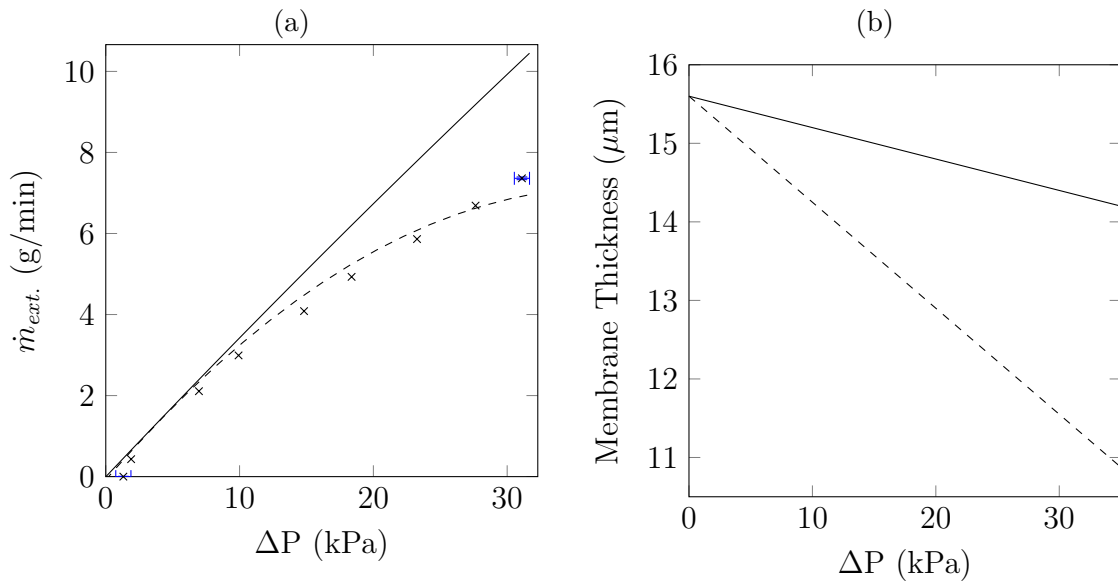


Figure 6.7: Single-phase superheated vapor flow rate predictions using the dusty gas model (a) not accounting for compaction (solid line) Eq. (2.19) and accounting for compaction (dashed line) with $\delta'_{vap} = 1.35 \times 10^{-7}$ m/kPa and (b) membrane thickness (dashed line) and that for air (solid line).

Table 6.4: Summary of single-phase results using the dusty gas model, Eq. (2.19), accounting for membrane compaction and holding thickness constant.

Fluid	Dusty Gas Model			
	With Compaction		No Compaction	
	δ' (m/kPa)	MAE (%)	$\delta = \delta_o$ (μm)	MAE (%)
Air	4.00E-08	5	15.6	6
Vapor	1.35E-07	12	15.6	30

higher porosities (76% and 79%) compared with the PTFE membrane studied here. Their working fluids were nitrogen and hydrogen at 25° and they found compaction coefficients of 8.9×10^{-8} m/kPa and 2.7×10^{-7} m/kPa for their 0.4 μm and 0.51 μm pore diameters respectively. They claim “ δ' is directly related to the temperature dependent mechanical properties of the membrane material.” When comparing the PTFE compaction coefficient at the same temperature it is evident that the PTFE membrane compacts less than comparable PP membranes. This is likely due to the fact that the porosity of the PTFE membrane is lower than the PP membranes. Assuming the compaction coefficient is directly related to the temperature as Lawson et al. [30] predict, a relationship can be developed to estimate the compaction coefficient. A linear fit capturing the two data points available for the 0.45 μm PTFE membrane studied here at 115°C and 25°C result in

$$\delta' = \left(1.1 \times 10^{-9} \frac{1}{K} T - 2.7 \times 10^{-7} \right) \text{ m/kPa} \quad (6.1)$$

where T is the average temperature of the gas in the membrane. It should be noted that this relationship was not verified to be fluid independent by changing the tem-

perature of the air or vapor.

As mentioned above, the thicknesses predicted by Darcy's Law and the DGM vary at different rates with pressure. Both Darcy's Law and the DGM predict greater compaction for vapor compared to air. As seen in Fig. 6.8, Darcy's Law predicts less overall compaction because the porosity term is not included, therefore the thickness predictions from the DGM are more accurate because it is describing the physics of the flow in more detail.

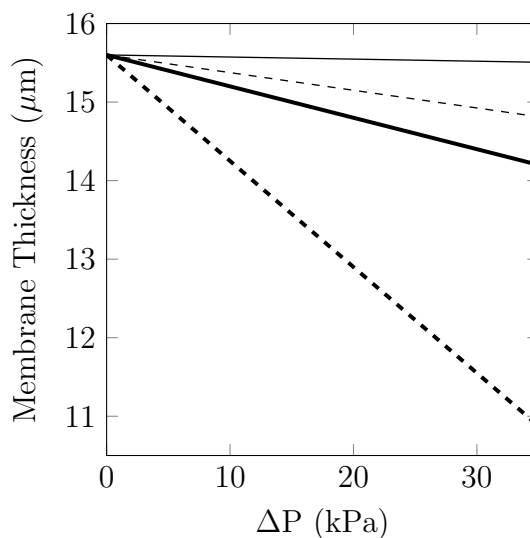


Figure 6.8: Predicted membrane thickness based on Darcy's Law (thin lines) and the DGM (thick lines) for superheated vapor (dashed line) and air (solid line); curves are defined by Eq. (5.20).

6.2 Modified Models for Two-phase Gas Extraction

In this section, the same models which were applied to the single-phase data are applied to the two-phase data. Permeability is first calculated holding the thickness

constant to keep Darcy's Law in its traditional form and to ultimately produce a model where the two-phase permeability captures the effects of compaction and effective area. Furthermore, the compaction results of Darcy's Law and the DGM are applied in addition to the effective flow area being scaled to account for the liquid blocking membrane pores as was described in section 5.6.2. This time-averaged extraction area is *estimated* assuming bubbles do not deform or stagnate at the membrane interface, but instead seamlessly rise through the liquid and flow into the membrane.

The results in sections 6.2.1 and 6.2.2 are evaluated at the average pressure and temperature of the gas as it passes through the membrane. For the liquid-air mixture, only the values of humid air are considered because if an application called for gas separation, the multi-species flow conditions would be desired to accurately predict extraction flow rates. The liquid-air flow loop was designed to reduce the likelihood of condensation-related issues by employing reasonably dry air to produce bubbles. Using relative humidity sensors before and after extraction were used to quantify the amount of vapor added to the air flowing through the system. As seen in the summary of test conditions Table 4.2, the inlet humidity is below 20%. When the gas is measured after it is extracted, especially at high pressure differences, it contains more water vapor. This addition of vapor is due to one of the three conditions:

1. Diffusion from the liquid to the bubbles as they pass through the inlet plenum
2. Evaporation at the liquid-membrane interface
3. Liquid droplets from rupturing film get stuck in the membrane and evaporate

These phenomenon exist in liquid-vapor studies as well, but predicting their contribution is not possible in this setup because the uncertainty in the generated vapor

is high, so the amount of vapor extracted in addition to that which is generated can not be determined.

In the area-corrected Darcy's Law and DGM predictions, the area is reduced by the Armand-corrected void fraction (Table 6.5) resulting in a decreased slope of the predicted mass flow rate.

Table 6.5: Armand-corrected void fraction for all two-phase experiments, calculated with Eq. (5.32).

Phases	Nominal Available Flow Rate		Void Fraction (%)	
	$\dot{m}_{avail.}$ (gpm)	$Q_{avail.}$ (mL/min)	β	α_{AA}
Liquid-Vapor	0.26	436	97.8	20.5
Liquid-Vapor	0.72	1208	99.2	41.5
Liquid-Vapor	0.98	1644	99.4	48.5
Liquid-Vapor	1.38	2315	99.9	68.1
Liquid-Vapor	1.55	2601	99.7	61.7
Liquid-Air	0.13	99	90.7	4.5
Liquid-Air	0.26	195	95.2	8.8
Liquid-Air	1.63	1208	99.2	36.5
Liquid-Air	2.37	1733	99.4	48.2

6.2.1 Darcy's Law

Presented in Fig. 6.9 is the Darcy permeability of both liquid-vapor and liquid-air for comparison. The resistance is shown in Fig. 6.10 as an alternative to the permeability.

The two-phase permeability plots, Fig. 6.9a and Fig. 6.9b, show on a log scale that both mixtures follow the same trend of decreasing permeability as the pressure difference is increased. This trend is not linear but appears so because the data is

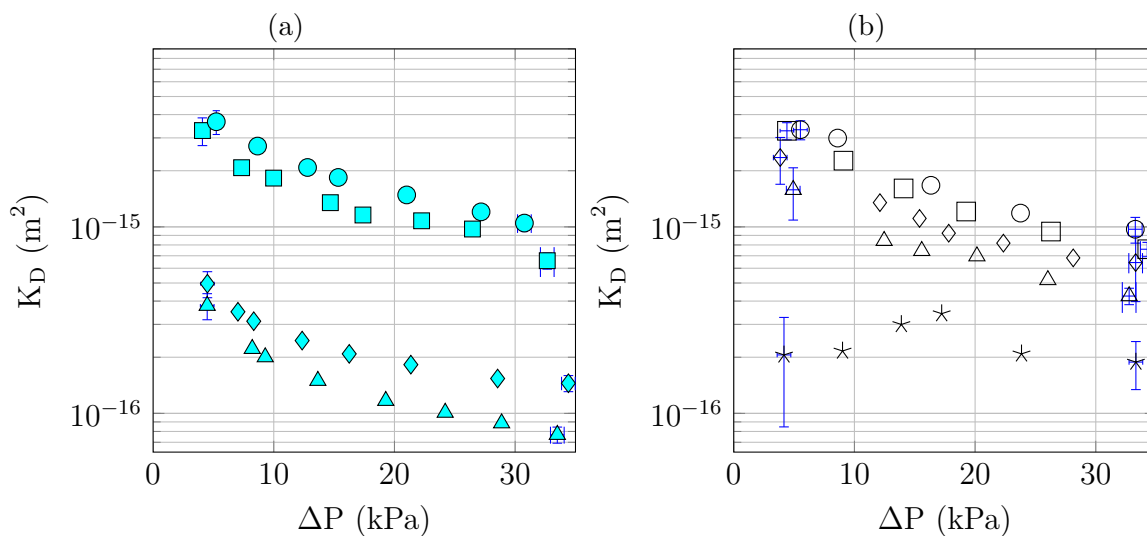


Figure 6.9: Two-phase Darcy permeabilities: (a) Liquid-air and (b) Liquid-vapor; symbols correspond to Table 6.1 on pg. 90.

presented in a log domain. This trend is due to hydrodynamic phenomena in the exo-membrane region. The hydrodynamics of the bubbles and liquid film at the membrane surface are influencing the extraction behavior significantly. This is evident because at the lowest pressure differential where full extraction is achieved (≈ 10 kPa for greater available gas cases), the permeability is less than that of the single-phase gases. The one case which is inconsistent with the trends of the other data points is that of the lowest available gas flow rate of liquid-vapor. Since there is an identical available gas flow for the liquid-air case which shares a consistent trend with the other data, the inconsistency with the liquid-vapor case is attributed to one of two things:

1. High uncertainty in the measured extraction flow rates as seen in Fig. 6.32a
2. A different flow regime comprised of many small bubbles and only some bubbles on par with other cases as is shown later in Fig. 6.15a

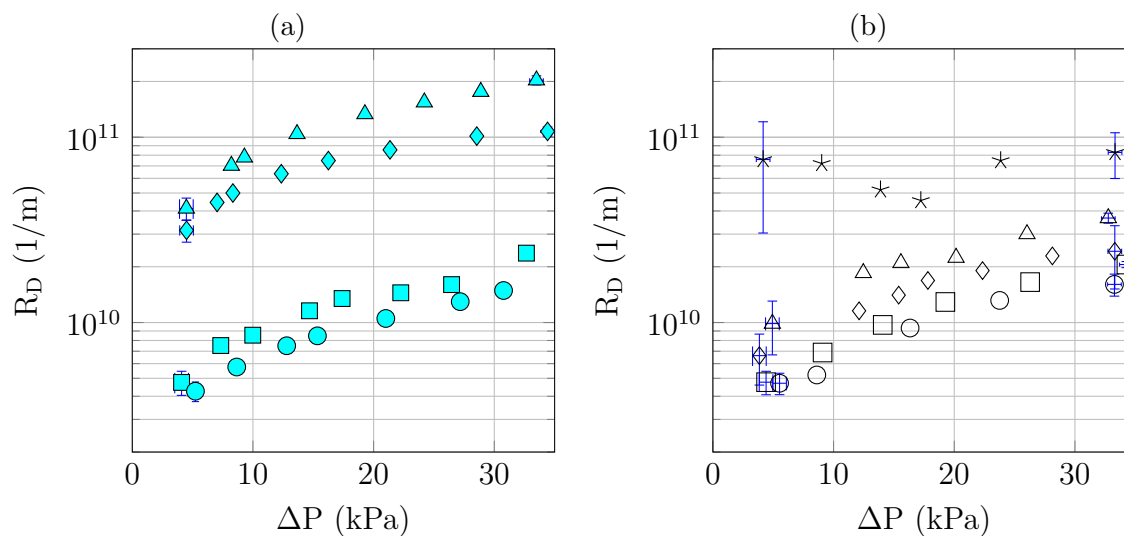


Figure 6.10: Two-phase Darcy resistances: (a) Liquid-air and (b) Liquid-vapor; symbols correspond to Table 6.1 on pg. 90.

It should be noted that these permeability calculations use the same superficial flow areas which were used in the single-phase calculations.

To correct the extraction area for more accurate two-phase predictions with Darcy's Law, the void fraction is used as is described in section 5.6.1. Other than coupling Darcy's Law with additional models to predict film rupture and bubble dynamics, this area correction will provide the best prediction for extraction rates rather than generating a purely empirical model. By scaling the membrane area by the void fraction in the inlet plenum, the time-averaged extraction area results as described in appendix C. The measured and predicted two-phase extraction rates are shown in Figs. 6.11 and 6.12 where the sloped line is the compaction- and area-corrected Darcy's Law. The mass flow rate predictions appear linear because the pressure differences are low and the effects of compaction are not significant. The plateau is

defined by the amount of available gas in the inlet plenum. When a high enough pressure difference is reached to drive the same amount gas through the reduced extraction area as the amount of gas available, the extraction rate reaches a limit. At this limit of full extraction, higher pressure differences will realistically result in slightly higher extraction rates due to evaporation from the liquid blocking the pores, but this increase is assumed to be negligible.

Darcy's Law predicts extraction reasonably well for all available flow rates at pressure differences below ≈ 5 kPa except for the 0.26 g/min case. The reasons this flow rate is not well predicted are consistent with the explanations for the out-of-trend permeability for this case as described at the beginning of this section.

The uncertainties in measured extraction rates vary between cases because data were either taken for different amounts of time or slugs of liquid being weighed resulted in a choppy mass vs. time curve. The uncertainty of the plateau is based on an energy balance predicting the amount of gas generated. This uncertainty remains nearly constant for all cases because the uncertainty of the heat flux and the liquid mass flow rate do not change significantly from case to case.

The liquid-air predictions presented in Fig. 6.12 are also limited by the available gas, but it is measured with a rotameter or flow rate transducer so the uncertainties are lower. The 2.38 g/min case of available air has a higher uncertainty than the other liquid-air cases because a rotameter with a greater range (and uncertainty) was used. The two higher mass flow rate cases have higher uncertainties because instantaneous extraction rates were sporadic and resulted in a high standard deviation.

The liquid-air predictions presented in Fig. 6.12 are limited by the available gas

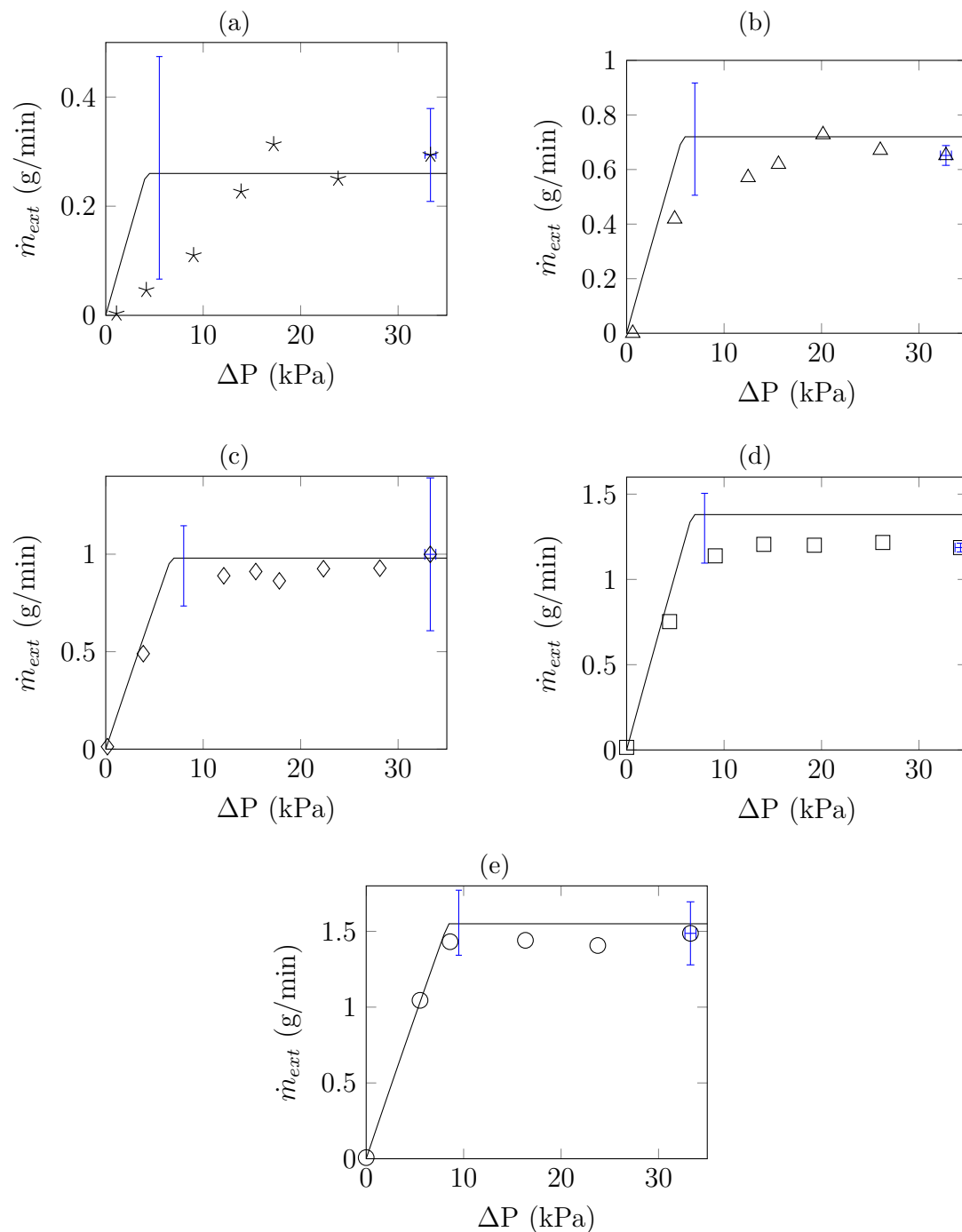


Figure 6.11: Liquid-vapor flow rate predictions from Darcy's Law accounting for compaction with Eq. (5.20) where $\delta' = \delta'_{D,vap}$ and flow area is scaled by the annular Armand-corrected void fraction; symbols correspond to Table 6.1 on pg. 90.

like the liquid-vapor predictions, but for this mixture the gas is not fully extracted. This incomplete extraction is attributed to the hydrodynamics in the inlet plenum being different than the liquid-vapor hydrodynamics.

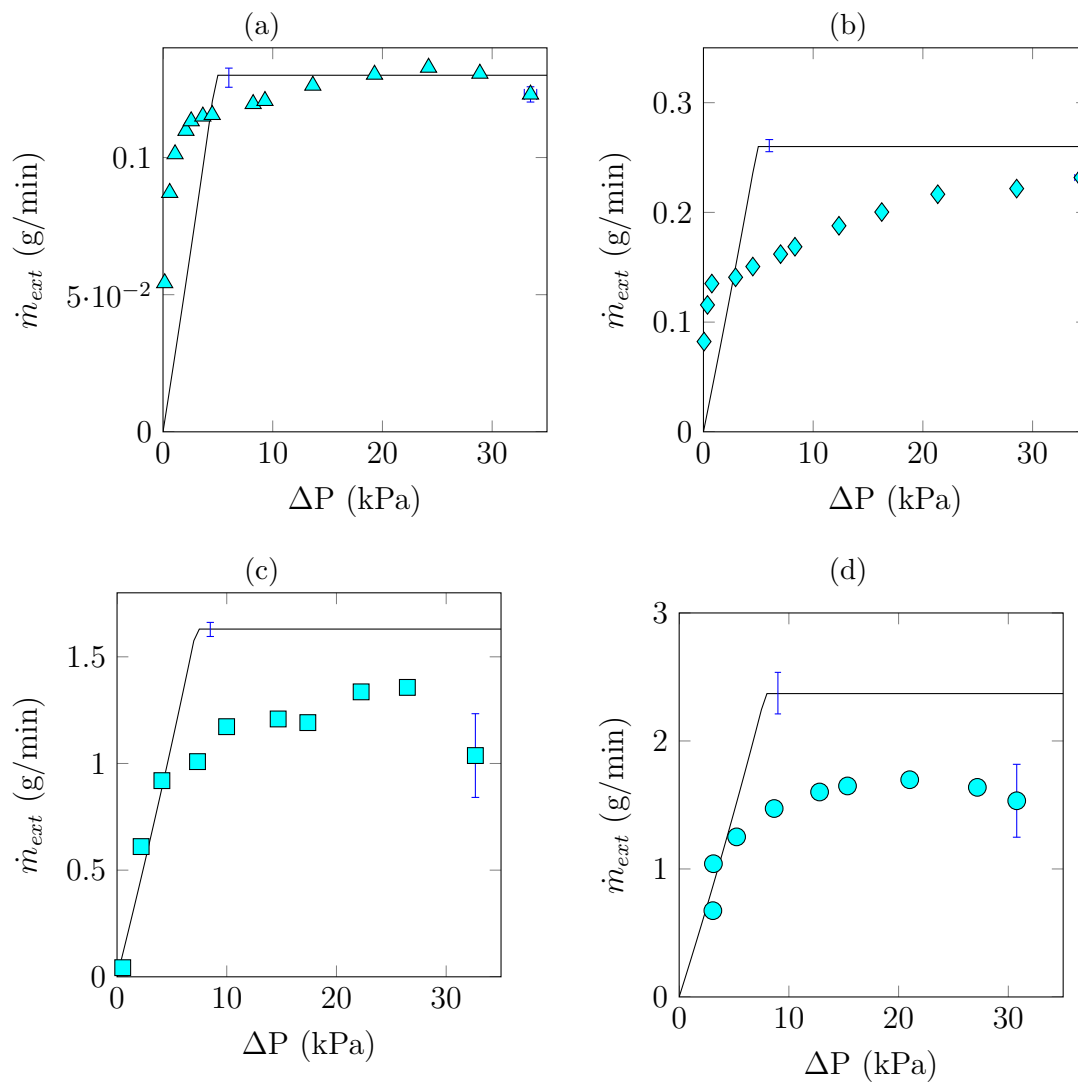


Figure 6.12: Liquid-air flow rate predictions from Darcy's Law accounting for compaction with Eq. (5.20) where $\delta' = \delta'_{D,air}$ and the flow area is scaled by the annular Armand-corrected void fraction α_{AA} listed in Table 6.5; symbols correspond to Table 6.1 on pg. 90.

6.2.2 Dusty Gas Model

The DGM accounting for membrane compaction, Eq. (2.19) with Eq. (5.20), is used to predict extraction rates where the area is scaled by the void fraction in the inlet plenum. The resulting extraction predictions are compared to the measured extraction rates in Figs. 6.13 and 6.14 for liquid-air and liquid-vapor, respectively. Fig. 6.14 shows complete extraction for the lowest available air flow rate case. When the air flow rate is low, there are fewer bubble-bubble interactions and the area of the membrane is not as populated by other bubbles so it is more likely that all the air can be extracted. This is discussed further in section 6.3.1.1.

The liquid-vapor extraction curves reach a plateau equivalent to the amount of vapor available indicating full extraction. This is discussed further in section 6.3.1.1. The fact that they reach full extraction is attributed to the bubble size and their low kinetic energy compared to the air bubbles.

For both mixtures, the transition from partial (the sloped section of the curve) to full extraction (the available gas plateau) is experimentally shown to be a gradual change, yet the DGM prediction indicates a sharp change. The single-phase DGM accounting for compaction show a similar shape to the experimental data here, but the trend is not apparent until higher pressure differences. Darcy's Law makes the same predictions and therefore it is necessary to produce a model to account for this gradual slope change from partial to full extraction. This topic is discussed in sections 6.3.2 and 6.3.3.

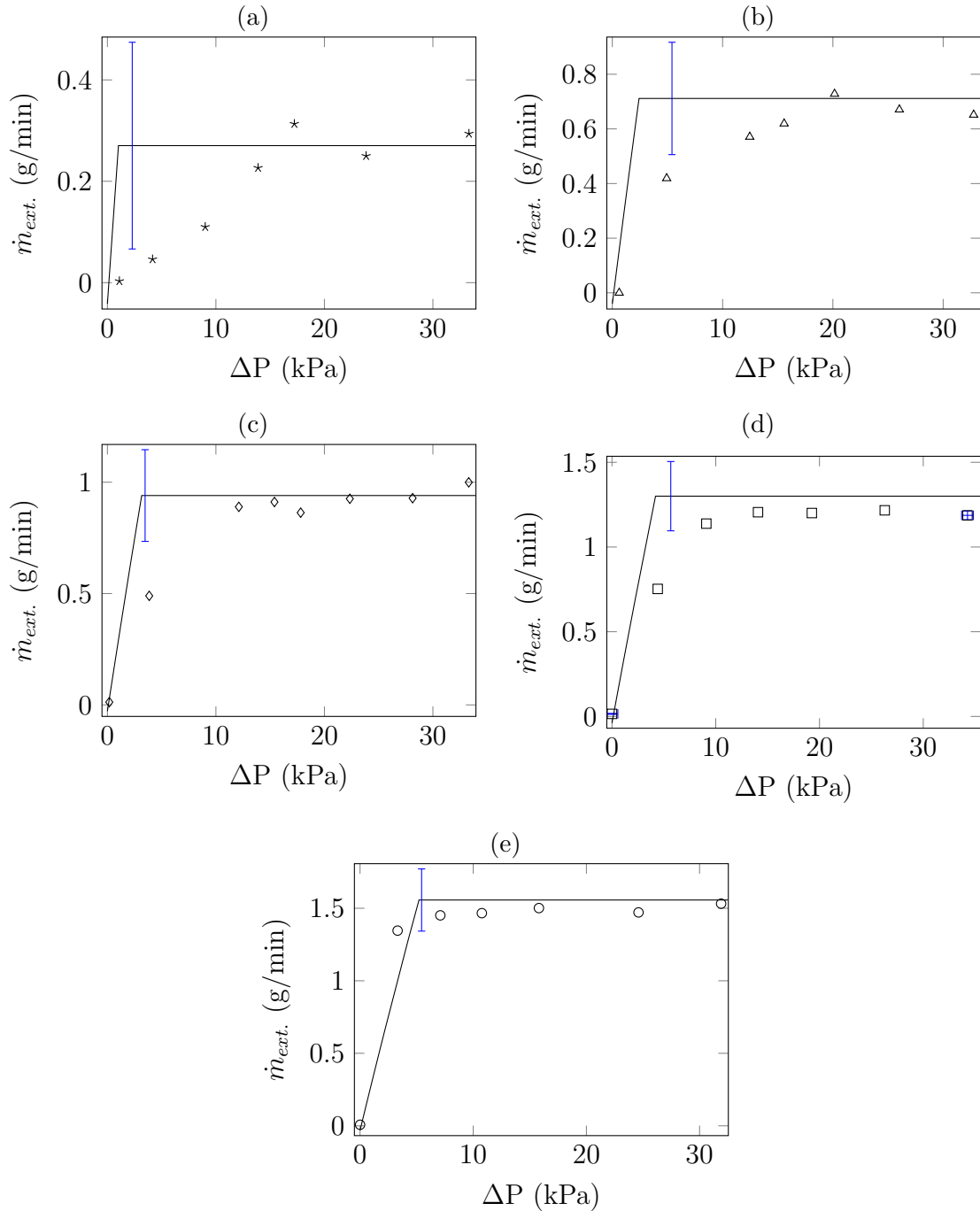


Figure 6.13: Liquid-vapor flow rate predictions from the dusty gas model accounting for compaction with Eq. (2.19) and Eq. (5.20) where $\delta' = \delta'_{vap.}$ and flow area is scaled by the annular Armand-corrected void fraction; symbols correspond to Table 6.1 on pg. 90.

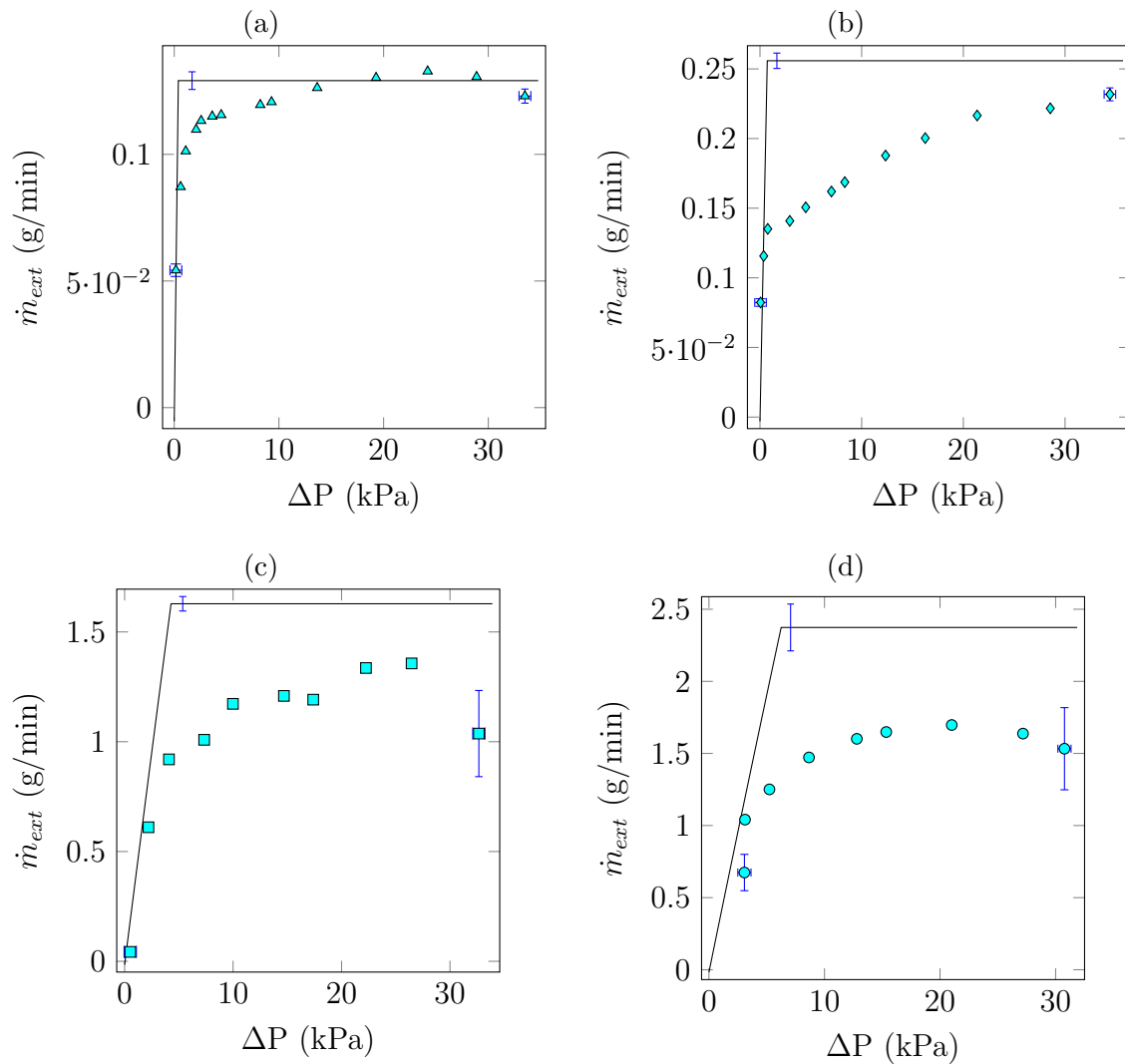


Figure 6.14: Liquid-air flow rate predictions from the dusty gas model accounting for compaction with Eq. (2.19) and Eq. (5.20) where $\delta' = \delta'_{air}$ and flow area is scaled by the annular Armand-corrected void fraction α_{AA} listed in Table 6.5; symbols correspond to Table 6.1 on pg. 90.

6.3 Generalized Models for Two-phase Gas Extraction

As a result of the compaction-corrected and estimated area-corrected Darcy's Law and DGM predictions not agreeing with the measured extraction data, the area corrections are modified based on measured data. In addition to providing more accurate extraction predictions, non-dimensional models give insight into the forces influencing the extraction behavior of each mixture. The assumptions used to estimate the reduced extraction area in section 6.2 are invalidated by hydrodynamics at the mixture-membrane interface as is discussed in section 6.3.1.

Non-dimensional models for the DGM and Darcy's Law are considered in sections 6.3.2 and 6.3.3, respectively. These models can be modified with a constant or pressure-dependent area correction and are designed to collapse the liquid-air and the liquid-vapor data cases into a single curve. When collapsing the data cases, the lowest available gas flow rate of liquid-vapor (0.26 g/min, Fig. 6.13a) is excluded from the curve fits because some measurements from this case do not fall in the trend. There is likely a source of experimental error at pressure differences below 10 kPa because the higher pressure difference data points collapse well with the other data cases. This deviation is likely due to the extraction mass flow rates being low and therefore the catch-and-weigh values are strongly dependent on the spacing of liquid slugs in the condenser which could be shifting the data.

After presenting one constant area correction DGM model and three pressure-dependent area correction DGM models in section 6.3.2, the best fit DGM scaling variables are applied to Darcy's Law. The same scaling variables applied to the DGM

do not collapse Darcy's Law, so one alternative pressure-dependent area correction Darcy's Law is presented in section 6.3.3. After finding Darcy's Law would require additional modification to collapse both mixtures, the compaction and area correction terms are absorbed into the two-phase permeability. This permeability is subsequently non-dimensionalized by the mean single-phase permeability and scaled with the same variables used to collapse the DGM for a more accurate fit. Finally, a recommended generalized model from both the DGM and Darcy's Law are presented in section 6.4.2 along with a description of the method to apply the models to predict gas extraction rates from two-phase mixtures.

6.3.1 Model Considerations

It is necessary to account for the hydrodynamics at the fluid mixture-membrane interface to accurately predict gas extraction rates. The *estimated* area correction term introduced in section 6.2 is a constant which merely changes the slope of the DGM or Darcy's Law predictions. Therefore, the intersection of the partial and full extraction curves (sloped curve and plateau) is predicted to be abrupt, when in fact it is measured as a gradual transition. A pressure-dependent area correction term therefore needs to be applied to the models. The area available for extraction depends on the hydrodynamics at or near the mixture-membrane interface. These exo-membrane hydrodynamics include three phase contact, thin film rupture and bubble kinetic energy as described in section 6.3.1.1. The estimated area correction term could be better estimated if the thin film rupture behavior and bubble geometry

during extraction were accounted for. The thin film likely ruptures at a different rate when the pressure difference is increased, furthermore the bubbles may not be able to neck completely and therefore the extraction area remains small at high pressures.

An empirical area correction term accounts for the combined effects of hydrodynamics at the mixture-membrane interface so existing gas transport models can better predict two-phase gas extraction. The method to determine the empirical area correction term is first presented in section 6.3.1.3. The variables capturing the hydrodynamic behavior at the mixture-membrane interface are discussed in section 6.4.1. The physics of these hydrodynamics can be related to the fluid properties presented in section 6.4.1. The empirical area correction terms are calculated from select data as described in section 6.3.1.3. This select data can be collapsed by variables which change between each of the nine individual data cases as described in section 6.3.1.4, then the data from each mixture can further be collapsed to produce a single curve fit as explained in section 6.3.1.5.

6.3.1.1 Hydrodynamics at the Mixture-membrane Interface

The purpose of this section is to discuss the drastic difference in the compaction- and void fraction-corrected extraction predictions for two-phase flow compared to the measured extracted gas as seen in Figs. 6.11 and 6.12 for Darcy's Law and Figs. 6.13 and 6.14 for the DGM. Information in this section is more qualitative than quantitative because the scope of the study is on time-averaged extraction not the specifics of the dynamic liquid-membrane interface.

The high speed videos are the source of information in evaluating the hydrodynamics at the surface of the membrane. As seen in Figs. 6.14c and 6.14d the liquid-air data pre-maturely plateaus whereas the the liquid-vapor case of comparable available gas reaches full extraction. Note that the 1.38 g/min case in Fig. 6.13d arguably does not meet the plateau but this is likely due to the fact that the supplied liquid for vapor generation is 4 g/min compared to 10 g/min (see Table 4.2) which results in more vigorous boiling resulting in more heater block losses. While these losses were accounted for, assumptions were made which limit the accuracy of the calculations. It is unlikely that hydrodynamics are separating the experimental plateau from the predicted plateau, because the experimental plateau falls within the uncertainty of the expected one (± 0.2 g/min).

Upon analyzing the bubble size and behavior in the high speed videos, the vapor bubbles are larger than the air bubbles. A select frame from each case is shown in Fig. 6.15 where the frames are scaled to have the same length scale. Note that the camera calibration varied for each case, a test calibration image has under 5% uncertainty as seen in appendix F.3 but there was no Lexan[®] window or water between the membrane and the camera when quantifying this uncertainty.

Bubble diameters are determined manually by measuring the bubble width and approximating this as the diameter, a summary of the bubble diameters is in Table 6.6. The uncertainty is of the mean bubble diameter, so bubbles vary in size by more than the tolerance shown. However, if another set of bubble samples were to be measured, there is 95% confidence that their mean diameter would be within this range.

In regards to the difference between the bubble stability of both mixtures, the

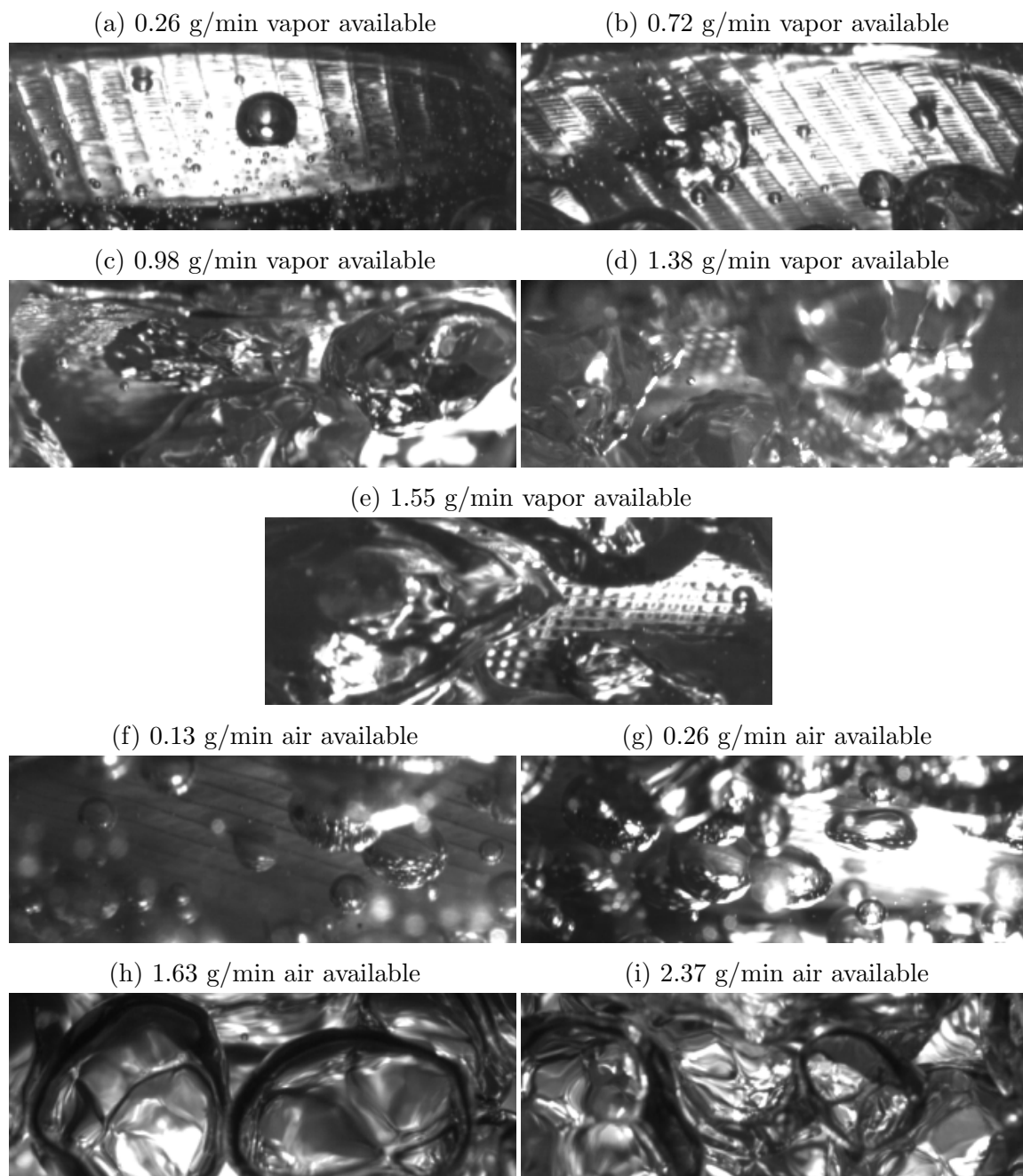


Figure 6.15: Two-phase images at the maximum pressure difference in the first cycle of each data case from high speed video scaled consistently: horizontal field of view is 15 mm. (a)-(e) are liquid-vapor and (f)-(i) are liquid-air; the grid lines are the outlines of the membrane ribs underneath the PTFE laminate, only visible because of the applied pressure difference across the membrane. Note that camera angle varies for each case.

Table 6.6: Bubble diameters and void fraction for all two-phase experiments. Note: the 0.26 g/min available vapor case disregards tiny bubbles from the mean bubble diameter calculation, these can be seen in the background of Fig. 6.15a

Phases	Nominal Available Flow Rate		Bubble Dia. (mm)	Void Fraction (%)	
	$\dot{m}_{\text{avail.}}$ (gpm)	$Q_{\text{avail.}}$ (mL/min)		β	α_{AA}
Liquid-Vapor	0.26	436	3.7 ± 0.9	97.8	20.5
Liquid-Vapor	0.72	1208	6.0 ± 0.9	99.2	41.5
Liquid-Vapor	0.98	1644	7.3 ± 0.7	99.4	48.5
Liquid-Vapor	1.38	2315	7.9 ± 0.9	99.9	68.1
Liquid-Vapor	1.55	2601	8.8 ± 1.1	99.7	61.7
Liquid-Air	0.13	99	2.0 ± 0.4	90.7	4.5
Liquid-Air	0.26	195	2.1 ± 0.3	95.2	8.8
Liquid-Air	1.63	1208	4.9 ± 0.6	99.2	36.5
Liquid-Air	2.37	1733	5.3 ± 0.8	99.4	48.2

Laplace equation can predict the pressure in a bubble. The larger the bubble, the closer the pressure is to the pressure of the fluid surrounding it. This does not explain why the vapor bubbles are extracted more readily than the air bubbles, because the air bubbles are smaller. In regards to the form of the bubbles, both are reminiscent of slightly compressed spheres (resulting in oval cross sections) when the diameter is about 5 mm or greater. The major difference between the bubbles' behavior is that the vapor bubbles rippled and tended to agglomerate with other bubbles as seen in Fig. 6.15e. This was not true with the air bubbles as can be seen in Fig. 6.15h where the bubbles have a distinct outline.

Another major difference between the mixtures' hydrodynamics is in the formation of a three phase contact (TPC) line. The TPC is formed when the liquid film between the solid (membrane) and bubble is ruptured as seen in Fig. 6.16e. At this point, the

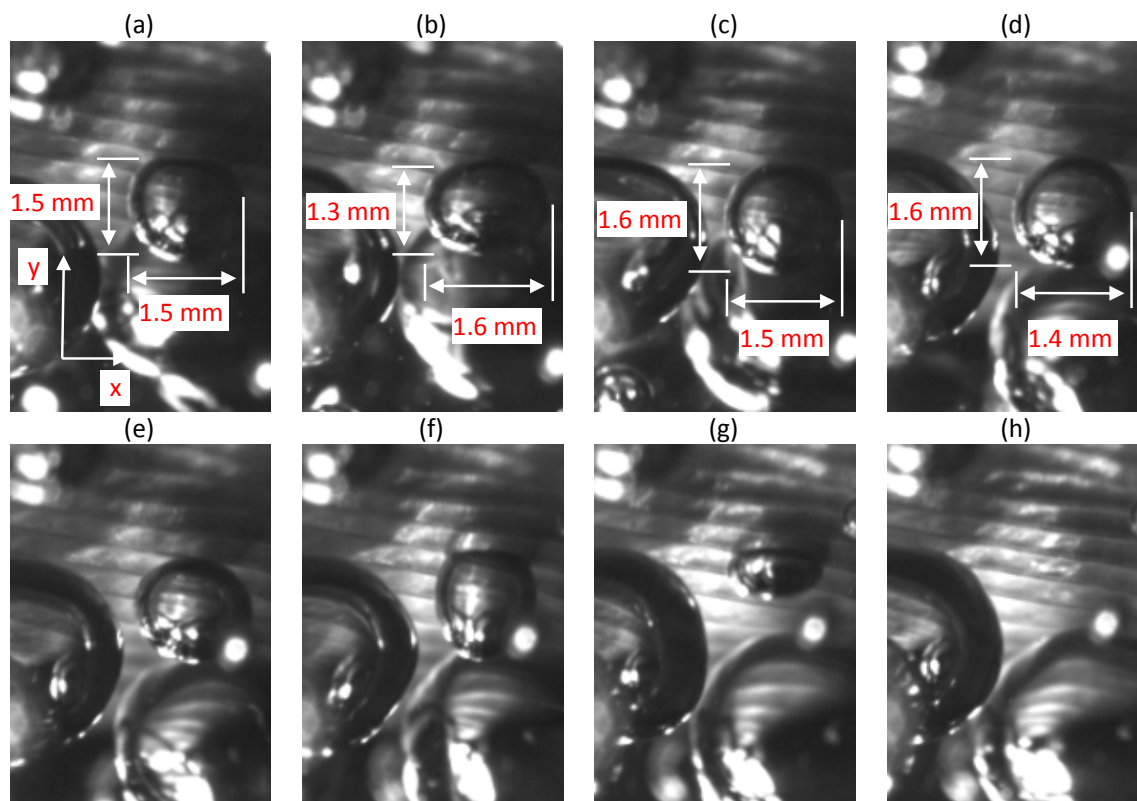


Figure 6.16: Air bubble interaction with membrane; images are from 0.26 g/min liquid-air case with 32 kPa pressure difference across membrane. Gravity is in the negative y-direction perpendicular to the face of the membrane. See Table 6.7 for a detailed description of collision times.

Table 6.7: Bubble collision times corresponding to Fig. 6.16

Subfigure	Time (ms)	Collision Number	Contact (ms)	Notes
(a)	0.0	1		First collision
(b)	1.7			Greatest compression
(c)	3.3		3.3	Last frame prior to departing
(d)	15.0	2		
(e)	17.1		2.1	First sign of extraction: necking
(f)	19.0			Bottom of bubble still at same y-location
(g)	20.7			Full diameter of bubble at membrane
(h)	21.7			Fully extracted, process lasts 4.6 ms

gas in the bubble begins to flow through the pores of the membrane if there is a sufficient pressure difference driving it. Once the TPC is formed, the ridge of the film is known to recede due to the balance of surface tension forces even without a vacuum-driven pressure difference [35, 47] as seen in Fig. 6.16f where the bubble is necking. This process is very rapid, but the capture frequency of the video here is fast enough to see the bubble necking. If the pressure difference across the membrane is low, the TPC ridge expands until the forces are balanced as seen in Fig. 6.17. The contact angle here is clearly greater than 90° showing the surface's affinity for gas.

Krasowska et al. [37] found that the surface roughness causes the TCP line to form after fewer collisions but does not affect the bubble behavior up to this point. This makes it difficult to determine what the role of the roughness is because the pressure is likely the ultimate cause of the ruptured liquid film. While the small pore sizes of the membrane should signify that the surface is more smooth than the smoothest ($<1\mu m$ RMS) rough surface studied by Krasowska et al. [37], it would need to be measured, say by an atomic force microscope because optical profilometers such as Zometric's ZeScope do not have high enough resolution.

Since the roughness of the pores in this PTFE membrane is likely on the same order of magnitude as the smooth surface studied by Krasowska et al. [37], its bubble dynamics will be compared. This assumption is based on the roughness measurements of a $0.44\mu m$ pore diameter polyvinylidene fluoride (PVDF) membrane which has an RMS roughness of $0.015\mu m$ as determined by Khayet et al. [17]. It is unclear whether this PVDF membrane is nanofibrous or hollow fiber, but if it is nanofibrous then the geometry is nearly identical to that of the PTFE membrane studied here. It is likely

nanofibrous because of its high porosity ($\epsilon = 0.705$).

The bubble in Fig. 6.16 has a measured approach velocity of approximately 0.4 m/s, as determined using Open Source Physic's Tracker software [45]. This value is comparable to the terminal velocity of 0.35 m/s due to buoyant forces for the similar sized bubble (1.48 mm dia.) studied by Krasowska et al. [37]. The difference in velocity is likely attributed to the bubble's inertia because the gas is driven through the bubbler. For their smooth surface, the bubble did not form a TPC line with the Teflon[®] until it collided 5 times, bouncing off of surface between collisions. From their data, it appears that necking occurs at 83.6 ms without the aid of an applied pressure. This time period is about five times longer than the time to begin extraction here as seen in Fig. 6.16e. The time between the first two collisions is consistent with this study and Krasowska et al. [37] where all roughnesses result in the same contact time between the first and second collision. Therefore the only variable which is of

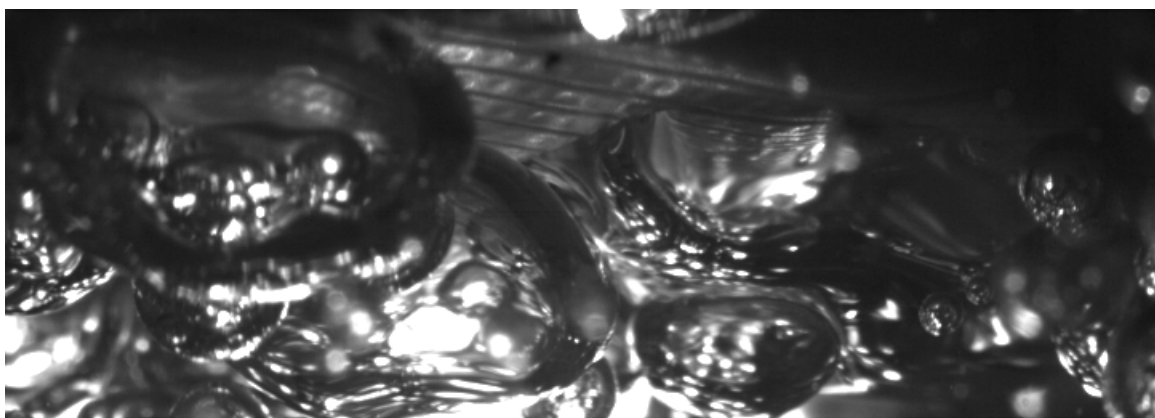


Figure 6.17: Air bubble forming an immobile air pocket with another bubble approaching colliding, image is from 0.26 g/min liquid-air case with 1 kPa pressure difference across membrane.

interest is the number of collisions. Since this bubble only collided twice compared to five times as found by Krasowska et al. [37], it is evident that extraction aids in the rupture of the thin film and the velocity of the retreating ridge of the film. Krasowska et al. [37] images show an approximate 6 ms time period between initial necking and the ridge of the film reaching the bubble diameter, whereas here it only takes about 3.6 ms.

It should be noted that the roughness due to the pores is not the only roughness that the membrane's surface exhibits. When pressures are applied to the membrane, the PTFE compacts such that concave dimples are formed between the ribs of the scrim backing. This creates a macro-scale roughness resembling a dimpled surface as is evident in Fig. 6.15e. These dimples are known to have an elliptical shape with major and minor radii of approximately 0.4 mm and 0.15 mm defined by the perforations in the PP scrim of Fig. 4.1. This would result in a macro-scale roughness and a significant increase in overall roughness compared to the micro-scale roughness of the pores alone.

In regards to the different bubble velocities prior to the first collision, when the air bubble leaves the porous plate used to disperse the bubbles, it already has energy associated with it because the air must be forced through the porous disc by pressurizing it to 10 kPa above atmosphere (note that the majority of this pressure drop is due to the porous nature of the bubbler). There is a different scenario when considering the vapor bubbles. The vapor is generated by phase change where the only reason the bubbles depart is due to buoyant forces overcoming surface tension forces. Therefore, there is less initial vapor bubble inertia and the vapor bubbles

may not even reach terminal velocity by the time they reach the membrane (≈ 25 cm). Krasowska et al. [37] found that for a 70% decrease in velocity from 0.35 m/s to 0.10 m/s the TPC time decreased 60% from 84 ms to 35 ms. This helps to explain why the liquid-vapor plateaus match the available gas. The higher mass flow rates of liquid-air have a higher kinetic energy than the vapor bubbles and tend to bounce off the membrane because the first few collisions do not dissipate enough energy to form a stable contact. Since the bubbles are more likely to bounce, they will have more time to avoid being extracted and possibly vent through the excess port.

6.3.1.2 Selection of the Scaling Variables

The goal of the scaling variables is to develop a single equation which can describe the experimental data with a single curve fit. This means incorporating relevant fluid properties and experimental conditions. The resulting area correction curves which will be presented in section 6.3.2 and section 6.3.3 are still non-dimensional, but they will be scaled to capture the physics of the given experimental conditions.

If hydrodynamics were not influential, one would expect the behavior of the vapor in the liquid-vapor cases to be similar to that in the single-phase superheated vapor experiment because the mean temperature in the membrane only differs by 5°C. Likewise for the liquid-air where the single-phase air test is at the same temperature as the two-phase tests, the transition from partial to full extraction (intersection of extraction predictions and plateau) is influenced by something other than compaction and a time-averaged effective extraction area. This is apparent because the transition

is smooth not abrupt as predicted. Considering the hydrodynamics cause the DGM and Darcy's Law predictions to deviate substantially from the measured data prior to reaching the plateau, the non-dimensional variables will capture hydrodynamics external to the membrane.

When selecting the non-dimensional variables, the liquid-vapor data can be collapsed separately from the liquid-air data by using a variable which varies between each case of data. This results in a set of empirical fits for each mixture which is less useful than a single model which encompasses multiple mixtures. Therefore, the data is first scaled by a variable which collapses the mixtures individually such as the void fraction, quality or available gas, then the two "bands" of data (liquid-air and liquid-vapor) are collapsed with their thermophysical properties. The other advantage of producing a fit which encompasses both mixtures is that the thermophysical properties help eliminate the need for length scales when non-dimensionalizing the available mass flow rate of gas. The benefit of excluding length scales is that they result in a less universal model. If the extraction area, plenum geometry or pore size varied in these experiments, a length scale would be necessary but the geometry and membrane was constant for the nine data cases of this study.

6.3.1.3 Empirical Effective Extraction Area

The measured extraction data from the two-phase data cases can be better predicted by modifying the membrane extraction area with a scaling term Φ_m , see Eq. (5.34), other than the void fraction. When considering a single case of data,

determining the empirical area correction term can be achieved in one of two ways as was described in section 5.6.2. The simpler of the two methods results in a single area correction term for each data case and the more complicated method results in a pressure-dependent term for each data case. The area correction term is only necessary prior to reaching full extraction, so only those data are used to calculate the area correction term. To determine what data is considered, an exponential fit of the form

$$\dot{m}_{ext} = \dot{m}_{plateau,exp} \exp(\Delta P n) \quad (6.2)$$

is applied to each case of data where n has units of 1/kPa. The form of the curve fit results in a horizontal asymptote, or plateau, defined by $\dot{m}_{plateau,exp}$ in Eq. (6.2). This experimental value is displayed in Table 6.8 compared to the measured available gas. The experimental plateau is typically lower than the amount of gas available for extraction.

The experimental plateaus listed in Table 6.8 are used as a criteria for selecting the data points to be considered to fit the area correction term. Starting at zero pressure difference, the data points are considered as long as they are less than 90% of the experimental plateau. The first data point within 10% of the plateau is also included in the data set to be analyzed, but none after it. The data considered are indicated by the filled markers shown in Fig. 6.18.

Table 6.8: Experimental plateau as determined from Eq. (6.2) compared to the theoretical plateau i.e. the available gas.

Fluid	Extraction Plateau (g/min)	
	Experimental	Theoretical
Liquid-vapor	0.31	0.26
	0.68	0.72
	0.95	0.98
	1.24	1.38
	1.49	1.55
Liquid-air	0.12	0.13
	0.18	0.26
	1.23	1.63
	1.65	2.37

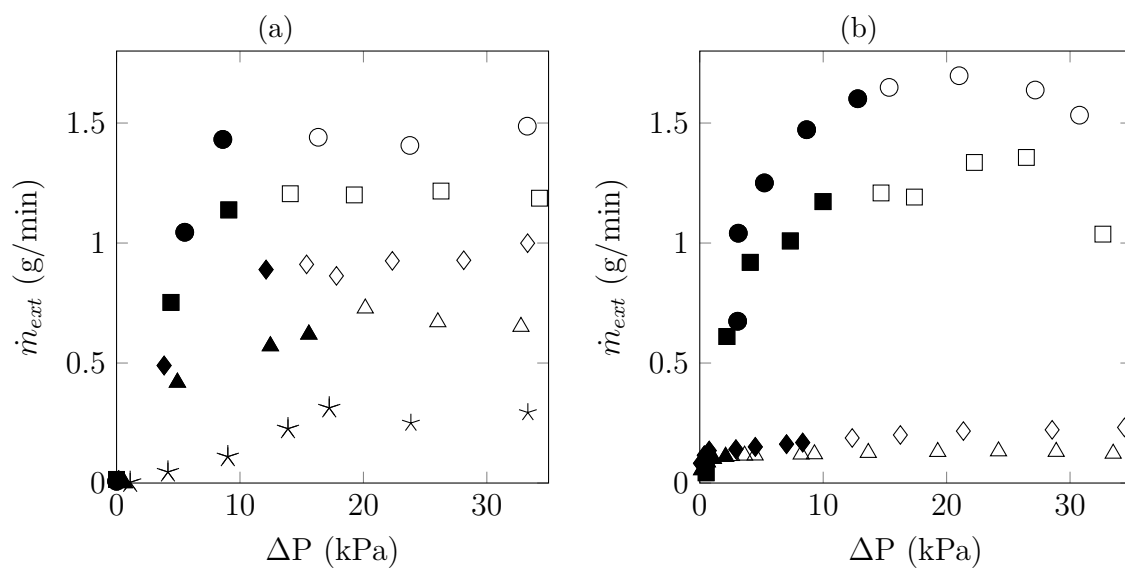


Figure 6.18: Filled data points are those considered to determine the two-phase extraction area correction term Φ_m for (a) liquid-vapor and (b) liquid-air. Criteria for selected data points is to be less than 90% of the experimental plateau, including the next point.

6.3.1.4 Collapsing Curves for Individual Mixtures

The liquid-vapor data can be collapsed into a “band” independent of the liquid-air data by using a variable which changes between each case of data i.e. a “case-specific” variable. The only case-specific variables are related to the available gas, which are the void fraction and quality. Ideally, the area correction term could be related to the void fraction or quality, but as is shown in section 6.3.2, these variables do not correlate with the empirical area correction values. The available mass flow rate is found to correlate well with the area corrections, resulting in a curve fit which fits the data well. After scaling the two sets of data by case-specific variables, two bands of data (liquid-air and liquid-vapor) result. As shown in the next section, these bands are collapsed with “mixture-specific” variables such as thermophysical properties.

6.3.1.5 Collapsing Curves Between Mixtures

This section considers mixture-specific variables which can be used to scale the liquid-vapor and liquid-air bands of data to collapse them into a single band. There are different thermophysical properties associated with the liquid-air and liquid-vapor mixtures due to temperature differences and dissimilar fluids as seen in Table 4.3, therefore a combination of mixture-specific variables will potentially scale each band so they coincide. The choice of mixture-specific variables is approached by realizing that most of the flow characteristics within the membrane are accounted for by using Darcy’s Law or the DGM as a base model to capture the effects of flow regime in the membrane. Therefore, non-dimensional numbers like the Knudsen number should be

avoided because it would be repetitive to account for pore-to-gas collisions.

The variables which influence the effective extraction area are related to the hydrodynamics in the inlet plenum including bubble dynamics, thin film rupturing and the three phase contact behavior between the gas, the liquid and the membrane. These hydrodynamics are influenced by viscous, buoyancy and surface tension forces. Therefore the potential variables which can be used to relate the two mixtures are the density and dynamic viscosity of the gas and liquid in the plenum, the contact angle of the membrane and the surface tension between the liquid and gas. The Bond number,

$$Bo = \frac{g(\rho_l - \rho_g)L^2}{\sigma_{lg}} \quad (6.3)$$

takes surface tension and buoyancy into account. Both of these forces are important in the inlet plenum because buoyancy drives the bubbles toward the membrane and three phase contact formation with the membrane depends on the surface tension. Calculating the Bond number reveals that the surface tension forces play a more significant role in the bubble behavior than the buoyancy forces when the length scale is constant for the two mixtures. This is apparent because the denominator (surface tension forces) of the liquid-air Bond number is 22% greater than that of the liquid-vapor, yet the numerator (gravitational forces) is only 4% greater. This results in a liquid-vapor Bond number which is 17% greater than the liquid-air Bond number.

To include the membrane's influence on the hydrodynamics, the contact angle

of the membrane is employed. The relevant results from Table 5.1 are the apparent contact angle of water-air at room temperature ($\theta_{la}=134.4^\circ$) and water-vapor at saturated temperature ($\theta_{lv}=131.9^\circ$). The contact angle decreases with temperature because the surface tension between the liquid and gas phase decreases. The contact angle of liquid-vapor is only 2% less than air, but if the cosine of the contact angle is compared, the difference is slightly amplified to 4%. In either case, this effect is expected to be small for these data.

A summary of the mixture-specific variables which are used are presented in Table 6.9 with their influence on the scaling indicated by the ratio of one mixture to the other.

Table 6.9: Select mixture-specific thermophysical properties used to collapse data presented with a repeated list of symbols from Table 6.1.

Fluid	Symbol	$\dot{m}_{avail.}$ (gpm)	μ_g (Ns/m ²)	μ_g/μ_l	$[g(\rho_l-\rho_v)/\sigma]^{1/2}$ (1/m)	$g(\rho_l-\rho_v)/(\sigma d_p)$ (1/m)	Contact Angle (°)
Liq.-vap. (LV)	*	0.26	1.23E-05	4.36E-02	399	3.54E+11	131.9
	△	0.72					
	◇	0.98					
	□	1.38					
	○	1.55					
Liq.-air (LA)	△	0.13	1.83E-05	2.06E-02	369	3.02E+11	134.4
	◇	0.26					
	■	1.63					
	●	2.37					
	Ratio, LV/LA:		0.67	2.12	1.08	1.17	0.98

6.3.1.6 Form of the Non-Dimensional Curve Fits

When generating curve fits to relate the scaled area correction term to either the void fraction or pressure (independent variables), one of two exponential forms is used. They are very similar, but the independent variable is either multiplied by

$$\Phi_m^* = C \exp(-n\chi) \quad (6.4)$$

or raised to the modifier within the exponential

$$\Phi_m^* = C \exp(-\chi^n) \quad (6.5)$$

where χ represents the independent variable, either $\zeta\Delta P$ or α_{AA} , and ζ is 1/kPa. To determine the coefficients C and n , a least squares regression analysis is followed by a sensitivity analysis to truncate the best-fit coefficients individually. Each coefficient is truncated such that the MAE does not vary by more than three percent from the full precision coefficient's fit.

6.3.2 Modified Dusty Gas Model

To generate a single equation estimating the constant area correction terms, they are first considered as a function of the known void fraction. After scaling the area correction to collapse the liquid-vapor and liquid-air data, the void fraction is found to poorly predict extraction rates prior to reaching the theoretical full extraction plateau.

Therefore, various other methods are implemented to scale the area correction term and relate it to the pressure difference across the membrane. The next simplest method is to scale the empirical area correction term by the void fraction then relate it to the pressure difference across the membrane. After this, the area correction term is scaled by quality and subsequently by the available gas mass flow rate and related to pressure. The non-dimensional values are presented in Table 6.9 along with the same symbols from Table 6.1.

The area correction scaling properties are evaluated at the inlet plenum temperature and atmospheric pressure. Vapor and air properties in the DGM are evaluated at the inlet plenum temperature and the average pressure in the membrane.

6.3.2.1 Area Correction Scaled By Fluid Properties, Function of Void Fraction

The void fraction can be used to estimate the constant area correction term reasonably well as seen in Fig. 6.19a. To collapse the liquid-vapor and liquid-air data in this curve, the data are scaled by the Bond number, contact angle and ratio of phase viscosities

$$\Phi_m^* = \Phi_m \frac{1}{(-\cos\theta)} \left(\sqrt{\frac{g(\rho_l - \rho_g)}{\sigma_{lg} d_p^2}} \right) \frac{\mu_g}{\mu_l} \quad (6.6)$$

The issue with this area correction model is that the area correction was experimentally found to vary with the pressure difference, which was the issue with the void

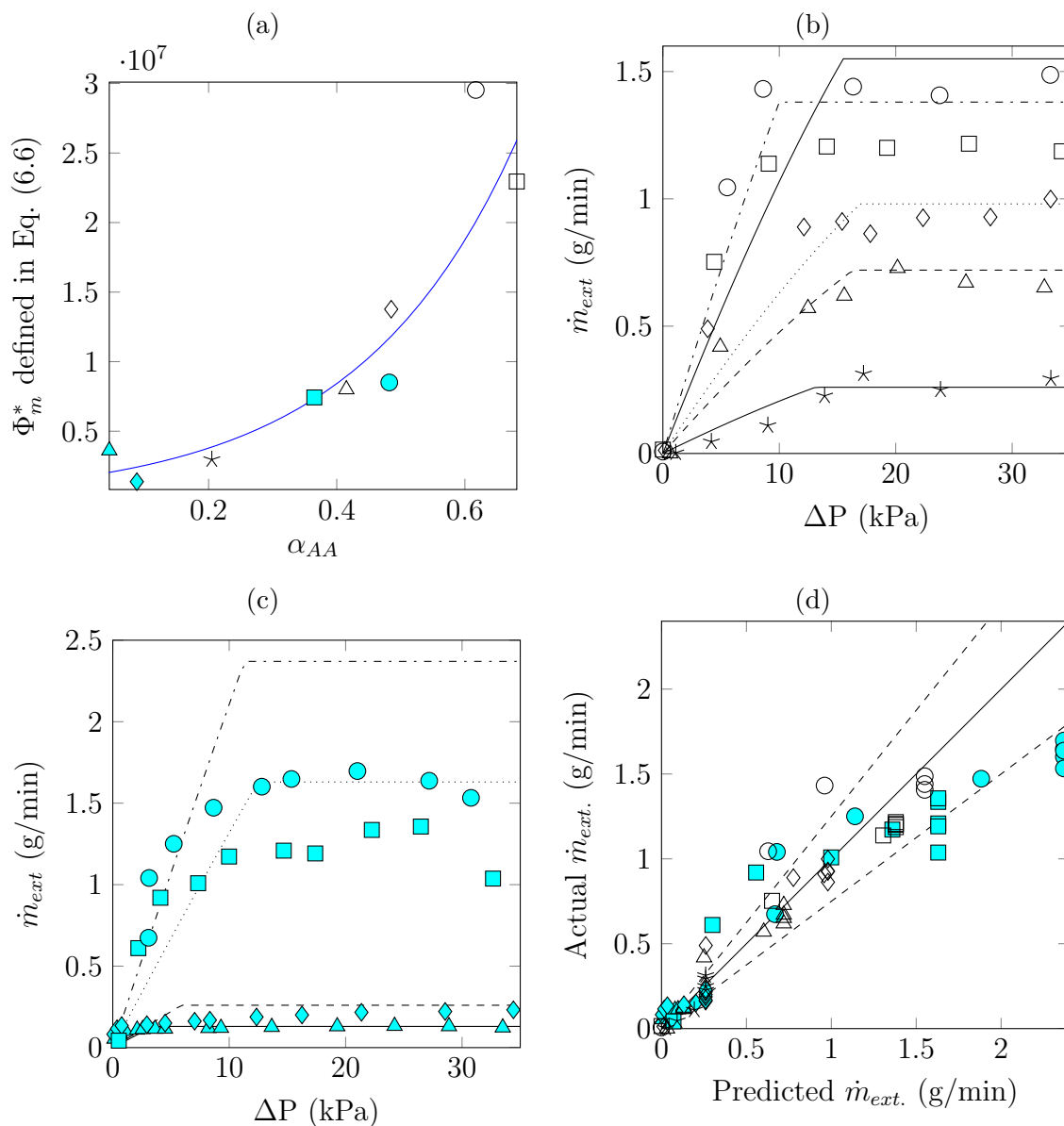


Figure 6.19: Extraction area correction term Φ_m^* as a function of void fraction: (a) exponential curve fit of the form Eq. (6.4) with $C = 1.7 \times 10^6$ and $n = -4$ (b) applied to liquid-vapor (c) applied to liquid-air and (d) compared to measured data with a $\pm 25\%$ error band. Symbols correspond to Table 6.9 on pg. 129.

fraction area corrections presented in Figs. 6.13 and 6.14. The only variables changing with pressure here are the density and the compaction, however compaction does not significantly influence the mass extraction until pressure differences of about 10 kPa as seen in Fig. 6.7. Therefore, the predicted extraction rates will increase as the pressure difference is increased. It is known that the most gas which can be extracted is that which is available, so the extraction rates are limited to the available gas. Empirically fitting a constant area correction merely reduces the overall MAE of all data cases by 1% as seen in the second DGM row of the model summaries presented in Table 6.12.

6.3.2.2 Area Correction Scaled By Void Fraction, Function of Pressure

To better fit the measured extraction data prior to full extraction, the empirical area correction is considered as a function of the pressure difference across the membrane. When the pressure difference is the independent variable, the area correction term decreases as the pressure difference increases which results in a curve that resembles the measured extraction behavior more accurately. The first case-specific scaling variable considered is the void fraction

$$\Phi_m^* = \Phi_m \frac{1}{\alpha_{AA}} \quad (6.7)$$

This equation seems to collapse the non-dimensional data as seen in Fig. 6.20a. However, when the non-dimensional area correction term is implemented to determine the quality of fit, the predictions result in an overall MAE which increases by 3% when

the void fraction is the independent variable. This can be visualized in Figs. 6.20b and 6.20c and is quantified in the third DGM row of the model summaries presented in Table 6.12.

This non-dimensional area correction term does not over-predict the liquid-air extraction rates as was found with Eq. (6.6), rather it under-predicts the extraction. When implementing this model as is seen in Figs. 6.20b and 6.20c, full extraction is defined by the available gas or the maximum extraction rate, whichever is reached first.

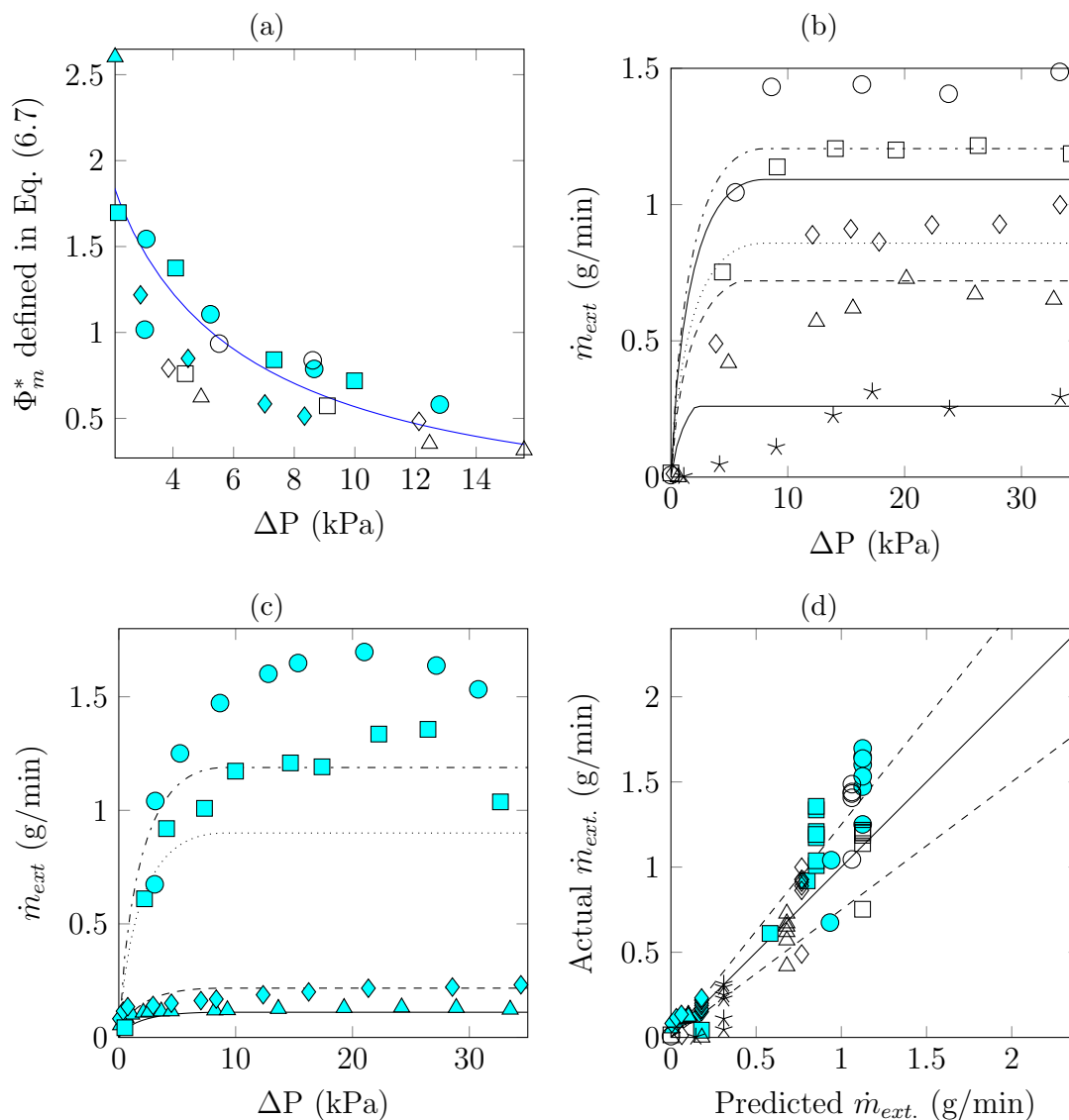


Figure 6.20: Extraction area correction term Φ_m^* as a function of pressure: (a) exponential curve fit of the form Eq. (6.5) with $C = 7$ and $n = 0.4$ (b) applied to liquid-vapor (c) applied to liquid-air and (d) compared to measured data with a $\pm 25\%$ error band. Note: top solid line in (b) is the prediction for the "o" markers. Symbols correspond to Table 6.9 on pg. 129.

6.3.2.3 Area Correction Scaled By Quality, Function of Pressure

As an alternative to the void fraction as a case-specific scaling variable, the quality is considered. The quality is defined as the ratio of available gas mass flow rate to inlet liquid mass flow rate. The combination of mixture-specific variables which collapse the data best is

$$\Phi_m^* = \Phi_m \frac{1}{x} \frac{1}{(-\cos\theta)} \left(\sqrt{\frac{g(\rho_l - \rho_g)}{\sigma_{lg} d_p^2}} \right) \frac{\mu_l}{\mu_g} \quad (6.8)$$

For this curve fit, the lowest available flow rate of air was excluded in addition to the lowest available flow rate of vapor. The data collapse well except for the high quality liquid-vapor case (1.38 g/min) as seen in Fig. 6.21a. As stated previously, the quality for this case is out of trend with the available gas flow rates because the liquid inlet mass flow rate is only 4.5 g/min compared to 10 g/min like the rest of the cases. Excluding this one case in particular, the data can be well predicted as seen in Figs. 6.21b and 6.21c. If the available gas mass flow rate is considered instead of the quality as the case-specific scaling variable, the data will collapse better.

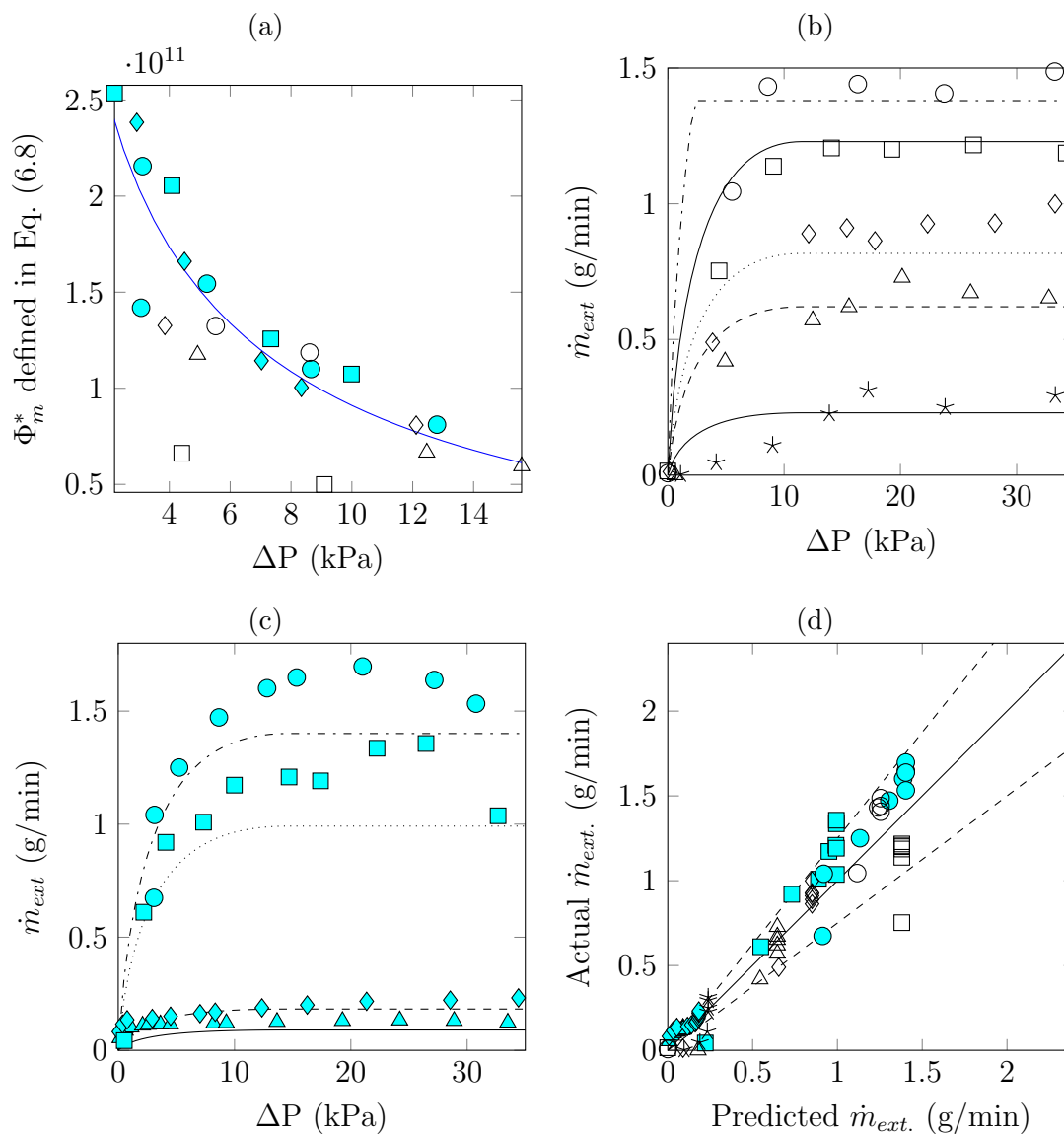


Figure 6.21: Extraction area correction term Φ_m^* as a function of pressure: (a) exponential curve fit of the form Eq. (6.5) with $C = 9 \times 10^{11}$ and $n = 0.36$ (b) applied to liquid-vapor (c) applied to liquid-air and (d) compared to measured data with a $\pm 25\%$ error band. Note: the top solid line in (b) corresponds to the “o” markers and the dash-dot line corresponds to the “□” markers. Symbols correspond to Table 6.9 on pg. 129.

6.3.2.4 Area Correction Scaled By Available Gas, Function of Pressure

Typically, it is desired to have a non-dimensional variable as an input to the non-dimensional models because they are more universal. However, in this case a dimensional variable is well suited for extraction predictions because the mass flow rate of gas and the driving pressure dictate the mass flow rate of gas being extracted. The reason why the quality does not predict the extraction rates well is because the liquid velocity is not changing the extraction behavior at these low flow rates (<10 g/min). Extraction rates are likely independent of liquid flow rate until a critical velocity is induced, this was studied by Xu et al. [20] in channel flows.

Since the two-phase extraction plateaus all increase with increasing available gas flow rate, a non-dimensional analysis which depends on the available gas mass flow rate is used in this section. The mass per time units of the case-specific variable (mass flow rate) are now non-dimensionalized to scale the pressure-dependent area correction. The resulting scaled equation is

$$\Phi_m^* = \Phi_m(-\cos\theta) \frac{\mu_g}{\dot{m}_{avail}} \sqrt{\frac{\sigma_{lg}}{g(\rho_l - \rho_g)}} \quad (6.9)$$

where the Bond number is no longer used, but instead a similar group of variables is used along with the gas viscosity.

When this this model is implemented, the data collapses well as seen in Fig. 6.22a. Furthermore, this model provides a smooth transition between partial and full extraction which is close to the measured values. This smooth transition is a result of the maximum extraction flow rate being lower than the available gas flow rates. This is

important for the liquid-air cases because in cases like Fig. 6.19c, the experimental plateaus can not be predicted.

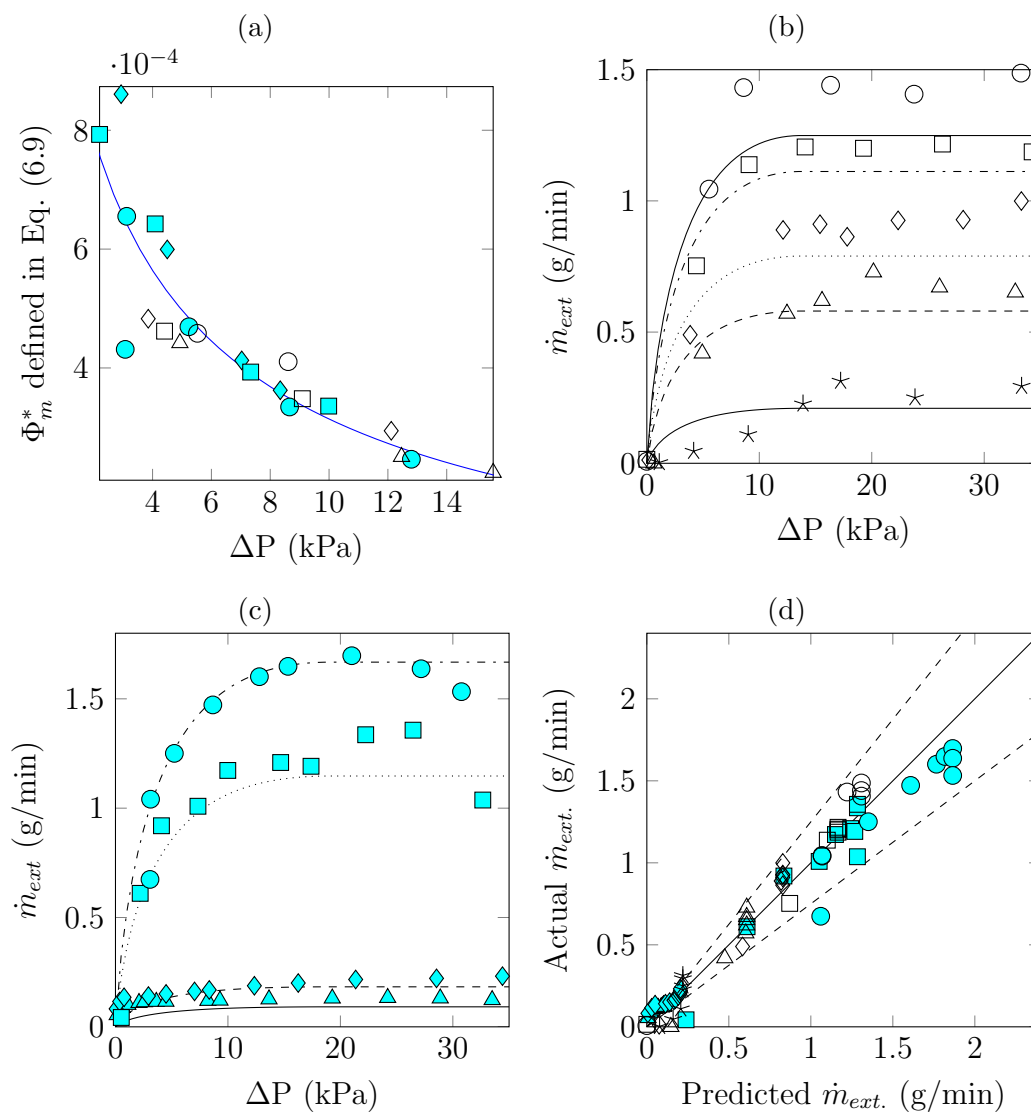


Figure 6.22: Extraction area correction term Φ_m^* as a function of pressure: (a) exponential curve fit of the form Eq. (6.5) with $C = 2.8 \times 10^{-3}$ and $n = 0.34$ (b) applied to liquid-vapor (c) applied to liquid-air and (d) compared to measured data with a $\pm 25\%$ error band. Symbols correspond to Table 6.9 on pg. 129.

6.3.3 Modified Darcy's Law

When the same non-dimensional equations used to collapse the dusty gas model are applied to Darcy's Law, the mixture-specific data cases collapse into bands based on the fluids used. To collapse these data, it is desirable to scale Darcy's Law by the two-phase permeability instead of using a compaction- and area-correction factor. This results in data which are better predicted but the relationship does not provide much physical insight.

6.3.3.1 Area Correction Scaled By Available Gas, Function of Pressure

When the same equation applied to the DGM, Eq. (2.19), is used to scale the best fit Darcy area correction values, the data do not collapse well as seen in Fig. 6.23. This is due to the fact that the slopes of the compaction-corrected curves are different as can be inferred from the superheated vapor curves Figs. 6.5 and 6.7 where Darcy's Law under-predicts the flow rate and the DGM over-predicts the flow rate at low pressure differences.

In an attempt to collapse the data further, the scaling term is modified to emphasize the gravitational and surface tension forces

$$\Phi_m^* = \Phi_m \frac{\mu_g(-\cos\theta)}{\dot{m}_{avail}} \frac{\sigma_{lg}}{g(\rho_l - \rho_g)d_p} \quad (6.10)$$

The only difference here is that the square root is removed and therefore a length scale is needed to keep the scaling term non-dimensional. The length scale is chosen

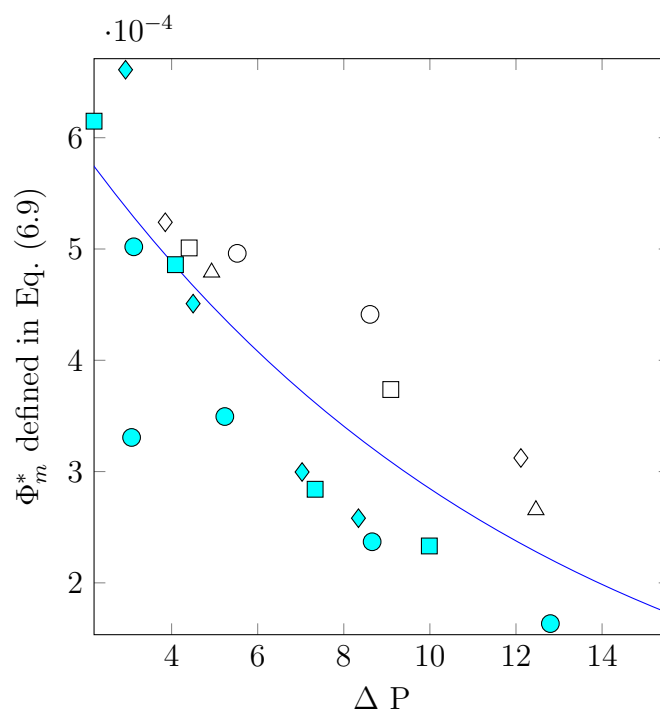


Figure 6.23: Darcy's Law best fit area correction term scaled with the same variables which collapsed the two-phase DGM data in Fig. 6.22a.

to be the pore diameter because it represents a membrane transport length scale.

The resulting non-dimensional area correction is slightly more collapsed as seen in Fig. 6.24a, but the curve fit over-predicts liquid-air extraction and under-predicts liquid-vapor extraction as seen in Figs. 6.24b and 6.24c.

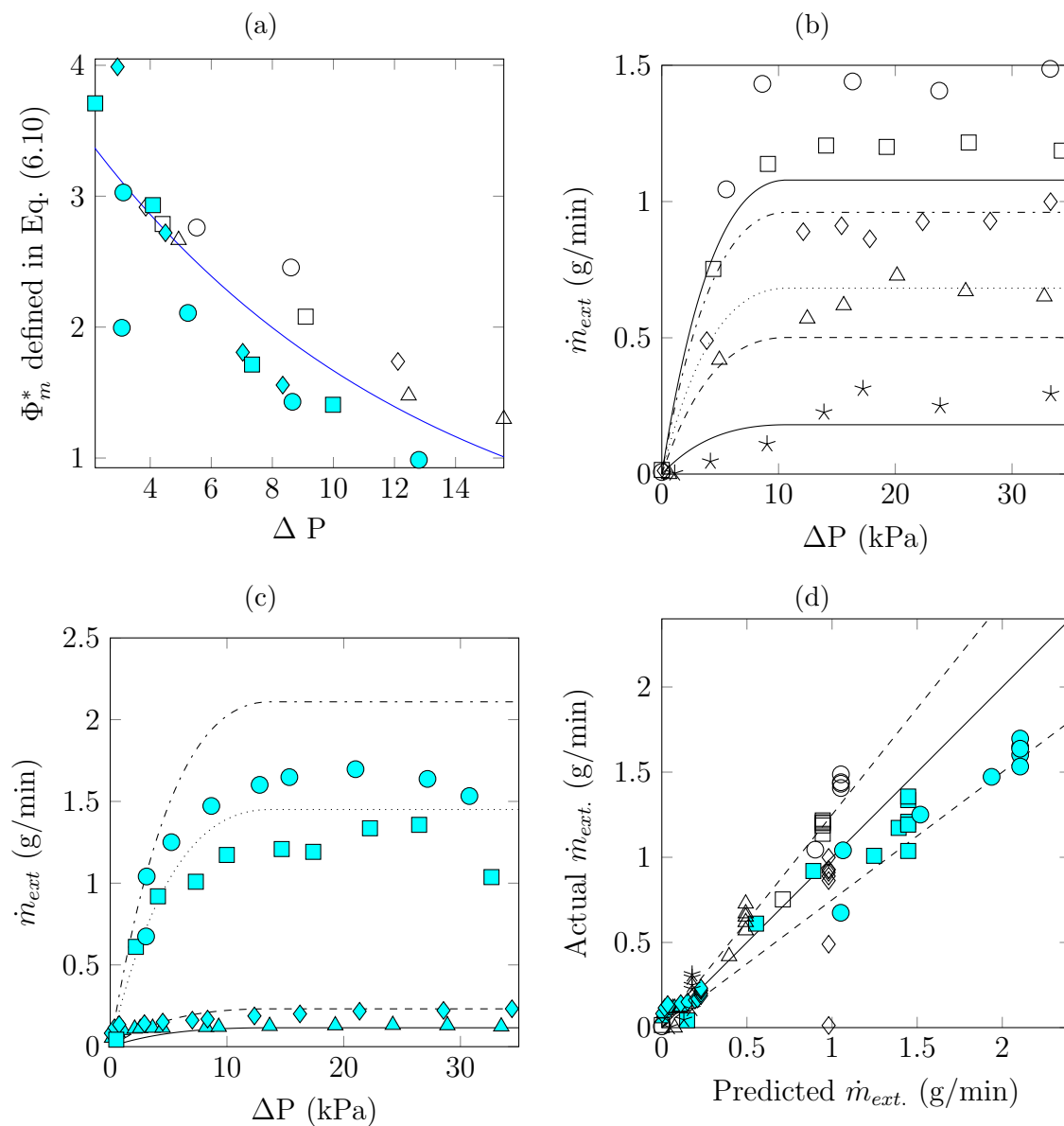


Figure 6.24: Extraction area correction term Eq. (6.10) as a function of pressure: (a) exponential curve fit of the form Eq. (6.4) with $C = 4.1$ and $n = 0.09$ (b) applied to liquid-vapor (c) applied to liquid-air and (d) compared to measured data with a $\pm 25\%$ error band. Symbols correspond to Table 6.9 on pg. 129.

6.3.3.2 Permeability Scaled by Available Gas, Function of Pressure

To achieve a curve fit which predicts extraction well at low pressure differences as seen in the DGM predictions of Fig. 6.22, an alternative approach is taken. It is possible that the data of Fig. 6.24a can be further collapsed, but it would require an additional empirical constant. Instead of using an area correction term, the permeability is used as the variable to be non-dimensionalized. Since the permeability has units of length squared, it needs to be scaled differently than the previous models in this chapter. However, if a variable can be employed to deem the permeability non-dimensional then the same groups mixture-specific variables can be applied. The intra-membrane hydrodynamics are captured by the single phase permeability, so this is a good value to non-dimensionalize the two-phase permeability with. This does not collapse the liquid-vapor or liquid-air data cases individually because it is a mixture-specific variable not a case-specific variable. Therefore, a case-specific variable must be included and the available gas mass flow rate is chosen because it was found to be effective in Fig. 6.22. The same mixture-specific variable as Eq. (6.9) is used to collapse the two-phase permeability data as

$$K_{D,lg}^* = \frac{K_{D,lg}}{\bar{K}_{D,g}} (-\cos\theta) \left(\frac{\mu_g}{\dot{m}_{avail}} \sqrt{\frac{\sigma_{lg}}{g(\rho_l - \rho_g)}} \right) \quad (6.11)$$

As was seen in Eq. (6.9), the available mass flow rate of air is the theoretical value, not the experimental plateau. For example, 2.37 g/min of air as measured at the bubbler is used, not 1.6 g/min where the data plateaus as seen in Fig. 6.14d. As was true for the data cases above, the lowest available gas flow rate of liquid-vapor

(0.26 g/min) is excluded from the curve fits. The resulting curve fit is displayed in Fig. 6.25.

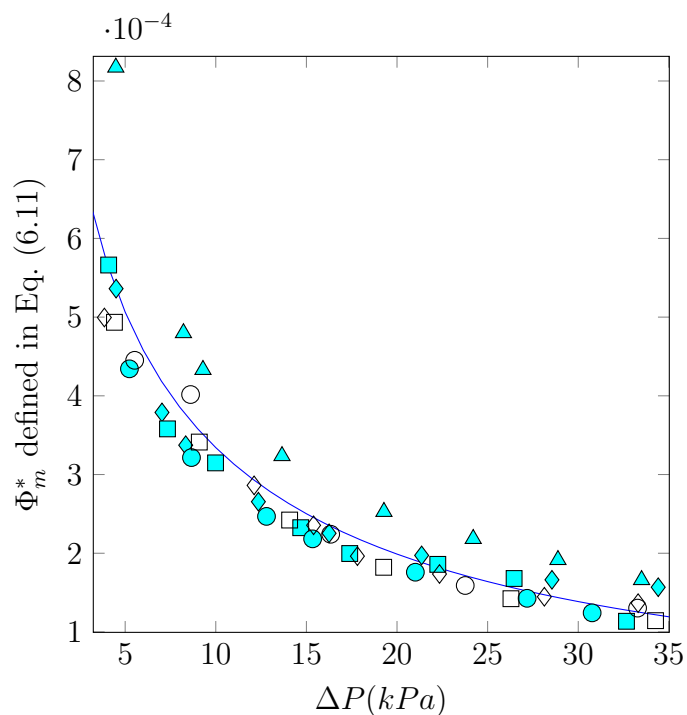


Figure 6.25: Liquid-vapor and liquid-air data scaled according to Eq. (6.11). Scaling values shown in Table 6.9, curve fit defined by Eq. (6.5) with $C = 2.7 \times 10^{-3}$ and $n = 0.32$. Symbols correspond to Table 6.9 on pg. 129.

Fig. 6.26 shows the permeability and mass flow rate based on the non-dimensional liquid-gas permeability equation, Eq. (6.11). The low available vapor flow rate case is well predicted except at low pressure differences even though it does not influence the fit. As quantified in Table 6.12, the extraction data are well predicted with an average MAE of 26%.

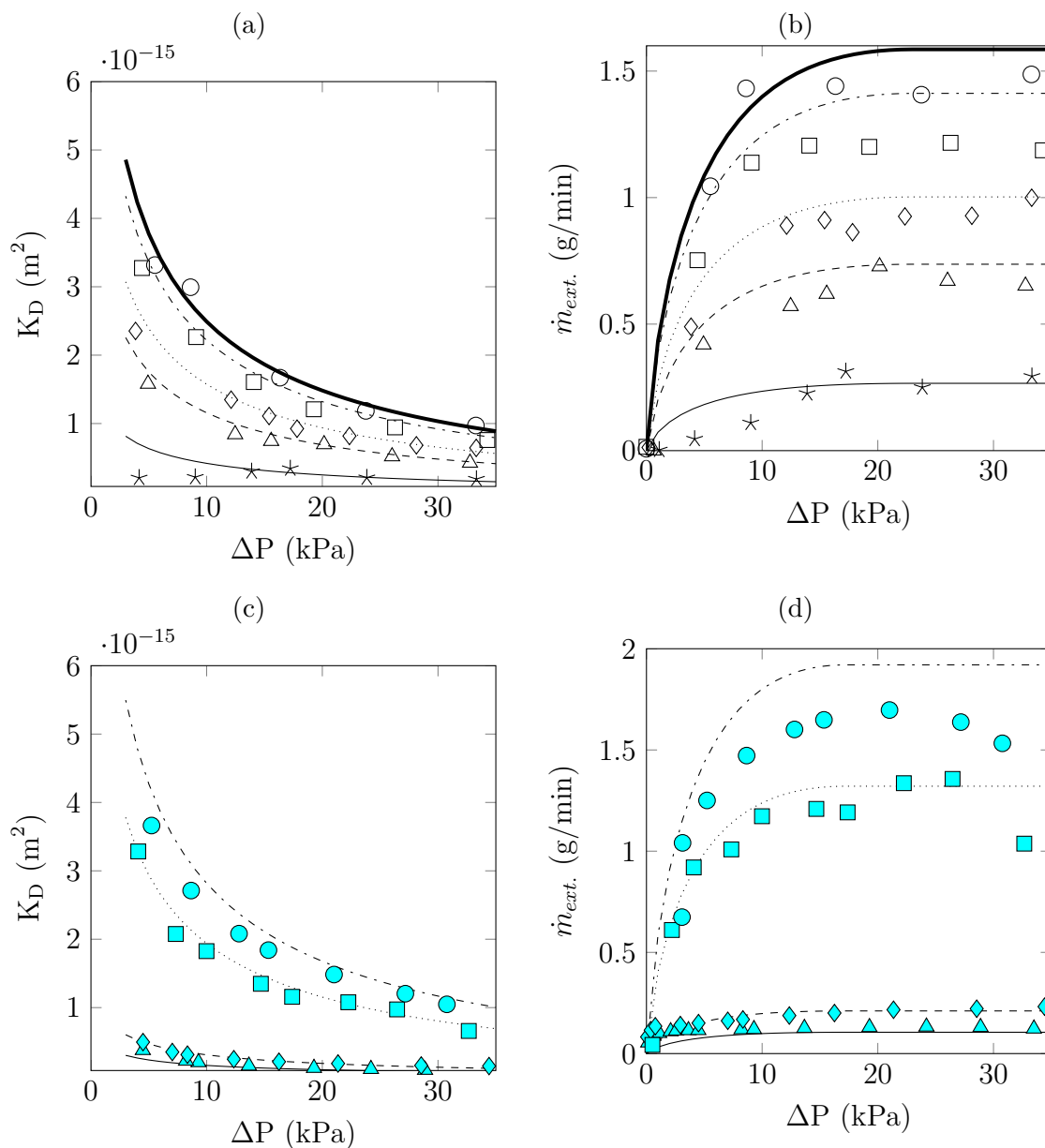


Figure 6.26: Darcy's Law *without compaction or area corrections* scaled according to Eq. (6.11). Showing measured and curve fit values for (a) and (b) liquid-vapor and (c) and (d) liquid-air. (a) and (c) are permeability and (b) and (d) are extracted mass flow rate. Symbols correspond to Table 6.9 on pg. 129.

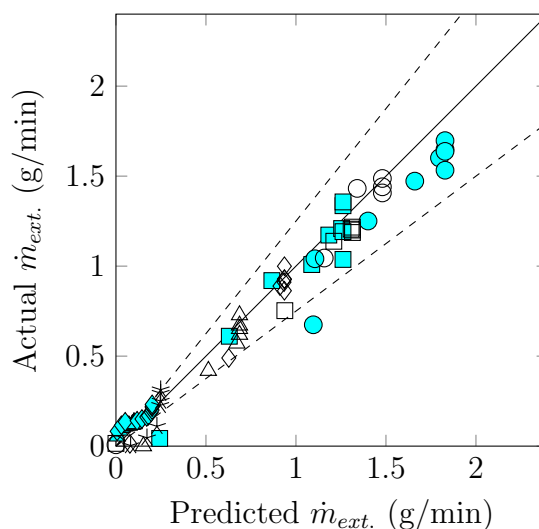


Figure 6.27: Non-dimensional two-phase permeability as a function of pressure compared to measured data with a $\pm 25\%$ error band. Symbols correspond to Table 6.9 on pg. 129.

6.4 Constraints of Generalized Models

The data presented up to this point has been limited to mass extraction measurements from a single half cycle of decreasing pressure. In all experiments, two full pressure cycles were taken to isolate the effects of cycling hysteresis found in some two-phase experiments. If there was a half cycle which was found to have inconsistent temperatures or available gas mass flow rate, it was omitted. Of the data taken, there is only one experiment where cycling hysteresis was determined to cause a permanent change in the extraction behavior. There are other cases which show temporary hysteresis but the cause of this behavior was determined to be a result of the apparatus design. In the liquid-vapor experiments, a large bubble would remain

pinned between the viewing window and the pin part of the collar holding the membrane. This bubble would provide a path for available gas to reach the excess port and avoid being extracted. For this reason, the data analyzed in the previous sections were limited to the point after a high enough pressure was reached to extract the bubble (the second half of the cycle, decreasing pressure). For this half-cycle it was determined through high speed video that the geometry did not affect the extraction rates. This is verified by the non-dimensional equations because the data showing this temporary hysteresis collapsed with the data showing no hysteresis as seen in sections 6.3.2 and 6.3.3. Sketches of the two types of cycling effects observed in the experiments here are shown in Fig. 6.28. The sketches in Fig. 6.28 are representative of all eleven raw data cases. When presenting each case of data in this section, the symbols correspond to those seen in Table 6.10.

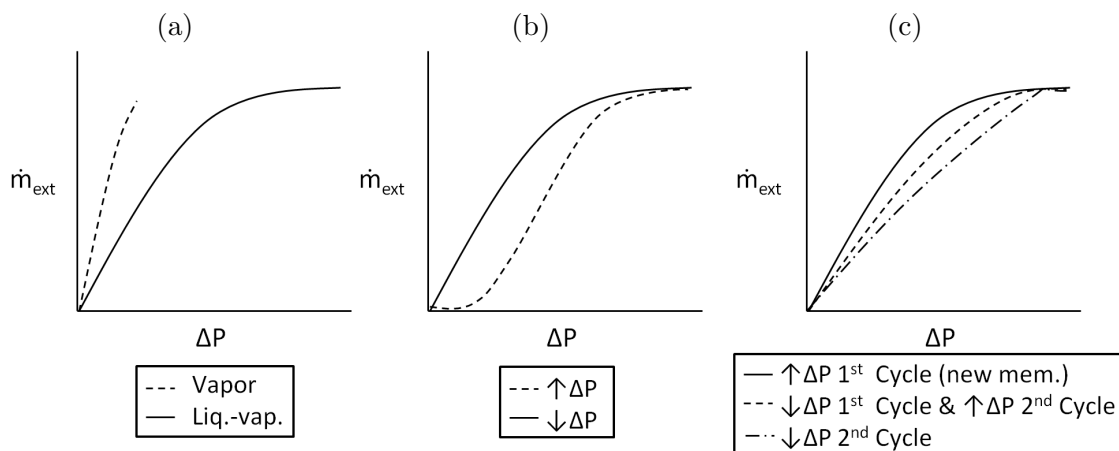


Figure 6.28: Sketches of observed cycling effects: (a) No cycling effects, bubble dynamics and reduced gas-membrane area in two-phase experiments (b) Temporary cycling effects, $\uparrow \Delta P$ cycles disregarded, determined to be caused by apparatus geometry (c) Permanent cycling effects, likely due to droplet entrapment and/or condensation.

Table 6.10: New list of symbols for cycling data.

Symbol	Description	Notes
○	↑ ΔP , New Membrane	May have been omitted due to unsteady data
□	↓ ΔP , 1 st Cycle	
◇	↑ ΔP , 2 nd Cycle	
*	↓ ΔP , 2 nd Cycle	
△	↑ ΔP , 3 rd Cycle	Where applicable
+	↓ ΔP , 3 rd Cycle	

Both of the single-phase cases do not show cycling effects as seen in Figs. 6.29a and 6.29b. This is expected as long as the nanofibers in the membrane do not break and clog the pores within the membrane. Furthermore, this shows that the membranes are not permanently deforming to the compacted state, because increases

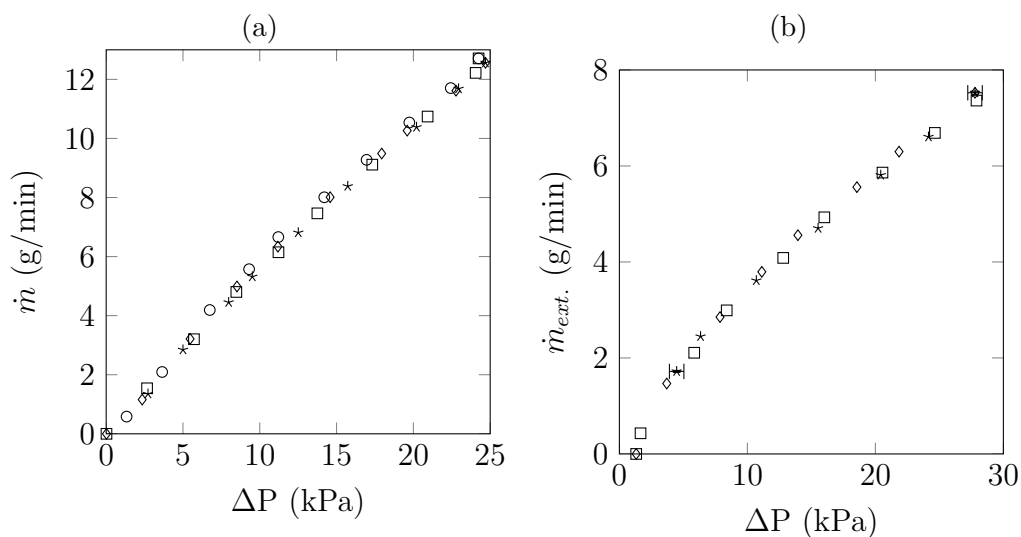


Figure 6.29: All single-phase pressure cycling data, gas extraction versus applied pressure difference. Symbols correspond to Table 6.10.

and decreases in pressure exhibit the same behavior.

The liquid-air cases are presented in Fig. 6.30a - Fig. 6.30d where the effects of hydrodynamics are present but the possibility for condensation is very unlikely,

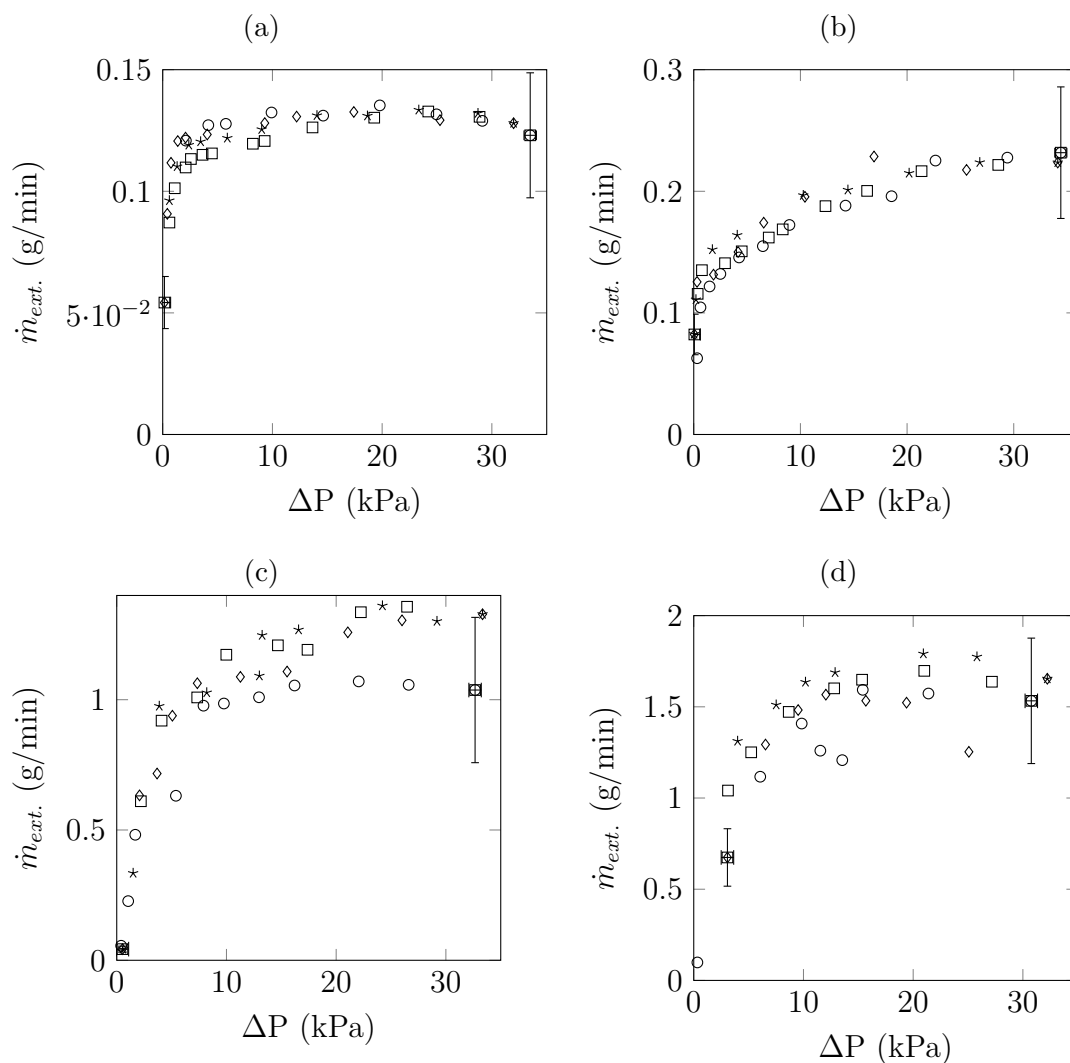


Figure 6.30: Effects of pressure cycling for all liquid-air data for the following mass flow rate of available humid air (g/min): (a) 0.13 (b) 0.26 (c) 1.67 and (d) 2.37. Symbols correspond to Table 6.10 on pg. 148.

because air is non-condensable due to the fact that it is reasonably dry. Figs. 6.30a and 6.30b are the two lowest available gas flow rate liquid-air experiments and show that all of the available air is extracted indicating full extraction is achieved.

For the two higher values of available air flow rates, Figs. 6.30c and 6.30d, the data plateaus *below* the expected value equal to the available mass flow rate of air (1.67 and 2.37 g/min respectively). This is believed to be a result of hydrodynamics and was discussed in section 6.3.1.1. One should also note that the data points scatter more in these two cases, it is possible that this is due to the fact that rotameters were used to calculate the mean extraction mass flow rates, but more likely bubble interaction was causing this to happen.

In regards to bubble interaction, the humid air cycling data shows that the hydrodynamics of more stable bubbles do not exhibit temporary hysteresis, even if it is a result of the apparatus geometry. This can be visualized in Fig. 6.17 where a bubble with high kinetic energy does not agglomerate with another bubble. In the case of the liquid-vapor however, the bubbles would likely agglomerate causing the behavior seen in Fig. 6.28b.

To further analyze the liquid-air data, the amount of water passing through the membrane can be quantified with the liquid-air data by considering the vapor mass flow rate in the extracted humid air as seen in Fig. 6.31. The measured vapor mass flow rate in the extraction line is due to four different contributions:

1. Inlet desiccant filter does not completely dry the available air
2. Water diffusion as the bubbles pass through the liquid from the bubbler to the membrane

3. Evaporation from the menisci at the pore entrances

4. Film suction in the form of droplets

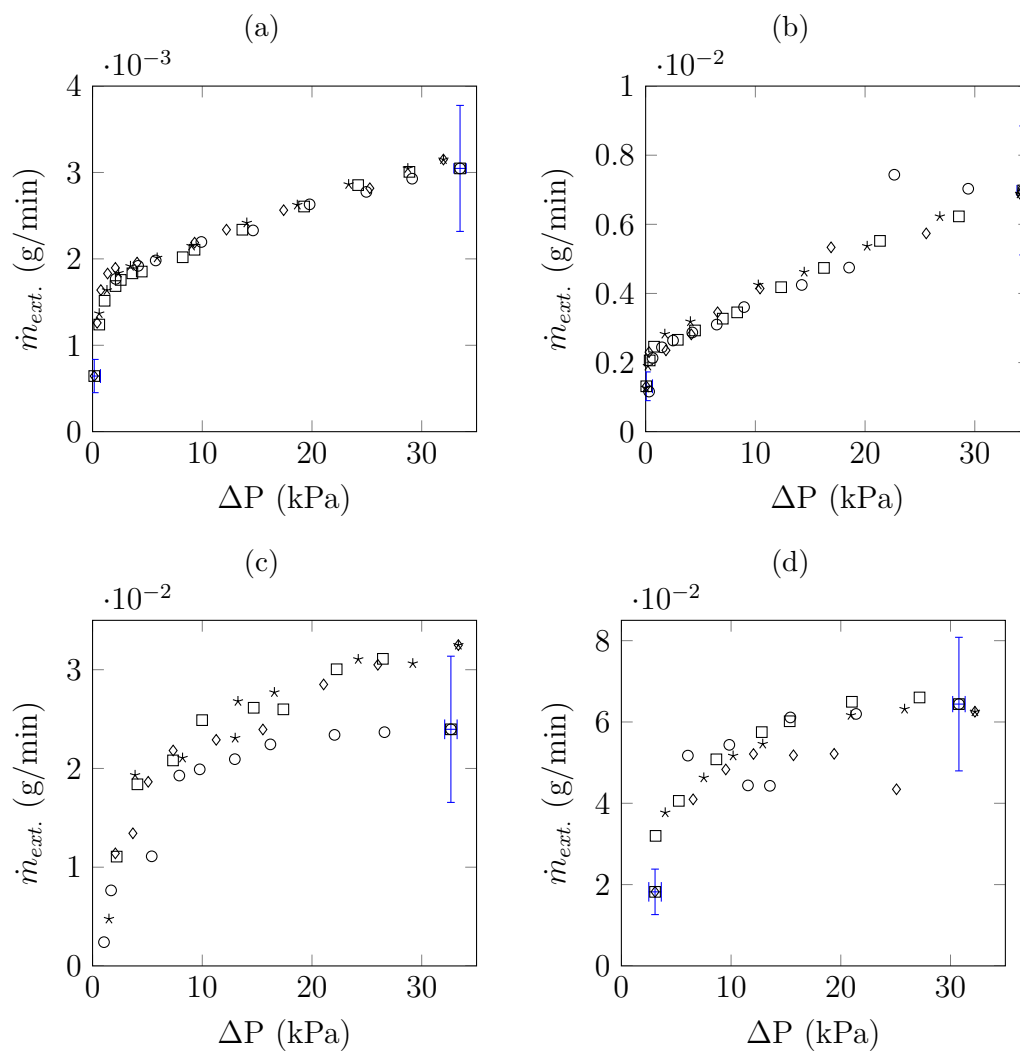


Figure 6.31: Total *water species (vapor)* in the extracted humid air minus the available vapor mass flow rate measured in the gas supply line versus applied pressure difference. Symbols correspond to Table 6.10 on pg. 148. Available humid mass flow rates of humid air are (g/min): (a) 0.13 (b) 0.26 (c) 1.67 and (d) 2.37

The humidity contribution of the available air is subtracted from the measured value in the extraction line knowing the mass flow rate of vapor in the available air line. The rapid increase in vapor content at low pressure differences is attributed to water diffusion as the bubble passes through the inlet plenum and is assumed constant at all pressures because the inlet conditions remain constant through the test. The linear increase in mass flow rate is either due to evaporation at the surface or droplets from the liquid film.

Addressing the issue of evaporation from the surface, full extraction is found to occur with a pressure difference of only 10 kPa in the 0.13 g/min case shown in Fig. 6.30a. Since the amount of extracted air remains approximately constant from 10 kPa to the maximum pressure difference, the curve of this data set plateaus. If the extracted air continued to increase to values greater than the available 0.13 g/min, it would be likely evaporation was occurring at the liquid interface. However, since there is a plateau, the effects of evaporation are not significant. This reasoning is a result of higher pressure differences resulting in an increase in mass extraction due to evaporation. The possibility that evaporation is not the only phenomena accounting for the increased humidity is fortified by considering Bandini et al. [48] study of pure water at 35°C being evaporated with VMD through a 0.2 μm PTFE nanofibrous membrane. In their study a pressure difference of ≈ 45 kPa was required to achieve measurable evaporation. At a pressure difference of 50 kPa, for the lowest liquid feed velocity it appears they are achieving $\approx 2 \times 10^{-3}$ g/min of evaporation. Since $\approx 1.5 \times 10^{-3}$ g/min of liquid can be attributed to film suction and evaporation combined at 33 kPa here, it is possible that the additional humidity is due to film suction,

especially considering the lower pressure difference.

This humidity data can help explain some of the behavior seen in the liquid-vapor cases. The liquid-vapor cycling results are presented in Fig. 6.32a - Fig. 6.32e. Like the liquid-air data, there is also some scatter, but the general trends show that the curves are still shaped in an exponential nature as was shown in the non-dimensional fits. The one case that stands out is Fig. 6.32d where a permanent increase in membrane resistance is shown to be a function of cycle number. What is peculiar about this behavior is that it is not seen in the cases with lower or higher available mass flow rates. This is believed to be due to droplet entrapment combined with condensation. One notable difference between the data case with possible droplet entrapment and the ones without is that the quality is at least twice as high and therefore the flow regime is more foamy than annular or bubbly.

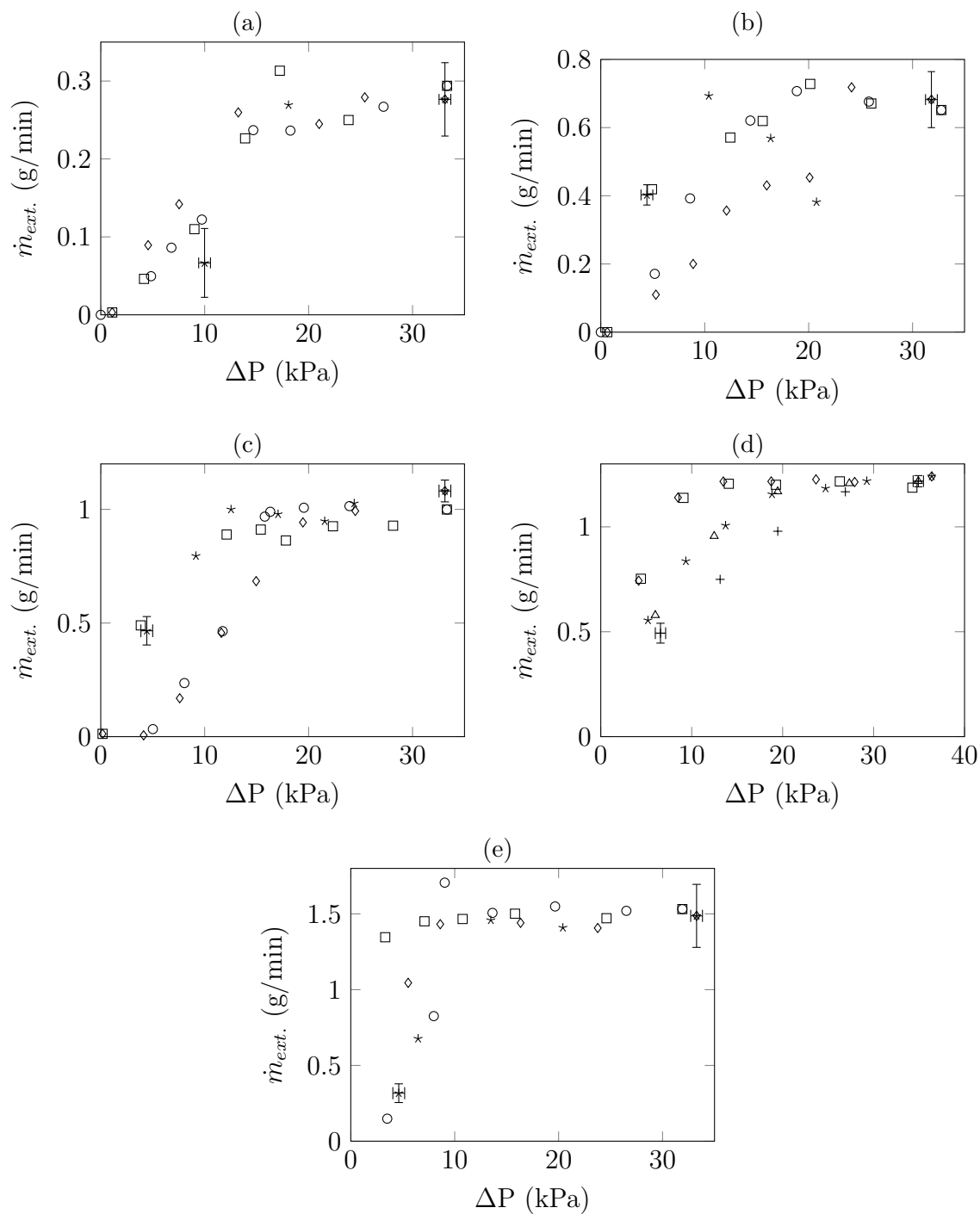


Figure 6.32: All liquid-vapor pressure cycling data, gas extraction versus applied pressure difference for the following mass flow rate of available vapor (g/min): (a) 0.26 (b) 0.72 (c) 0.98 (d) 1.38 and (e) 1.55. Symbols correspond to Table 6.10 on pg. 148.

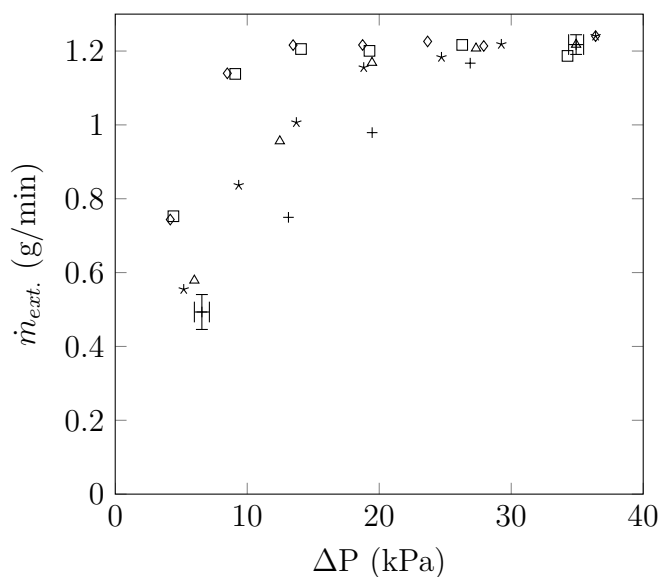


Figure 6.33: 1.38 g/min available vapor cycling reproduced

To explain the unexpected behavior of the 1.38 g/min liquid-vapor case in Fig. 6.32d, some ideas are presented here. The case of interest is reproduced in Fig. 6.33. Increased membrane resistance over time is typically attributed to fouling. Fouling of membranes is very unlikely within the time span of these tests (4-5 hours), especially when considering the fact that the distilled water is filtered with pores smaller than the membrane's pores. Furthermore, as was mentioned earlier PTFE is known to be very resistant to fouling.

Judging by the overlay of data for the second half of each cycle (\square , \star , $+$) and the first half of the next (\diamond , \triangle) with a drastic decrease in flow rate for the next half-cycle, fouling is not likely. Fouling would show a consistent decrease in extracted vapor as time goes on.

It is also known that water can build up on the support side of the membrane.

David et al. [32] passively vented vapor from a two-phase saturated mixture and blew air through the extraction chamber to manage the water and found that this technique helped remove droplets on the membrane support. In the tests here, the NiCr heater coils kept the extraction chamber at 120°C as seen in the table of case summaries, Table 4.2.

When considering the possibility for these trends to be a result of hydrodynamic behavior, the data can not be described as a temporary effect due to bubble pinning as seen the 0.98 g/min liquid-vapor case Fig. 6.32c. Also, if bubble behavior or liquid film rupturing was varying from one cycle to the next, the plateau would not be reached. Examples of the hydrodynamics preventing full extraction were seen in the 1.67 and 2.37 g/min cases of liquid-air Figs. 6.30c and 6.30d.

The most likely reason why the resistance is increasing is due to increased hydraulic dispersion where vapor particles lose more momentum due to pore blockage as discussed by Liu and Masliyah [33]. Hydraulic dispersion is known to only occur in porous media where the pores are interconnected like the pores in the PTFE membrane studied here (Fig. 4.2). Furthermore dispersion is not just a function of the porosity and geometry of the pores; it is possible for fluid phases to introduce dispersion as has been found in the case of trapped air bubbles in hydrophilic porous media [33]. In the case of the system here, it is known that water is evaporating at the liquid-membrane interface as it does in VMD because of the applied pressure difference which results in diffusion. In addition to the evaporation from the menisci at the pore entrances, it is also likely that when the thin liquid film ruptures to form TCP, it does not merely recede as is found in film rupture below solid walls as studied

by Redon et al. [47]. The combination of the pressure difference and the thinning film likely results in small droplets being pulled into the membrane. It is known that the film ruptures due to wave instabilities where the low amplitude regions of the waves result in a thin layer of liquid and are more likely to initiate the rupture [35]. Films typically rupture at 0.04-0.06 μm without the aid of extraction [35]. Assuming the same film rupture dynamics exist in a system with extraction (a conservative assumption), the thickness of the films upon rupture are about a tenth the 0.45 μm pore diameter which makes it possible that before the films thin to this point, the pressure at the membrane pore is great enough to disturb the film. When the film prematurely ruptures due to the applied pressure difference, it is possible droplets form which could either fall down through the bubble into the plenum or get pulled into the membrane. The droplets that get pulled into the membrane could get trapped in deeper layers of the membrane. As was approximated earlier, there are about 35 layers of pores assuming each layer is the thickness of the mean pore diameter.

Assuming droplets are getting pulled into the membrane, the major difference between the liquid-air and liquid-vapor cases is that the air is very dry and can therefore absorb water vapor. Since the droplets are so small, it is likely they will evaporate readily as the air passes by the droplets trapped in the membrane. When considering the liquid-vapor case however, the membrane is likely at saturation because it is in contact with the saturated pool of water. Even though the temperature in the membrane is at saturation, the mere passing of vapor does not provide energy to overcome the heat of vaporization for the droplet to change phases. The reason why the energy associated with the pressure drop at the membrane does not apply here

is because the pores are interconnected and the droplet is assumed to be at least one layer deep in the membrane allowing the pressure to equilibrate around the drop. If this explanation holds true, the droplets will remain trapped in the membrane until energy is available to overcome the heat of vaporization.

One possible reason why the extraction rate decreases on the decreasing pressure cycles is because when the pressure *difference* is decreased, the *absolute* extraction pressure is increased. With an increase in absolute pressure, the saturation temperature increases and therefore vapor is likely to condense on the trapped droplets increasing their size upon a decrease in pressure difference. Once the PTFE forming the membrane has enough time to get up to saturation temperature by convection of the passing vapor, the vapor passing by the droplet stops condensing. Given the right conditions, this cycling process appears to result in a decreased porosity which is limiting the extraction rates as is seen in Fig. 6.33.

In regards to the reason why the 0.98 and 1.55 g/min cases do not exhibit the same behavior, with the data here can only be attributed to the difference in quality. The quality of the 1.38 g/min case is 32% compared to 10% and 15% for the 0.98 and 1.55 g/min cases respectively (see Table 4.2). The higher quality is believed to have two effects on the bubbles. First, less liquid is in the inlet plenum which would result in more of a foamy flow and therefore thinner liquid interfaces may exist between bubbles. Second, the boiling process will be more vigorous and therefore bubble departures will be more frequent resulting in higher bubble velocities. The combination of these two effects could result in thinner films being ruptured at the membrane, resulting in smaller droplets which are more likely to get sucked into the

membrane.

One possible reason why the higher pressure differences do not show a significant decrease in mass transport is that for a higher flow rate, the droplets will have higher inertia and may be able to pass through the membrane. At lower mass flow rates through the membrane (lower pressure differences), the membrane is thicker because it is not compacted as much, and therefore the drops take longer to pass through and can accumulate more volume. More data would need to be taken at qualities greater than 30% to verify this, but the data have been deemed accurate due to the fact that two half-cycles overlay each other and the next two mimic this behavior but at a lower extraction rate.

6.4.1 Summary of Non-dimensional Models

Referring to the summary of the traditional versus compaction-corrected models without area corrections, Table 6.11, the compaction corrections reduce the average MAE for both the DGM and Darcy's Law. The MAE values are only accounting for the error between the model predictions and the measured data for data points in the partial extraction region, or in other words, at extraction rates lower than the available gas plateau. If measured data points had pressure differences less than 0.5 kPa, these data points were not considered, because the MAE was artificially high due to a measured extraction rate near zero (see the MAE equation, Eq. (D.12)). Cells which do not have values indicate that even at the next lowest pressure difference beyond 0.5 kPa, the predicted gas extraction rate was greater than the available gas

Table 6.11: MAE of extraction predictions comparing the effects of compaction with no reduced area. MAE percent values are in bold, are *only representative of data in the partial extraction region* and exclude data points with measured pressure differences less than 0.5 kPa.

		\dot{m}_{avail} (g/min)									
		Liquid-Vapor					Liquid-Air				
Model	Compaction	0.26	0.72	0.98	1.38	1.55	0.13	0.26	1.63	2.37	Avg.
DGM	No	299	166	98	79		154	81	97		139
	Yes	287	160	93	73		154	80	95		135
Darcy	No	72		83	48		92	99	86		80
	Yes	72		50	48		92	93	82		73

plateau. If this is the case, there is no data available to calculate the MAE in the partial extraction region.

Referring to the summary of the non-dimensional compaction- and area-corrected models, Table 6.12, the extraction data are well predicted with the lowest average MAE of 11% and 8% for Darcy’s Law and the DGM, respectively. The higher error in the low available flow rate data is due to the fact that these curves were typically not included in the non-dimensional curve fits, but also a slight deviation in the predicted flow rate will result in a large error. The MAE values are averaged excluding the lowest available flow rate cases to be consistent with the single-phase averages of Table 6.11. The MAE of the best compaction- and area-corrected DGM and Darcy’s Law predictions are reduced by 94% and 86% compared to the traditional DGM and Darcy’s Law, respectively.

When considering the MAE influenced by both partial and full extraction regions, the most accurate model is the two-phase permeability model as shown in Table 6.13.

Table 6.12: MAE of non-dimensional extraction predictions accounting for compaction and reduced area. MAE percent values are in bold, are *only representative of data in the partial extraction region* and exclude data points with measured pressure differences less than 0.5 kPa. Non-dimensional area correction models are in the Φ_m^* column.

Model	Φ_m^*	\dot{m}_{avail} (g/min)									
		Liquid-Vapor					Liquid-Air				
		0.26	0.72	0.98	1.38	1.55	0.13	0.26	1.63	2.37	Avg. ^a
DGM	α_{AA}	511	122	67	53	13	48	46	32	36	53
	Eq. (6.6)	67	21	22	30	30	30	53	34	36	32
	Eq. (6.7)	629	48	31	30	12	20	32	12	11	25
	Eq. (6.8)	143	21	19	147	11	40	13	12	8	33
	Eq. (6.9)	113	7	12	7	9	41	15	5	4	8
Darcy	α_{AA}	464	72		33	13	31	50	30	32	38
	Eq. (6.10)	62	10		11	20	48	43	15	29	21
	Eq. (6.11)	39	6	8	5	8	52	33	8	9	11

^a Not including L-V 0.26 g/min or L-A 0.13 g/min cases for consistency with single-phase

However, the DGM non-dimensionalized by Eq. (6.9) provides an average MAE close to that of the permeability model. The reason why the average MAE values in Table 6.13 have lower average values than in Table 6.11 is because the plateau is reached, and since there are numerous points at the plateau, this influences the MAE significantly. The main purpose of the area-corrected models is to better predict the transition from partial to full extraction, which is best achieved by Eq. (6.11) and Eq. (6.9).

The data compiled in Table 6.13 considers all data points other than those with pressure differences less than 1.5 kPa. This is different than the criteria of the values in the partial extraction MAE table, Table 6.12, because the 0.26 g/min liquid-vapor

Table 6.13: MAE of non-dimensional extraction predictions accounting for compaction and reduced area. MAE percent values are in bold, are *representative of data in the partial and full extraction regions* and exclude data points with measured pressure differences less than 1.5 kPa. Non-dimensional area correction models are in the Φ_m^* column.

		\dot{m}_{avail} (g/min)									
		Liquid-Vapor					Liquid-Air				
Model	Φ_m^*	0.26	0.72	0.98	1.38	1.55	0.13	0.26	1.63	2.37	Avg.
DGM	α_{AA}	108	20	10	19	7	18	30	32	38	31
	Eq. (6.6)	37	13	13	15	19	9	30	28	38	22
	Eq. (6.7)	108	22	14	12	18	14	18	20	19	27
	Eq. (6.8)	79	11	11	27	12	34	8	14	8	23
	Eq. (6.9)	68	9	11	5	9	35	9	7	6	18
Darcy	α_{AA}	108	22	21	21	10	12	34	34	41	33
	Eq. (6.10)	63	21	21	18	24	24	13	18	26	25
	Eq. (6.11)	30	7	10	4	8	47	30	10	7	17

case has high MAE values at pressure differences below 1.5 kPa. A similar table quantifying the MAE of all data for the single-phase cases is not presented, because nearly all models and data cases predict full extraction at pressure differences greater than 1.5 kPa.

A summary of the compaction- and area-corrected models considered is listed in Table 6.14. The top row of each base model section was presented in section 6.2 and assumes the area can be corrected by the void fraction.

In regards to the results validation, Alexander and Wang [7] conducted a similar study with water-air mixtures for larger pores and a lower pressure difference and used an exponential fit to determine empirical coefficients, but their model is not comparable because it is specifically for microchannels. Aside from the model de-

Table 6.14: Summary of non-dimensional area corrections for the DGM and Darcy's Law.

Base Model	Exponential Fit				Non-Dimensional Area Correction	
	Form	χ	C	n	Φ_m^*	Case-specific Variable
DGM	N/A	N/A	N/A	N/A	α_{AA}	
	Eq. (6.4)	α_{AA}	1.7×10^6	-4	Eq. (6.6)	
	Eq. (6.4)	ΔP	7	0.4	Eq. (6.7)	α_{AA}
	Eq. (6.5)	ΔP	9×10^{11}	0.36	Eq. (6.8)	x
	Eq. (6.4)	ΔP	2.8×10^{-3}	0.34	Eq. (6.9)	\dot{m}_{avail}
Darcy	N/A	N/A	N/A	N/A	α_{AA}	
	Eq. (6.4)	ΔP	4.1	9×10^{-2}	Eq. (6.10)	\dot{m}_{avail}
	Eq. (6.5)	ΔP	2.7×10^{-3}	0.32	Eq. (6.11)	\bar{K}_{lg} and \dot{m}_{avail}

velopment, it was found that permeability increases slightly as the applied pressure difference is increased for single-phase air and a membrane porosity of 55%. This is inconsistent with Lawson et al. theoretical predictions [30] but the change in permeability here is small. The empirical compaction coefficient is compared to Lawson et al. [30] study, but their membrane was constructed of a different material and had different properties so the verification is limited.

6.4.2 Recommended Models

The best fit model in the partial extraction region for both liquid-air and liquid-vapor mixtures is the modified DGM, Eq. (6.9), but when considering both partial and full extraction regions, the modified Darcy's Law, Eq. (6.11), provides the best fit. It is recommended to use the modified DGM, Eq. (6.9), for extraction predictions

because it contains more physical meaning and therefore is more applicable to a variety of systems. The applicability of the modified models developed here have only been verified for a range of available gas flow rates and for two mixtures. When applying the modified models to predict extraction rates from liquid-gas mixtures, the user must be aware of the model constraints as described in section 6.4.

The accuracy of the models is specific to the geometry of the experimental apparatuses. Due to the high void fractions, bubbles are prone to agglomeration, so the distance between the bubble origin (boiling surface or air bubbler) and the extraction surface could lead to differences in extraction predictions. Furthermore, the ratio of the membrane area to the total area of the wall which the membrane sits on should not be overlooked, because a smaller extraction area will result in less membrane-bubble contact. The extent to which extraction rates will be limited was not studied here, but the membrane area covered 69% of the top wall and all of the available vapor was extracted in the liquid-vapor studies. Therefore, if more than 69% of the wall where the membrane sits is available for single-phase gas transport, then the system would presumably perform similarly.

When employing the best fit modified DGM or Darcy's Law, the non-dimensional equations summarized in Table 6.14 must be rearranged to isolate the area correction, Φ_m . To explain this, applying of the best fit modified Darcy's Law, Eq. (6.11), is presented. With this model, the average permeability of the gas being extracted is needed. If the experimental flow rate is measured as a function of the pressure difference across the membrane, an approach like that in section 6.1.1 can be used to find the average permeability. The flow rate can also be predicted as a function of the

pressure difference using the DGM, Eq. (2.19) and Eq. (5.20), where the compaction coefficient is a function of the average temperature in the membrane as estimated by Eq. (6.1). This flow rate and the corresponding pressure differences will provide data to determine the permeability. If air or vapor is being extracted, the single-phase Darcy permeabilities in Table 6.3 can be scaled by the dynamic viscosity at the operating temperature of interest to estimate the average single-phase permeability.

The non-dimensional liquid-gas permeability Eq. (6.11) is rearranged to calculate the dimensional permeability

$$K_{D,lg} = \bar{K}_{D,g} \frac{1}{-\cos\theta} \frac{\dot{m}_{avail}}{\mu_g} \sqrt{\frac{g(\rho_l - \rho_g)}{\sigma_{lg}}} \text{Cexp}(-\Delta P^n) \quad (6.12)$$

This pressure-dependent permeability is substituted into Darcy's Law Eq. (2.9) with a constant membrane area equal to that to the single-phase tests and the non-compacted membrane thickness

$$\dot{m}_D = \frac{K_{D,lg} A_{mem} \Delta P \rho}{\delta_o \mu} \quad (6.13)$$

Applying Eq. (6.13) where the two-phase permeability is defined by Eq. (6.12) results in the curves shown in Fig. 6.34a. These curves need to be modified to properly show full extraction, as defined by a plateau equal to the maximum extraction rate predicted, as seen in Fig. 6.34b. The plateau is always limited by the maximum predicted extraction rate in this example, but the predictions should also be limited by the available gas flow rate when a maximum is not reached as seen in the 1.38 g/min case (the dash-dot line) of Fig. 6.21b.

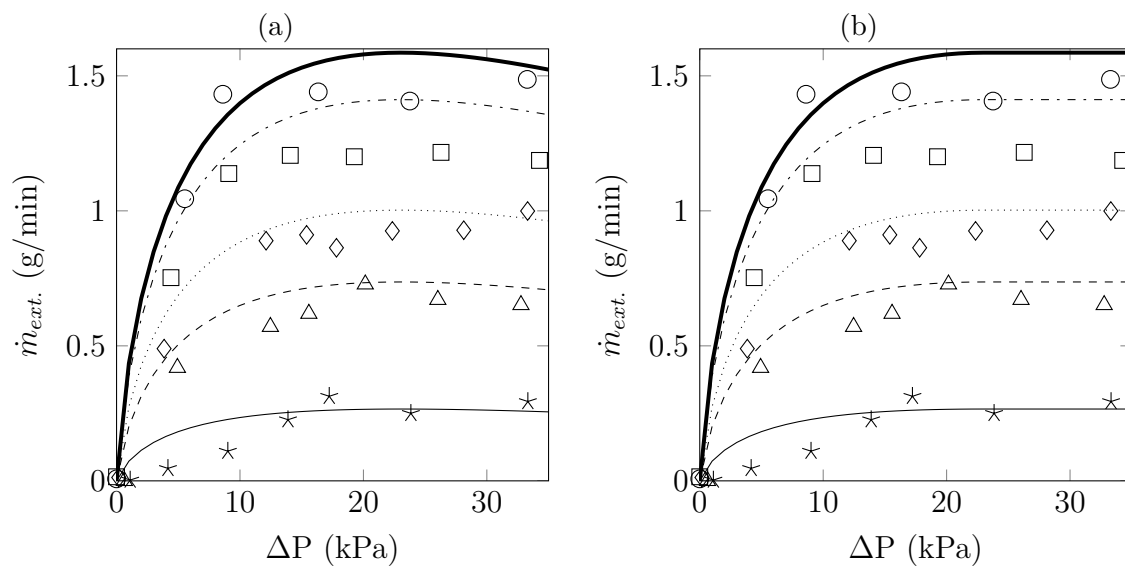


Figure 6.34: Darcy's Law extraction predictions using Eq. (6.12) showing the impact of (a) omitting and (b) including the full extraction criteria as defined by the maximum extraction rate in (a) or the available gas flow rate, whichever is lower.

Chapter 7 – Conclusions

This study focused on the characteristics of microporous inter-connected pore membranes while extracting gas from two-phase fluid mixtures. Both water-air and water-vapor mixtures were evaluated. A range of experimental conditions were achieved by varying the applied pressure differential across the membrane and the two-phase void fraction in the pool. The general trend of the studies was an increase in mass extraction rates for an increase in applied pressure difference until a maximum extraction rate equal to or less than the available gas flow rate was reached. Gas extraction from two-phase mixtures has been found to be a complex process dependent on many parameters, including both membrane and fluid properties. Consequently, repeatable performance may be difficult to achieve.

A number of variations to two existing porous media gas transport models have been developed to predict extraction flow rates of gas extracted from bubbly-annular liquid pools. These variations are based on the dusty gas model (DGM) and Darcy's Law, where the membrane thickness and extraction area are modified to be pressure-dependent. Membrane compaction is pressure-dependent due to the resulting force and the membrane's high porosity and polymer construction. PTFE membranes are less rigid at elevated temperatures, and therefore the thickness decreases more rapidly than at lower temperatures. The extraction area decreases with increasing pressure difference, because bubbles are extracted at a greater rate; in other words, for the same

volume flow rate, less area is required if the driving potential increases. Furthermore, the three phase contact dynamics (bubble necking, film rupture) change which makes the area correction term partially dependent on hydrodynamic time constants.

The compaction- and area-corrected models presented require knowledge of the available gas flow rate. Knowing this, the extraction flow rate as a function of pressure difference across the membrane can be estimated. Scaling of the resultant models was performed to arrive at a non-dimensional form. The models were scaled by variables describing the physics of the mixture at or near the membrane interface. These physics include surface tension forces, capillary forces, buoyant forces, viscous forces and proper length scales in select model variations. The most accurate model in the partial extraction region is the DGM with an MAE of 8%, however when considering both the partial and full extraction regions, the MAE increases to 18%. An alternative model based on Darcy's Law is slightly more accurate over both regions with an MAE of 17%, but requires knowledge of the single-phase permeability of the gas being extracted. The DGM is recommended in spite of the overall accuracy of the modified Darcy's Law, because it provides better insight into the physical factors influencing gas transport and is therefore more universal.

Bubble dynamics were studied using high speed video images and compared to three phase contact studies (TPC) of bubbles approaching a rough hydrophobic solid. Based on these observations, the extraction process appears to rupture thin films, and therefore, TPC is enhanced by extraction. The liquid-air apparatus design resulted in greater bubble kinetic energy than in the liquid-vapor apparatus, so the air bubbles tended to bounce off the membrane. Repeated collisions between each bubble and

the membrane were found to be necessary to dissipate enough energy and begin extraction. Consequently, extraction rates may be influenced by the hydrodynamic flow conditions of bubbles in contact with the membrane.

Cycling the pressure difference across the membrane was found to result in non-repeatable vapor extraction rates when the quality in the pool was 32%, however for qualities below 15% extraction rates were repeatable. The gas flow resistance of the membrane increased each time the pressure difference was decreased, but was unaffected for an increase in pressure difference.

Chapter 8 – Recommendations

There are a number of complex phenomena associated with gas extraction from two-phase mixtures which should be further investigated for a better understanding of the extraction process. To make the models presented here more robust, liquid-vapor qualities greater than 15% should be studied to better understand how pressure cycling increases resistance. The range of parameters should also be expanded to include the effects of inlet plenum geometry and membrane variations including pore size and hydrophobicity. The models developed here are evaluated at the average pressure and temperature between the inlet and extraction plenum, but the temperature or pressure of one plenum may be more influential on the average state properties in the membrane. A CFD study of the average temperature and pressure in the membrane would be useful, because it very well may be that temperatures are closer to the saturation temperature through the thickness of the membrane. Furthermore, the presence of a liquid in contact with the membrane may be found to influence the average temperature in the membrane more than the gas in the extraction chamber i.e. merely averaging the inlet and extraction temperatures could be an inaccurate prediction of the average gas temperature.

The bubble dynamics could be studied more quantitatively if individual bubbles were extracted and if their velocity were varied. Single bubble tests would lead to a better understanding in the film rupture and three phase contact behavior with an

applied pressure difference across the membrane. It would also be useful to study the extraction of a bubble which has not departed from the wall, because this replicates some end-use applications like micro-scale heat transfer.

In regards to further studying droplet entrapment and/or condensation, an environmental scanning electron microscope (ESEM) could possibly be used to look at a cross-section of a membrane which underwent increased flow resistance, but it would be difficult to cut the membrane without evaporating the droplets. Other methods of detecting any liquid droplet distribution should be looked into as this phenomena would be nearly unavoidable if high qualities are confirmed to result in increased flow resistance.

To reduce the number of variables and possibly eliminate issues associated with condensation and droplet entrapment, a rigid membrane with straight-through pores could be used. Alexander and Wang [7] used a rigid silicon membrane hydrophobized with a silane, but noted that the surface coating gave them issues. The robustness of solid hydrophobic membranes needs to be further studied, but Tasaltin et al. [49] were able to successfully coat an anodic alumina oxide (AAO) membrane with a silane. This resulted in a rigid, superhydrophobic surface with straight-through pores and high porosity. This would be ideal for an application such as gas separation in heat transfer studies if the silane did not wash off. Tasaltin et al. [49] anodized their own membranes from pure aluminum, but Synkera (CO, USA) and Whatman/GE (NY, USA) supply membranes which appear to be analogous to the one manufactured by Tasaltin et al. [49]. An in-house study was conducted at Oregon State University (OSU) by the same author of this thesis using Whatman's 0.150 μm pore diameter,

50 μm thick AAO membranes with hexamethyldisilazane (HMDS). This is the same silane used by Tasaltin et al. [49], but in their work, flow rates through the membrane were not analyzed. When the AAO samples were studied at OSU, they were fracturing as a result of handling, so results are limited. However, a contact angle of $\theta = 107 \pm 13^\circ$ was achieved.

Bibliography

- [1] Fang, C., David, M., Rogacs, A., and Goodson, K., 2010. “Volume of fluid simulation of boiling two-phase flow in a vapor-venting microchannel”. *Frontiers in Heat and Mass Transfer*, **1**(1), p. 111.
- [2] David, M. P., Miler, J., Steinbrenner, J. E., Yang, Y., Touzelbaev, M., and Goodson, K. E., 2011. “Hydraulic and thermal characteristics of a vapor venting two-phase microchannel heat exchanger”. *International Journal of Heat and Mass Transfer*, **54**(25), pp. 5504–5516.
- [3] Meng, D. D., Kim, J., and Kim, C.-J., 2006. “A degassing plate with hydrophobic bubble capture and distributed venting for microfluidic devices”. *Journal for Micromechanics and Microengineering*, **16**, pp. 419–424.
- [4] Apreotesi, M. A., 2007. “Microscale thermal management utilizing vapor extraction from a fractal-like branching heat sink”.
- [5] Mudawar, I., 2001. “Assessment of high-heat-flux thermal management schemes”. *Components and Packaging Technologies, IEEE Transactions on*, **24**(2), pp. 122–141.
- [6] Salakij, S., 2013. “Modeling in-situ vapor extraction during flow boiling in microscale channel”. Graduation date: 2013.
- [7] Alexander, B. R., and Wang, E. N., 2009. “Design of a microbreather for two-phase microchannel heat sinks”. *Nanoscale and Microscale Thermophysical Engineering*, **13**(3), pp. 151–164.
- [8] Gibson, P., Schreuder-Gibson, H., and Rivin, D., 2001. “Transport properties of porous membranes based on electrospun nanofibers”. *Colloids and Surfaces A: Physicochemical and Engineering Aspects*, **187**, p. 469481.
- [9] Khayet, M., 2011. “Membranes and theoretical modeling of membrane distillation: A review”. *Advances in Colloid and Interface Science*, **164**(12), May, pp. 56–88.

- [10] Lawson, K. W., and Lloyd, D. R., 1997. “Membrane distillation”. *Journal of membrane Science*, **124**(1), pp. 1–25.
- [11] El-Bourawi, M. S., Ding, Z., Ma, R., and Khayet, M., 2006. “A framework for better understanding membrane distillation separation process”. *Journal of Membrane Science*, **285**(1), p. 429.
- [12] Peña, L., de Zárata, J. M. O., and Mengual, J. I., 1993. “Steady states in membrane distillation: influence of membrane wetting”. *Journal of the Chemical Society, Faraday Transactions*, **89**(24), pp. 4333–4338.
- [13] Persson, K. M., Gekas, V., and Trägårdh, G., 1995. “Study of membrane compaction and its influence on ultrafiltration water permeability”. *Journal of membrane science*, **100**(2), pp. 155–162.
- [14] Lawson, K. W., and Lloyd, D. R., 1996. “Membrane distillation. i. module design and performance evaluation using vacuum membrane distillation”. *Journal of membrane science*, **120**(1), pp. 111–121.
- [15] Khayet, M., Feng, C. Y., Khulbe, K. C., and Matsuura, T., 2002. “Preparation and characterization of polyvinylidene fluoride hollow fiber membranes for ultrafiltration”. *Polymer*, **43**(14), pp. 3879–3890.
- [16] Martinez, L., Florido-Diaz, F. J., Hernandez, A., and Pradanos, P., 2002. “Characterisation of three hydrophobic porous membranes used in membrane distillation: modelling and evaluation of their water vapour permeabilities”. *Journal of membrane science*, **203**(1), p. 1527.
- [17] Khayet, M., Khulbe, K. C., and Matsuura, T., 2004. “Characterization of membranes for membrane distillation by atomic force microscopy and estimation of their water vapor transfer coefficients in vacuum membrane distillation process”. *Journal of membrane science*, **238**(1), pp. 199–211.
- [18] Adnan, S., Hoang, M., Wang, H., and Xie, Z., 2011. “Commercial PTFE membranes for membrane distillation application: Effect of microstructure and support material”. *Desalination*.
- [19] Darcy, H., 1856. *Les fontaines publiques de la ville de Dijon*. V. Dalmont.
- [20] Xu, J., Vaillant, R., and Attinger, D., 2010. “Use of a porous membrane for gas bubble removal in microfluidic channels: physical mechanisms and design criteria”. *Microfluidics and nanofluidics*, **9**(4), pp. 765–772.

- [21] He, X., 2013. “CFD simulation of single-phase and flow boiling in confined jet impingement with in-situ vapor extraction using two kinds of multiphase models”. PhD thesis, Jan. Graduation date: 2013.
- [22] David, M. P., Steinbrenner, J. E., Miler, J., and Goodson, K. E., 2011. “Adiabatic and diabatic two-phase venting flow in a microchannel”. *International Journal of Multiphase Flow*, **37**(9), pp. 1135–1146.
- [23] Meng, D. D., Cubaud, T., Ho, C.-M., and Kim, C.-J., 2007. “A methanol-tolerant gas-venting microchannel for a microdirect methanol fuel cell”. *Microelectromechanical Systems, Journal of*, **16**(6), pp. 1403–1410.
- [24] Carey, V., 2007. *Liquid Vapor Phase Change Phenomena*, 2 ed. Taylor & Francis, Nov.
- [25] De Gennes, P.-G., Brochard-Wyart, F., and Qur, D., 2003. *Capillarity and wetting phenomena: drops, bubbles, pearls, waves*. Springer.
- [26] Vargaftik, N., Volkov, B., and Voljak, L., 1983. “International tables of the surface tension of water”. *J. Phys.Chem. Ref. Data*, **12**(3).
- [27] Sarti, G. C., Gostoli, C., and Matulli, S., 1985. “Low energy cost desalination processes using hydrophobic membranes”. *Desalination*, **56**, pp. 277–286.
- [28] Marconnet, A. M., David, M. P., Rogacs, A., Flynn, R. D., and Goodson, K. E., 2008. “Temperature-dependent permeability of microporous membranes for vapor venting heat exchangers”. *Heat Transfer, Fluid Flows, and Thermal Systems, Parts A, B, and CASME*, pp. 1005–1012.
- [29] Saffarini, R. B., Mansoor, B., Thomas, R., and Arafat, H. A., 2013. “Effect of temperature-dependent microstructure evolution on pore wetting in PTFE membranes under membrane distillation conditions”. *Journal of Membrane Science*, **429**, Feb., pp. 282–294.
- [30] Lawson, K. W., Hall, M. S., and Lloyd, D. R., 1995. “Compaction of microporous membranes used in membrane distillation. i. effect on gas permeability”. *Journal of Membrane Science*, **101**(12), May, pp. 99–108.
- [31] Zhang, J., Li, J. D., and Gray, S., 2011. “Effect of applied pressure on performance of PTFE membrane in DCMD”. *Journal of Membrane Science*, **369**(1), pp. 514–525.

- [32] David, M. P., Marconnet, A., and Goodson, K. E., 2008. “Hydrodynamic and thermal performance of a vapor-venting microchannel copper heat exchanger”.
- [33] Liu, S., and Jacob, H. M., 1996. “Single fluid flow in porous media”. *Chemical Engineering Communications*, **148**(1), pp. 653–732.
- [34] Haynes, W. M., 2010. *CRC Handbook of Chemistry and Physics, 91st Edition*. Taylor & Francis Group, June.
- [35] Radoev, B., Stöckelhuber, K. W., Tsekov, R., and Letocart, P., 2007. “Wetting film dynamics and stability”. *Colloids Interface Sci. Ser. 3*.
- [36] Schulze, H. J., Stöckelhuber, K. W., and Wenger, A., 2001. “The influence of acting forces on the rupture mechanism of wetting films nucleation or capillary waves”. *Colloids and Surfaces A: Physicochemical and Engineering Aspects*, **192**(1), p. 6172.
- [37] Krasowska, M., Krastev, R., Rogalski, M., and Malysa, K., 2007. “Air-facilitated three-phase contact formation at hydrophobic solid surfaces under dynamic conditions”. *Langmuir*, **23**(2), Jan., pp. 549–557.
- [38] Bandini, S., Gostoli, C., and Sarti, G. C., 1992. “Separation efficiency in vacuum membrane distillation”. *Journal of Membrane Science*, **73**(2), pp. 217–229.
- [39] Sabo, M. D., 2012. “Performance and flow stability characteristics in two-phase confined impinging jets”.
- [40] White, F. M., 2008. *Fluid Mechanics*. McGraw-Hill Higher Education.
- [41] Laganá, F., Barbieri, G., and Drioli, E., 2000. “Direct contact membrane distillation: modelling and concentration experiments”. *Journal of Membrane science*, **166**(1), pp. 1–11.
- [42] Hetsroni, G., 1982. “Handbook of multiphase systems”.
- [43] Chisholm, D., 1983. *Two-phase flow in pipelines and heat exchangers*. G. Godwin.
- [44] NTeWORKS. PicPick.
- [45] Brown, D. Tracker.

- [46] Skiljan, I. IrfanView.
- [47] Redon, C., Brochard-Wyart, F., and Rondelez, F., 1991. “Dynamics of dewetting”. *Physical review letters*, **66**(6), pp. 715–718.
- [48] Bandini, S., Saavedra, A., and Sarti, G. C., 1997. “Vacuum membrane distillation: experiments and modeling”. *AIChE journal*, **43**(2), pp. 398–408.
- [49] Tasaltin, N., Sanli, D., Jonávs, A., Kiraz, A., and Erkey, C., 2011. “Preparation and characterization of superhydrophobic surfaces based on hexamethyldisilazane-modified nanoporous alumina”. *Nanoscale research letters*, **6**(1), p. 18.
- [50] Purinton, N., and Filter, S., 1992. Gore-tex: An introduction to the material and treatments. <http://cool.conservation-us.org/coolaic/sg/bpg/annual/v11/bp11-33.html>.
- [51] Willmott, C. J., and Matsuura, K., 2005. “Advantages of the mean absolute error (MAE) over the root mean square error (RMSE) in assessing average model performance”. *Climate Research*, **30**(1), p. 79.

APPENDICES

Appendix A – Laplace Equation

As described in section 2.2.1, the Laplace equation can be used to estimate the liquid entry pressure (LEP) of a hydrophobic pore with a known pore radius. The Laplace equation can be defined from both a mechanics and a thermodynamic perspective. Mechanically, the work done by the capillary (which comprises surface tension) and pressure force is minimized. Both approaches arrive at the pressure difference across the liquid-gas interface as a function of the surface tension and the change in surface area and volume of the interface for an incremental deformation. The thermodynamic equation is derived in Carey [24] and the mechanics equation is derived in de Gennes [25]; the resulting general Laplace equation from both approaches is

$$P_I - P_{II} = \sigma \frac{dA_{int}}{dV_{int}} \quad (\text{A.1})$$

where P is the pressure and the subscripts I and II designate the bulk liquid and gas phases, respectively, on each side of the interface as depicted in Fig. A.1. The surface tension, σ , is that of the liquid and gas and the derivatives of the interface area and volume, dA_{int} and dV_{int} , respectively, depend on the shape of the interface.

The geometry of the meniscus needs to be mathematically described to calculate the area and volume change due to a deflection as indicated by the fractional term in Eq. (A.1). Assuming the pore is cylindrical, a semi-spherical interface is used. Carey [24] notes that this interface geometry assumption is valid when the capillary

length is much greater than the pore radius as described in section 2.2.1. Therefore, the area and volume derivatives shown in Eq. (A.1) describe a sphere and the Laplace equation simplifies to

$$P_I - P_{II} = \sigma \frac{2}{R} \quad (\text{A.2})$$

where R is the radius of the sphere containing bulk fluid I as seen in Fig. A.1. As visualized in Fig. A.1, the trigonometric relationship between R and r_p is

$$R = \frac{r_p}{\cos(\theta - 90^\circ)} \quad (\text{A.3})$$

Substituting the trigonometric relation for R , Eq. (A.3), into Eq. (A.2) yields the

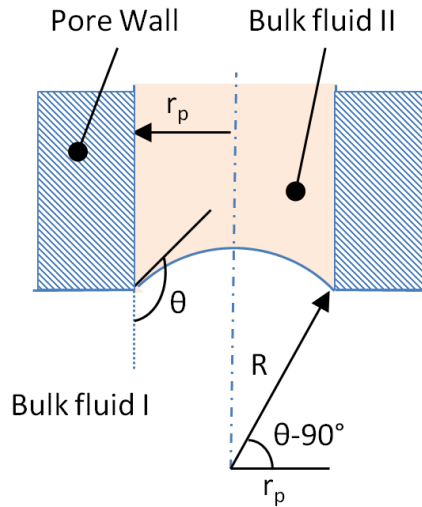


Figure A.1: Sketch of meniscus geometry consistent with the assumption applied to Eq. (A.2)

LEP equation

$$P_I - P_{II} = \frac{2\sigma \cos(\theta - 90^\circ)}{r_p} \quad (\text{A.4})$$

which is rearranged to the final form of the LEP equation, Eq. (2.2).

Appendix B – Estimated Liquid-vapor Contact Angle

The critical surface tension of PTFE is reported to be 0.018 N/m [24] based on multiple fluid measurements. Using this value and a measured contact angle of a liquid drop in air at room temperature, the equilibrium contact angle (that of the same solid but as a flat surface) can be calculated. When the equilibrium contact angle is calculated with this value, it is approximately 90° when it is published to be 108° [24]. This is likely due to the fact that the room temperature water does not meet the dispersion-dominated interaction potential assumptions described in section 2.2.2. Despite this, Carey [24] notes that the adsorption equation is used to derive Eq. (B.1) and it is reasonably accurate when either the solid or the liquid is non-polar. PTFE is a non-polar solid because the carbon chains are surrounded by fluorine whose charges cancel each other out [50]. Since a 90° contact angle on PTFE is not representative of the actual behavior, as a rough estimation, the critical surface tension, $\sigma_{sg,d}$ is calculated when $\theta_{int} = 108^\circ$ to provide an estimate for the critical surface tension of PTFE with a *polar* liquid such as water to produce an accurate contact angle. With this calculation, the “polar” critical surface tension decreases to about half that of the critical surface tension based on non-polar liquids (0.018 N/m), assuming the same dipole-dominant equation,

$$\cos\theta_{int} = 2 \left(\frac{\sigma_{sg,d}}{\sigma_{lg}} \right)^{1/2} - 1 \quad (\text{B.1})$$

can be used to predict the wetting condition when the liquid-gas surface tension, σ_{lg} , is greater than the critical surface tension of the solid, $\sigma_{sg,d}$.

With the equilibrium contact angle for water-air-PTFE now as expected at 108° , the equilibrium contact angle of 100° water-vapor-PTFE can be estimated with Eq. (B.1). The equilibrium contact angle decreases to 103.4° , because the surface tension of saturated liquid-vapor is lower than room temperature liquid-air. With the equilibrium contact angle of liquid-vapor estimated, the contact angle, θ , on the rough membrane can be estimated using the form of the Cassie-Baxter model which applies to intrinsically hydrophobic surfaces because there is gas in the pores

$$\cos\theta = 1 - \Phi_s(1 + \cos\theta_{int}) \quad (\text{B.2})$$

where Φ_s is the fraction of solid under the liquid. Again, if the pores were filled with liquid, the Wenzel equation would be applied to estimate the contact angle.

Since both the intrinsic and actual (apparent) contact angles are known for liquid-air, the only unknown in the equation is the fraction of the liquid in contact with the solid at the membrane-liquid interface Φ_s . This variable is calculated to be 0.43 which means the liquid is in contact with air over 57% of the membrane area - this is consistent with the membrane's porosity with the volume of the void (air) being 55% of the total membrane volume. Using the calculated solid fraction in contact with the liquid, the apparent contact angle of the liquid-vapor at 100°C is calculated to be 131.9° , which is 2% lower than the liquid-air contact angle at 27°C .

Appendix C – Two-phase Effective Extraction Area

The area available for gas flow needs to be scaled when two-phase mixtures are in contact with the membrane. A scaling parameter Φ_m accounting for the area of the membrane in contact with the gaseous phase only is multiplied by the total area available for extraction to make more accurate predictions with the dusty gas model. This area correction parameter is a function of the volume of gas in the plenum as well as the shape and behavior of the gas volume. In the case of the bubbles in the experiments here, it is assumed that the shape of the gas volumes are spherical as seen in Fig. C.1, the bubbles do not deform and the velocity is constant.

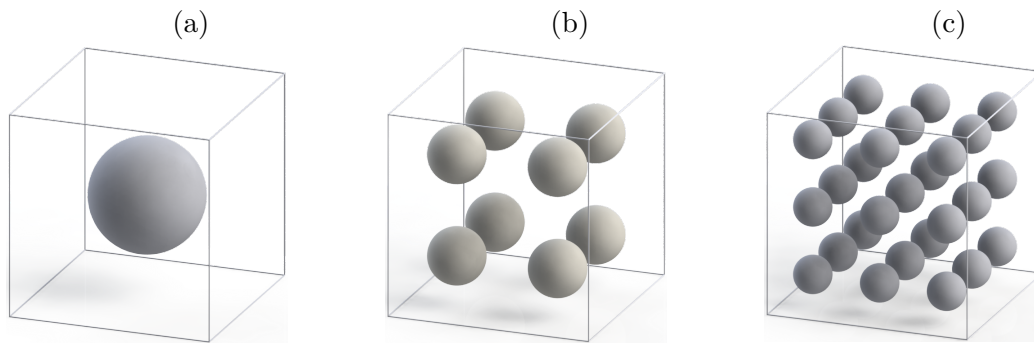


Figure C.1: Spherical bubbles (grey) arranged in a cubic unit control volume of liquid representing a 9% void fraction, bubbles are equally spaced in a $i \times i \times i$ grid where i is (a) 1 (b) 2 and (c) 3

The control volume is chosen to be a cube with sides one unit in length for simplicity. The radius of the bubbles, r_b , is defined by the number of bubbles in the unit cube, $N_b = i^3$, and the void fraction, α :

$$r_b = \left(\frac{3\alpha}{4\pi N_b} \right)^{1/3} \quad (\text{C.1})$$

To determine the area of gas in contact with the membrane as the bubble moves from the bottom of the control volume (CV) to the top of the CV, the circular cross-section area of the bubble (see Fig. C.2) must be integrated through the height of the bubble. The bottom of the CV is -0.5 and the top is 0.5 as shown in Fig. C.3.

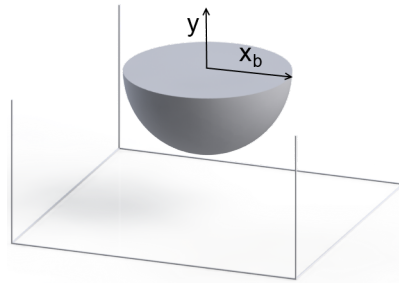


Figure C.2: Cross-section area (πx_b^2) of a spherical bubble with radius r_b

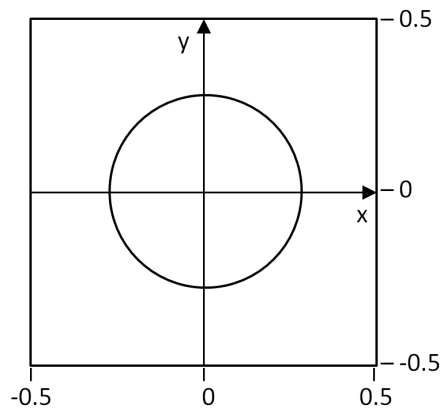


Figure C.3: Coordinate system used to integrate the cross-section area of a bubble as it passes through a horizontal plane perpendicular to the page

To integrate the bubble cross-section area, the bubble is “sliced” at a specified

y-location as shown in Fig. C.4, where the membrane is the cross-section plane. The

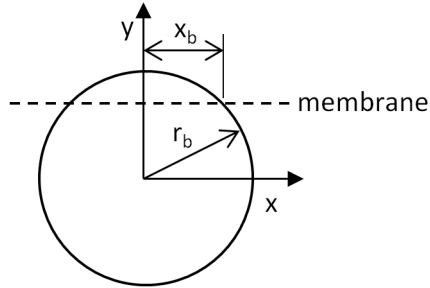


Figure C.4: 2D representation of variables used to integrate the cross-section area of a bubble as it passes through a horizontal plane perpendicular to the page, $r_b^2 = x_b^2 + y^2$

area of the cross-section at the membrane is described by

$$A_{ext} = \pi x_b^2 = \pi(r_b^2 - y^2) \quad (\text{C.2})$$

where x_b is the radius of the circle in the cross-section (in contact with the membrane) at the height, y , as determined by the equation of a circle centered at the origin with a constant, known bubble radius, r_b .

As the spherical bubble passes through the membrane, the average gas area in contact with the membrane is determined by integrating the cross-section area through the height of the CV then dividing by this height. This integral is written as

$$\bar{A}_{ext} = \frac{\pi \int_{-0.5}^{0.5} (r_b^2 - y^2)}{1 \text{ unit}} \quad (\text{C.3})$$

Integrating gives the average area of gas in contact with the membrane:

$$\bar{A}_{ext} = \frac{\frac{4}{3}\pi r_b^3}{1 \text{ unit}} \quad (\text{C.4})$$

and when the bubble radius is written in terms of the void fraction, α , the average gas-membrane contact area is

$$\bar{A}_{ext} = \frac{4}{3}\pi\left(\frac{3\alpha}{4\pi}\right) = \alpha \text{ unit}^2 \quad (\text{C.5})$$

Eq. (C.5) provides an estimate for the average area of gas in contact with the membrane in a cubic CV. To apply this average extraction area to a real system, the ratio of average extraction area to total membrane area is calculated to determine an area correction parameter. Since the membrane area in the unit cube is 1 unit^2 , the units of Eq. (C.5) cancel and the area correction parameter is defined as the void fraction. This correction parameter can now be multiplied by the membrane area of a real system to approximate the average area available for extraction:

$$A_{ext} = \Phi_m A_{mem} = \alpha A_{mem} \quad (\text{C.6})$$

For a 9% void fraction, the bubble radius is 0.278 units as shown in Fig. C.5a and the resulting average radius for gas extraction is 0.095 units as shown in Fig. C.5b.

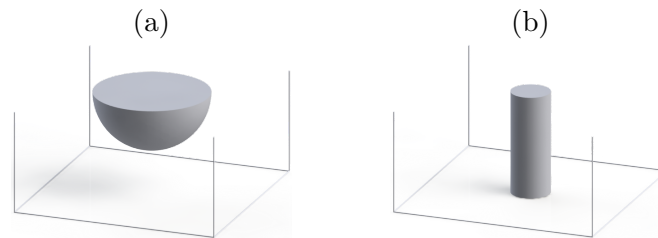


Figure C.5: Sketches of a 9% void fraction unit cube sliced at half the height, showing (a) a spherical bubble and (b) the equivalent average extraction area

Appendix D – Uncertainty

Either the Kline-McClintock (K-M) or the perturbation method of uncertainty is used to determine the error bars on the plotted data points. The majority of the uncertainty calculations were performed with the K-M method. As an example of a K-M uncertainty calculation, the vapor generation equation is analyzed. The equation to determine the amount of vapor generated as a result of boiling is

$$\dot{m}_{gen} = x\dot{m}_{in} \quad (\text{D.1})$$

where \dot{m}_{in} is the liquid mass flow rate supplied to the inlet plenum, which is the control volume (CV) for the following equations, and x is the quality. The quality is determined with

$$x = \frac{h_{out} - h_{f,sat}}{h_{fg,sat}} \quad (\text{D.2})$$

where h_{out} is the enthalpy of the fluid leaving the CV, $h_{f,sat}$ is the enthalpy of the liquid saturation temperature and $h_{fg,sat}$ is the difference in enthalpy of the liquid and gas at saturation temperature. The enthalpy leaving the CV is determined with an energy balance

$$h_{out} = \frac{\dot{m}_{in}h_{f,in} + Q_{in}}{\dot{m}_{out}} \quad (\text{D.3})$$

where $h_{f,in}$ is the enthalpy of the subcooled liquid entering the CV, Q_{in} is the heat supplied to the boiling surface and \dot{m}_{out} is the mass flow rate of liquid and gas leaving

the CV. Conservation of mass gives

$$\dot{m}_{out} = \dot{m}_{in} \quad (D.4)$$

With the above equations, the pressure and temperature are enough to calculate the enthalpies at each state. The heat supplied to the CV is determined by multiplying the nodal-corrected heat flux by the area of the heater block's wall, so the uncertainty in the heat flux and area need to be accounted for as will be shown. To calculate the uncertainty in the vapor generation, Eq. (D.3) is first considered. The partial derivative of each term on the right hand side of the equation must be taken and root sum squared, this yields

$$U_{h_{out}}^2 = \left[U_{\dot{m}_{in}} \frac{h_{f,in}}{\dot{m}_{out}} \right]^2 + \left[U_{h_{f,in}} \frac{\dot{m}_{in}}{\dot{m}_{out}} \right]^2 + \left[U_{Q_{in}} \frac{1}{\dot{m}_{out}} \right]^2 + \left[U_{\dot{m}_{out}} \frac{-\dot{m}_{in}h_{f,in} + Q_{in}}{\dot{m}_{out}^2} \right]^2 \quad (D.5)$$

The uncertainty in the heat supplied is

$$U_{Q_{in}}^2 = [U_{q''}A]^2 + [U_A q'']^2 \quad (D.6)$$

The uncertainty in heat flux is calculated from the 1-D conduction equation

$$q'' = \frac{k(T_1 - T_2)}{\delta_{TC}} \quad (D.7)$$

and therefore the uncertainty is

$$U_{q''}^2 = \left[U_k \frac{(T_1 - T_2)}{\delta_{TC}} \right]^2 + \left[U_{T_1} \frac{k}{\delta_{TC}} \right]^2 + \left[U_{T_2} \frac{-k}{\delta_{TC}} \right]^2 + \left[U_{\delta_{TC}} \frac{-k(T_1 - T_2)}{\delta_{TC}^2} \right]^2 \quad (\text{D.8})$$

Now all of the uncertainties are known for the uncertainty in the quality, Eq. (D.2),

$$U_x^2 = \left[U_{h_{out}} \frac{1}{h_{fg,sat}} \right]^2 + \left[U_{h_{f,sat}} \frac{-1}{h_{fg,sat}} \right]^2 + \left[U_{h_{fg,sat}} \frac{-h_{out} + h_{f,sat}}{h_{fg,sat}^2} \right]^2 \quad (\text{D.9})$$

With all of the uncertainties known for the generated vapor, Eq. (D.1), the final uncertainty of generated vapor is determined with

$$U_{\dot{m}_{gen}}^2 = [U_{\dot{m}_{in}} x]^2 + [U_x \dot{m}_{in}]^2 \quad (\text{D.10})$$

which depends on Eq. (D.9) and the uncertainty of the inlet mass flow rate transducer. Eq. (D.9) depends on Eq. (D.5) which subsequently depends on Eqs. (D.6) and (D.8).

To quantify the goodness of fit of the curve fits and non-dimensional equations, the mean absolute error is used. This is used instead of the root mean squared error to make comprehending the error more natural [51]. The mean absolute error is a sum of the residuals, $y_i - \hat{y}_i$, divided by the total number of data points, n :

$$MAE = \frac{\sum_{i=1}^n (y_i - \hat{y}_i)}{n} \quad (\text{D.11})$$

where y_i is the raw data point and \hat{y}_i is the estimated curve fit data point for the

same x-value as y_i . The non-dimensional form to provide percent uncertainty is

$$MAE\% = \frac{\sum_{i=1}^n \left(\frac{y_i - \hat{y}_i}{y_i} \right)}{n} \quad (\text{D.12})$$

When presenting the average bubble diameter or contact angle, a tolerance follows the value. This tolerance is the uncertainty of the means:

$$U_m = t_{\nu, P} S_{\bar{x}} \text{ where } S_{\bar{x}} = \frac{S_x}{\sqrt{n}} \quad (\text{D.13})$$

where ν is the number of degrees of freedom, $t_{\nu, P}$ is the student-t score (a function of the degrees of freedom and confidence level, P) and S_x is the standard deviation.

Appendix E – List of Equipment

- Extracted vapor scale: Scientech SP350
- Hot Oil Bath: Thermo Electron Corporation, NESLAB EX7 Heating Bath
- Flow meters
 - Mass flow meter: Micro Motion Model CMF010M323NABUEZZZ
 - Volume flow meters
 - * Transducer
 - Alphagaz 1-500 SCCM Air side-trak 500 psi max (no documentation found), serial number 3392
 - * Rotameters
 - Gilmont M099, glass ball: 3-320 mL/min (from Gilmont F6500 Kit)
 - Matheson G603, glass ball: 140-2560 mL/min
 - Aalborg 044-40, glass bead: 791-23,742 mL/min
- Filters
 - Water
 - * Swagelock stainless steel 15 μm
 - * Keystone Polypropylene 0.2 μm canister filter

- Air
 - * RTi 60 SCFM Eliminator SS cotton reinforced fiber; metal bowl with float drain
 - * Motor Guard M-30 0.01 μm filter
- Desiccant (Air)
 - * Available air: Wilkerson 837137 1/4 in NPT
 - * Extraction: Drierite indicating $CaSO_4$ packed in an Alltech porous media tube
- Membrane
 - PTFE0453005 PTFE laminated Membrane, .45 micron pore, 300mm x 300mm sheet, Pack of 5 (Sterlitech)
 - Membrane support
 - * “Super-small-particle filtering” stainless steel porous disc 3/4 in diameter X 1/16 in thickness 10 micron, packs of 4 (McMaster-Carr)
- Venturi vacuum generator: Vaccon 100-ST4
- Inlet gear pump
 - Head: Micropump Model GB-P25.JVS.A.B1
 - Drive: Cole-Parmer Model 75211-10
- Autotransformer: 120VAC Brushed Autotransformer
- Oscilloscope: Tektronix THS720P

- Voltage probe: Tektronix P5200
- Current probe: Tektronix A621 (hall effect sensor, not recommended for currents under 1A even though capable of measuring)
- DAQ boards
 - Pressure transducers: PCI-MIO-16E-4
 - * Connector block: NI SCB-68
 - Thermocouple and flow rate sensors: PCI-6034E
 - * Connector block: NI SCB-68
- Computers
 - Computer 1: Dell Optiplex 745
 - Computer 2: Dell Optiplex GX280
- Degasser: 10 gallon 120VAC GE Hot Water Heater Model GE10P06SAG
- High Speed Camera: Phantom V5.0
 - Lens: AF Micro Nikkor 60mm 1:2.8 D
- State Sensors
 - Pressure Transducers
 - * Pre-extraction (liquid-air only): Omega PX312-030AV
 - * Extraction: Omega PX212-030AV
 - * Outlet: Omega PX212-030AV
 - * Inlet: Omega PX409-030AV

- Thermocouples
 - * Omega TMTSS-062G-6 (T-type sheathed, grounded)
- Relative humidity
 - * Pace Scientific TRH-100
- Calibration equipment
 - Pressure
 - * National Institute of Standards and Technology (NIST) hand-held digital standard
 - Volume flow rate
 - * Cole-Parmer 74900 Series Syringe Pump
 - * Alltech Digital Flow Check HR

Appendix F – Calibration

This section presents the methods of calibration for the sensors. The rotameters come with factory calibrations, typically $\pm 5\%$, and are checked with a syringe pump or the Alltech digital flow checker. The mass flow meters are factory calibrated and output the calibrated flow rate. Pressure transducers are calibrated in-house with a hand-held digital NIST standard. Thermocouples are calibrated with two-point calibration (boiling, freezing), because expected temperatures are close to those two values. The relative humidity sensors come factory calibrated but are checked with salt solutions. The high speed camera must be user-calibrated and depends on the desired measurements - here, the membrane grid is used for calibration.

F.1 Pressure Transducers

All pressure transducers were calibrated at the same time using both compressed air and a vacuum. The transducers and NIST standard are threaded into a tapped block. Uncertainties seen in Table F.1 are from the root sum square of the NIST uncertainty and the standard error of the calibrating curve fit. The equation for the pressure transducer curve fits is

$$P \text{ (kPa)} = mV_{\text{signal}} + b \tag{F.1}$$

where the signal voltage varies with pressure and is from 0-100 mV for these models.

Table F.1: Pressure transducer calibration curves

	m	b	U_{cal} (kPa)	Omega Model	Serial Number
Inlet	2071.99	-0.59	0.384	PX409-030AV	402108
Outlet	2069.05	0.20	0.478	PX212-030AV	R109988
Extraction	2074.45	0.87	0.416	PX212-030AV	S022864
Pre-extraction rotameter	2065.70	0.67	0.473	PX312-030AV	50907

F.2 Thermocouples

All thermocouples are calibrated in boiling distilled water and distilled water with ice cubes. Thermocouples are suspended in the liquid and stirred during calibration. The form of the thermocouple calibration curves is

$$T \text{ (}^\circ\text{C)} = mT+b \quad (\text{F.2})$$

The resulting calibrations are seen in Table F.2.

Table F.2: Thermocouple calibration, $U_{TC}=0.81^\circ\text{C}$ which is the maximum uncertainty in heater block (HB) thermocouple “a” HB_a as seen in Fig. 4.20 when calibrated separately in an oil bath. The calibration of this transducer shown here is that from the two-point calibration to be consistent.

	m	b
Inlet	0.999	-2.016
Extraction	0.997	-1.702
HB_a (on axis, 0.24 cm from wall)	0.993	-1.673
HB_b (on axis, 1.51 cm from wall)	0.995	-1.671
HB_c (off axis, 1.51 cm from wall)	1	-2.138

F.3 High Speed Camera

To calibrate the high speed camera, the grid lines of the membrane are used. Since the distance between ribs, k_{mm} , is 1.08 mm, the pixel-to-length scale can be determined by measuring the distance between ribs along the horizontal. The camera angle, α , must be known relative to the plane of the membrane so the horizontal pixel distance, $l_{1,pivot}$, can be converted to the out of plane length scale, k_{px} . This is accomplished by measuring the apparent angle between the horizontal and the grid lines of the membrane, θ . The equations and the figures they refer to are below, followed by a test image showing and sample calculations resulting in a $\approx 5\%$ calibration uncertainty.

$$l_{1,long} = \cos(\theta)l_{1,pivot} \quad (\text{F.3})$$

$$l_{2,long} = \cos(\theta)l_{1,long} \quad (\text{F.4})$$

$$x_{vertex} = l_{1,pivot} - l_{2,long} \quad (\text{F.5})$$

$$y_{vertex} = \sin(\theta)l_{1,long} \quad (\text{F.6})$$

$$y_{perp.} = \frac{y_{vertex}}{\sin\alpha} \quad (\text{F.7})$$

$$l_{perp.,hyp.} = \sqrt{y_{perp.}^2 + l_{2,long}^2} \quad (\text{F.8})$$

$$\psi = \cos^{-1}\left(\frac{l_{2,long}}{l_{perp.,hyp.}}\right) \quad (\text{F.9})$$

$$k_{px} = \sin(\psi)l_{1,pivot} \quad (\text{F.10})$$

$$mm/px = \frac{k_{mm}}{k_{px}} \quad (\text{F.11})$$

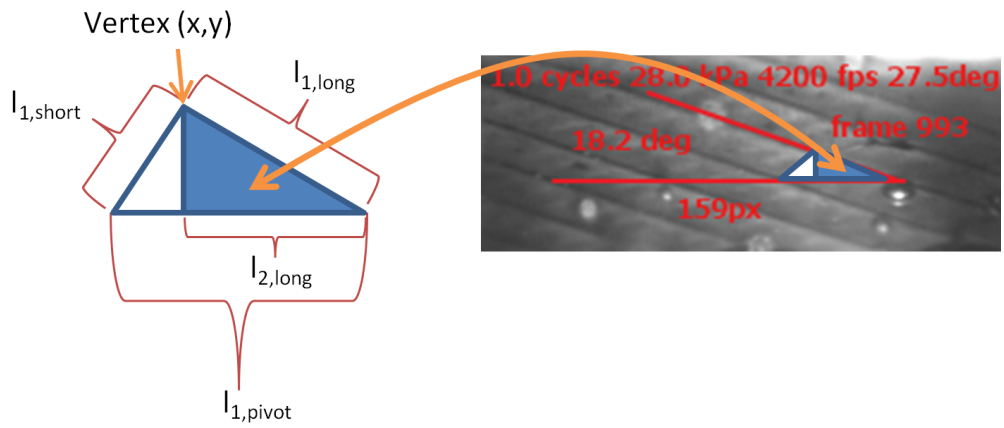


Figure F.1: Geometry and variables for Eq. (F.3) to Eq. (F.11)

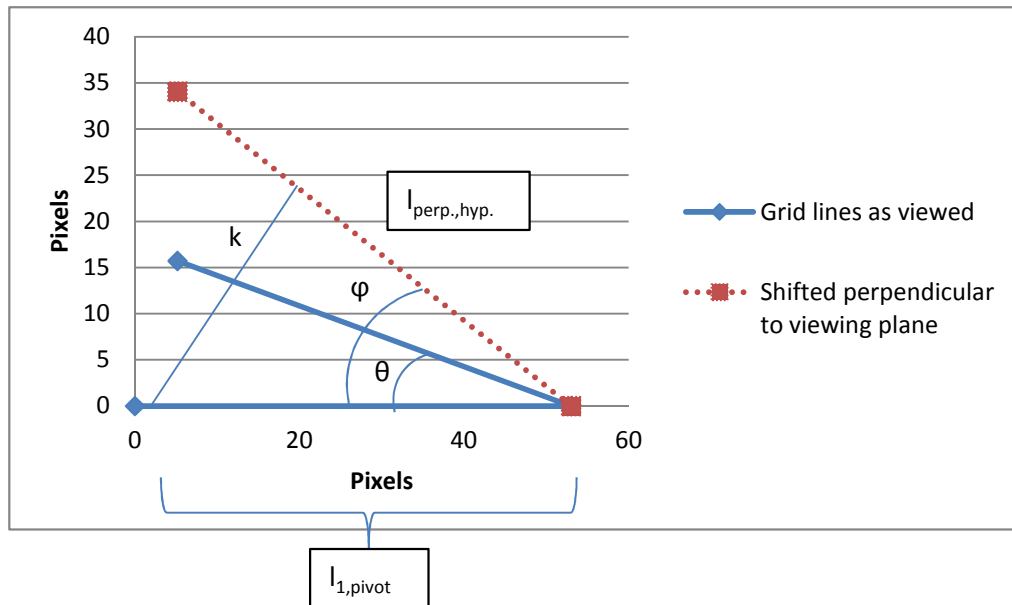


Figure F.2: Pivoting the angled grid lines (membrane ribs) about the horizontal to account for perspective, see Eq. (F.3) to Eq. (F.11)

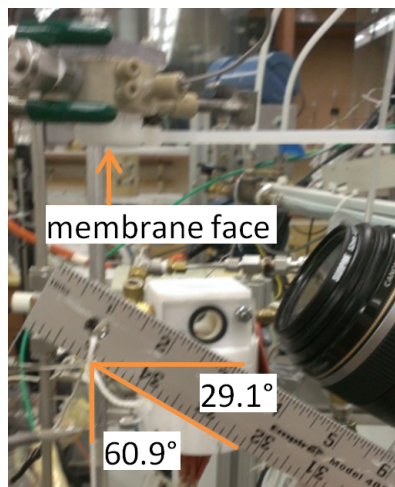


Figure F.3: Measuring the camera angle with reference to horizontal which is parallel to membrane face, this image is for the calibration test

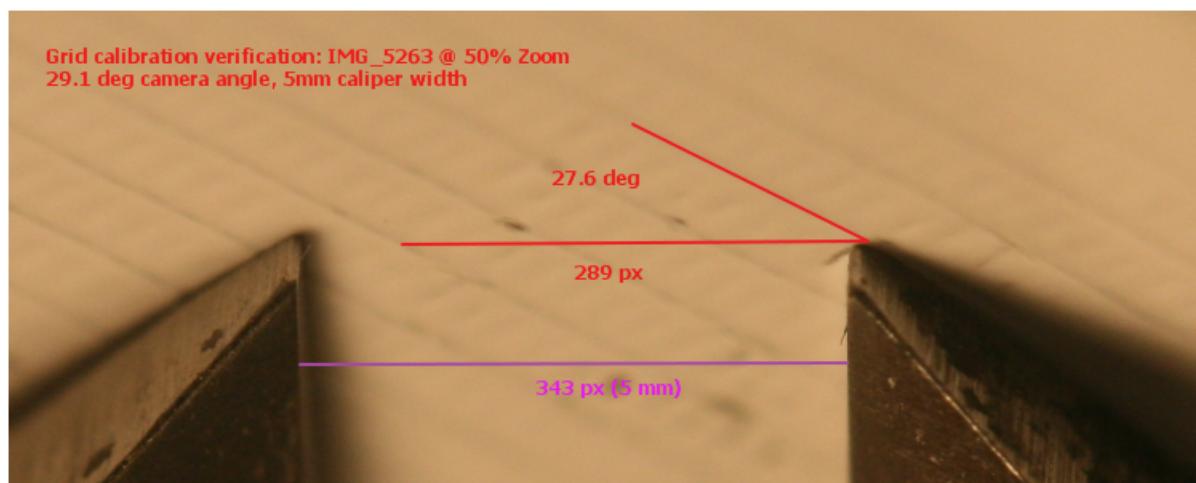


Figure F.4: Test image, camera angle 29.1 degrees

The output calculations from the test image are shown in Table F.3

Table F.3: Test image calculations, camera angle $\alpha = 29.1$ degrees as measured with PicPick’s protractor from Fig. F.3, top three highlighted sections are user input

camera angle α (deg)	29.1
distance between three grids at pivot (px):	289.0
average width between grids at pivot line (px) $l_{1,pivot}$:	96.3
angle of grid line from pivot (deg) θ :	27.6
grid line to vertex (px) $l_{1,long}$:	85.4
long leg of internal triangle (px) $l_{2,long}$:	75.7
(px) x_{vertex}	20.7
(px) y_{vertex}	39.6
(px) $x_{perp.}$	81.3
hypotenuse in perpendicular plane (dotted line) (px) $l_{perp., hyp.}$	111.1
angle of grid in perp. plane (dotted line) (deg) ϕ :	47.1
short leg of perp. triangle (length known) k (px):	70.5
k (mm):	1.08
mm/px:	1.5E-02
VERIFICATION:	
num px:	343.0
calibrated length:	5.2
percent difference	4.6%

F.4 Relative Humidity Sensors

The relative humidity sensors were calibrated by swapping out the mounting plate in a sensor block with one that was tapped with three holes (see “Calibration plate” in appendix G). The inlet and outlet ports were plugged and a three point calibration was performed. The two extreme points were achieved with desiccant (0% RH) and distilled water (100% RH). A salt solution was used for a third point knowing the

relative humidity in a volume at room temperature with some liquid on the salt. Each solution is left in the sealed chamber for at least 5 hours. The solutions used were:

1. $CaSO_4$ desiccant: Humidity of saturated salt solution from Handbook of Chemistry and Physics [34], 75.5 ± 0.1 at $20^\circ C$
2. NaCl dry powder
3. Distilled water

The calibration points shown in Table F.4 verify that for 0-75.5% RH the factory calibrations are indeed within 3%, therefore the coefficients given by the manufacturer were used. The relative humidity sensors were likely too wet to record accurately when in a saturated environment, because even the thermistors were reading incorrect values. When saturated, the “extraction” RH sensor read 100% humidity and $19.2^\circ C$, so it is assumed that as long as the sensing element is not saturated, it reads correctly for the other two RH sensors.

Table F.4: Relative Humidity Calibration Verification

Relative Humidity with Temperature Correction and Given Calibration Curve			
Expected RH	Inlet	Extraction	Pre-extraction rotameter
0	-0.007	-0.007	-0.003
0.755	0.733	0.724	0.745
1	1.097	0.998	1.126

Temperature		
Inlet	Extraction	Pre-extraction rotameter
18.3	18.8	19.5
18.4	18.9	19.5
38.2	19.2	64.6

The coefficients given are applied to the following equations as given by Pace Scientific

$$\%RH_{raw} = \frac{V_{signal}}{V_{in}}(C_{high} - C_{low}) + C_{low} \quad (\text{F.12})$$

where V_{in} is the voltage supplied to the RH sensors (5.05 VDC). The high and low values from the factory calibration were used:

Table F.5: Calibration coefficients as determined by Pace Scientific

Location	C_{low}	C_{high}
Inlet	-31.1	134.8
Extraction	-27.7	132.5
Pre-extraction rotameter	-29.1	137.6

Temperature compensation was performed with

$$\%RH = \frac{\%RH_{raw}}{1.0546 - 0.00216T} \quad (\text{F.13})$$

where T is in Celsius.

F.5 Volume Flow Meters

Rotameters were all read at the center of the spherical float. Humidity was kept low so the float did not stick to the tapered tube it slid in. A syringe pump was used to calibrate the low volume flow rate rotameters (320 mL/min range), but multiple 60 mL syringes have to be used, which results in the plunger sticking to the syringe walls, so slight fluctuations were read by the high precision rotameter. Tubes

leading to the rotameter were wrapped in Teflon[®] tape to twist into the syringes, but this coupling is not very reliable. Nevertheless, the syringe pump calibrates the rotameters to give a curve similar to that supplied by the manufacturer. For the higher flow rate rotameters, manufacturer-supplied curves are used.

The rotameter calibration curves are shown in Table F.6. These coefficients correspond to

$$Q = F_{SV}^2 C_3 + F_{SV} C_2 + C_1 \quad (\text{F.14})$$

where F_{SV} is the float scale value read at the center of the ball and the volume flow rate, Q , is in mL/min.

Table F.6: Rotameter calibration curves for polynomial fit

Rotameter	C_3	C_2	C_1
Gilmont M099	0.0318	0.4856	0
Matheson G603	-0.0474	23.7	70
Aalborg 044-40	0.0	162.9876	-973.449

A digital Alltech NIST traceable flow rate checker (500 mL/min max) is checked against the 320 mL/min range rotameter and proves to be well calibrated. Therefore, this digital checker is used to calibrate the Alphagaz flow rate transducer. This is achieved using compressed air, because it provides a steady flow rate. The Alltech and Alphagaz flow sensors were placed in-line with each other and pressure transducers are upstream of each flow meter for pressure corrections. The pressure drop in all flow meters with a range at or below 500 mL/min were found to have negligible pressure drop, but it was still accounted for.

Since there was no documentation for the Alphagaz transducer, a set of wires on

the “output” channel of the monitor (cable ribbon) producing a varying signal for different flow rates was chosen. A 0-5V signal was searched for but only a $\approx 1-6$ V signal was found, this was used. The resulting curve fit was

$$Q_{Alphagaz} = V_{signal}119.6 - 155.89 \quad (\text{F.15})$$

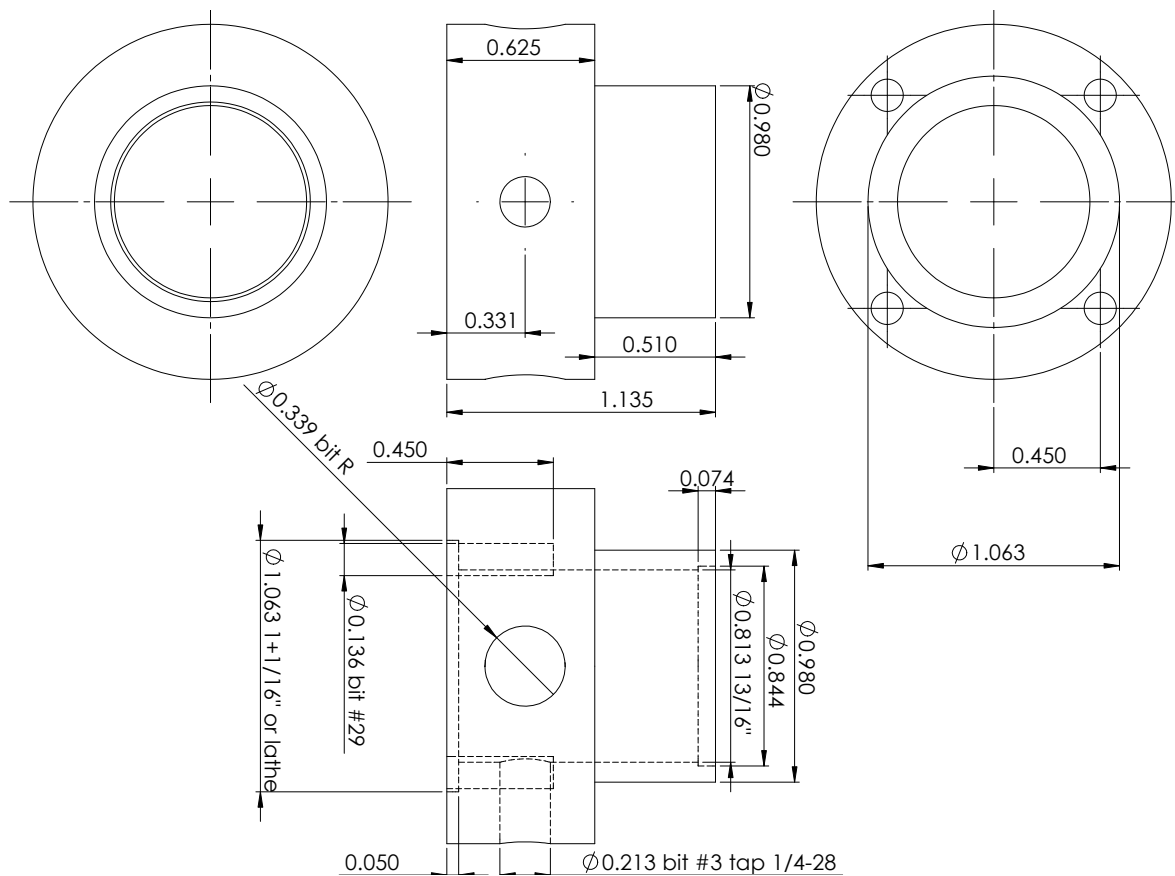
where the volume flow rate, $Q_{Alphagaz}$, is in mL/min and the Alphagaz signal wire potential, V_{signal} , is in volts.

Appendix G – Parts Drawings

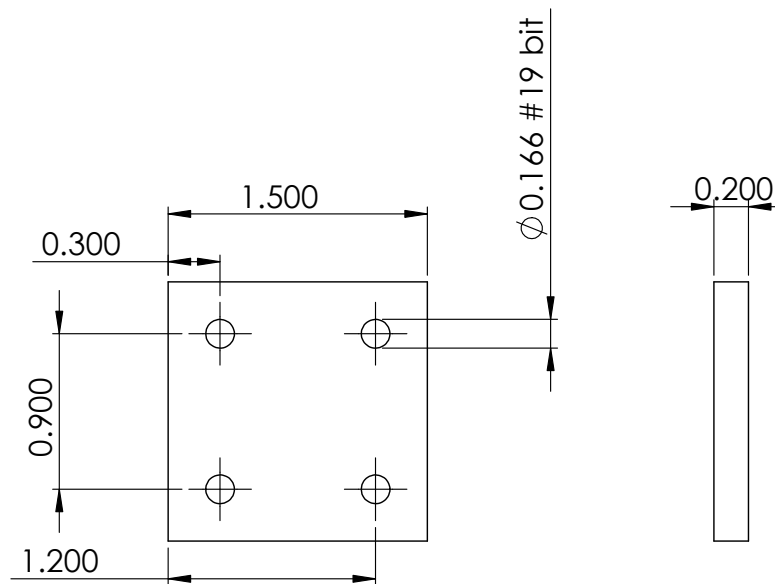
Units of parts drawings are in inches.

Extraction chamber

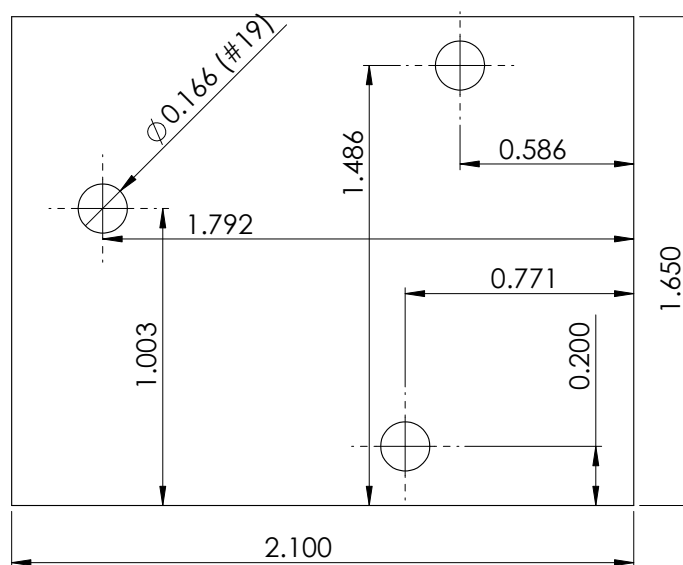
Main body - holes for NiCr heater compression fittings not shown, see single-phase device drawing for 1/4-28 tap callout with seat for compression taper



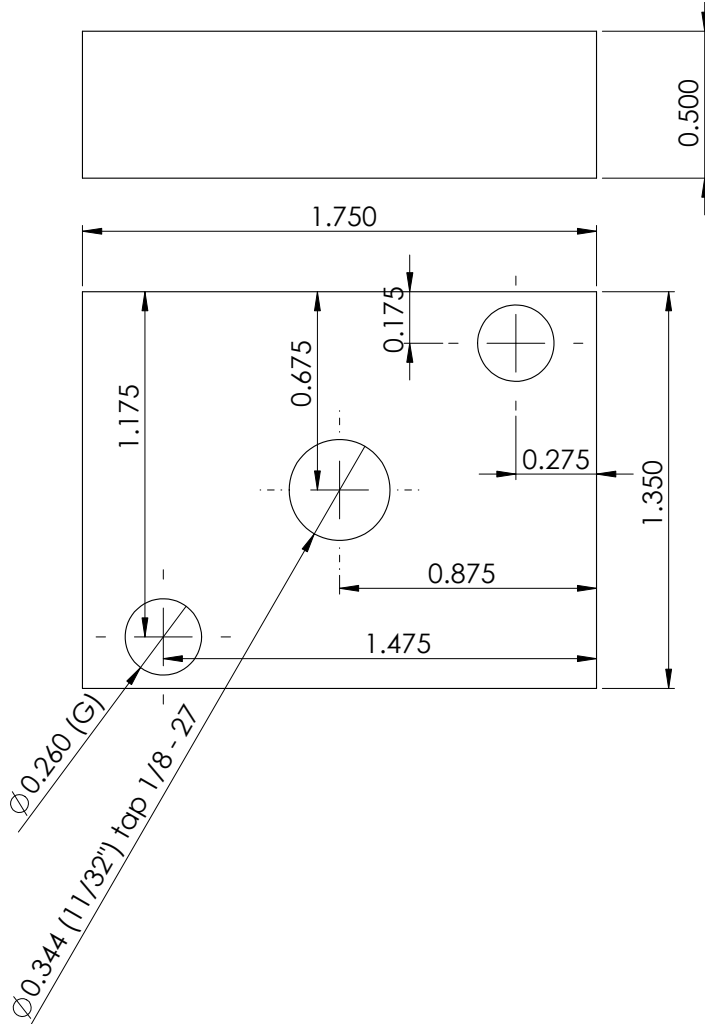
Extraction chamber window

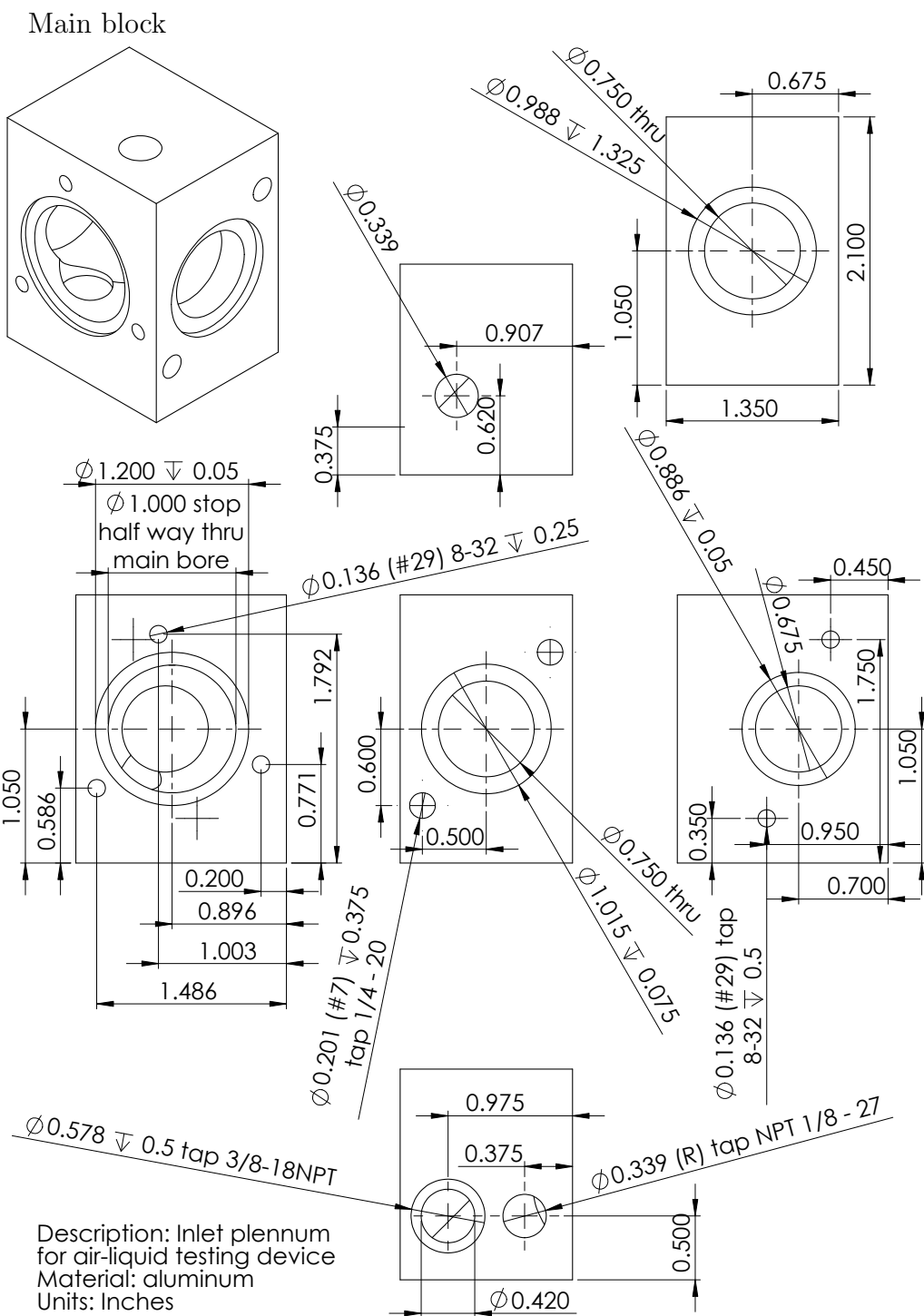
Liquid-air device

Front window



Available air bubbler plate

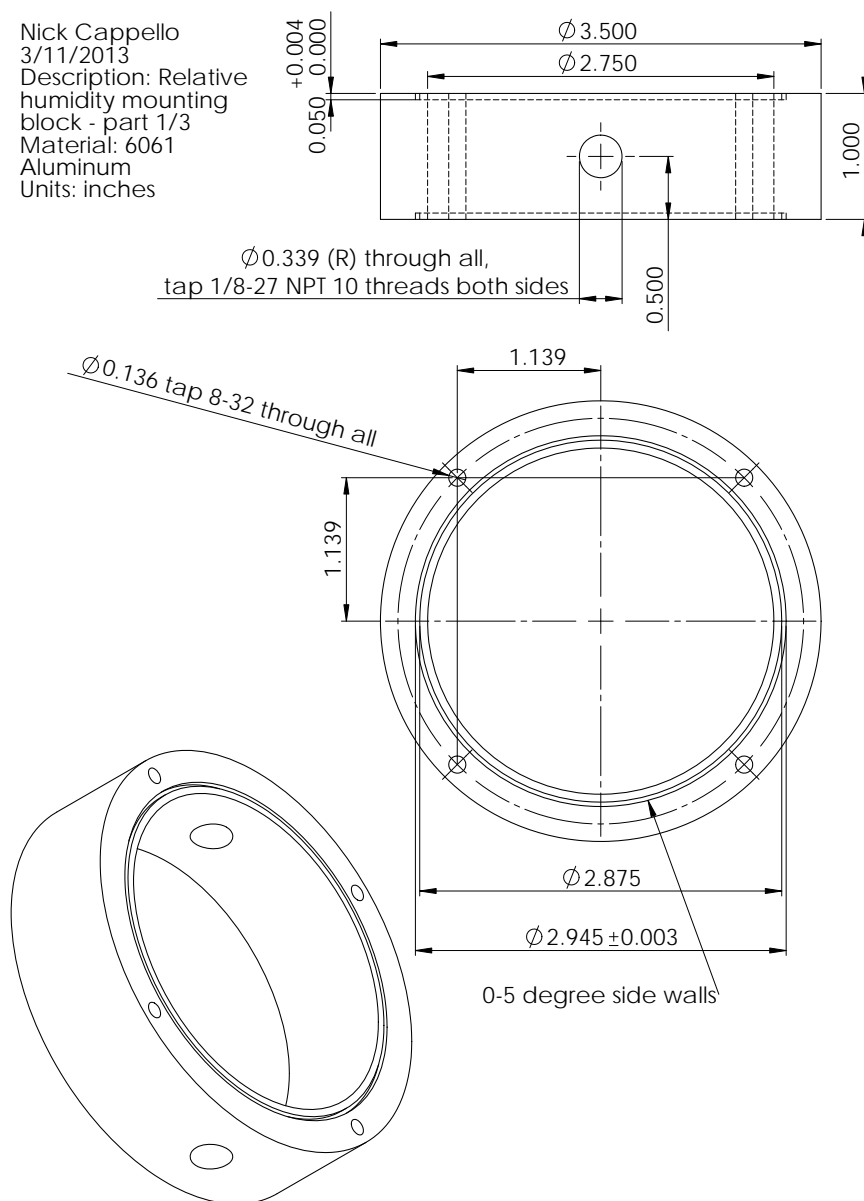




Humidity sensor

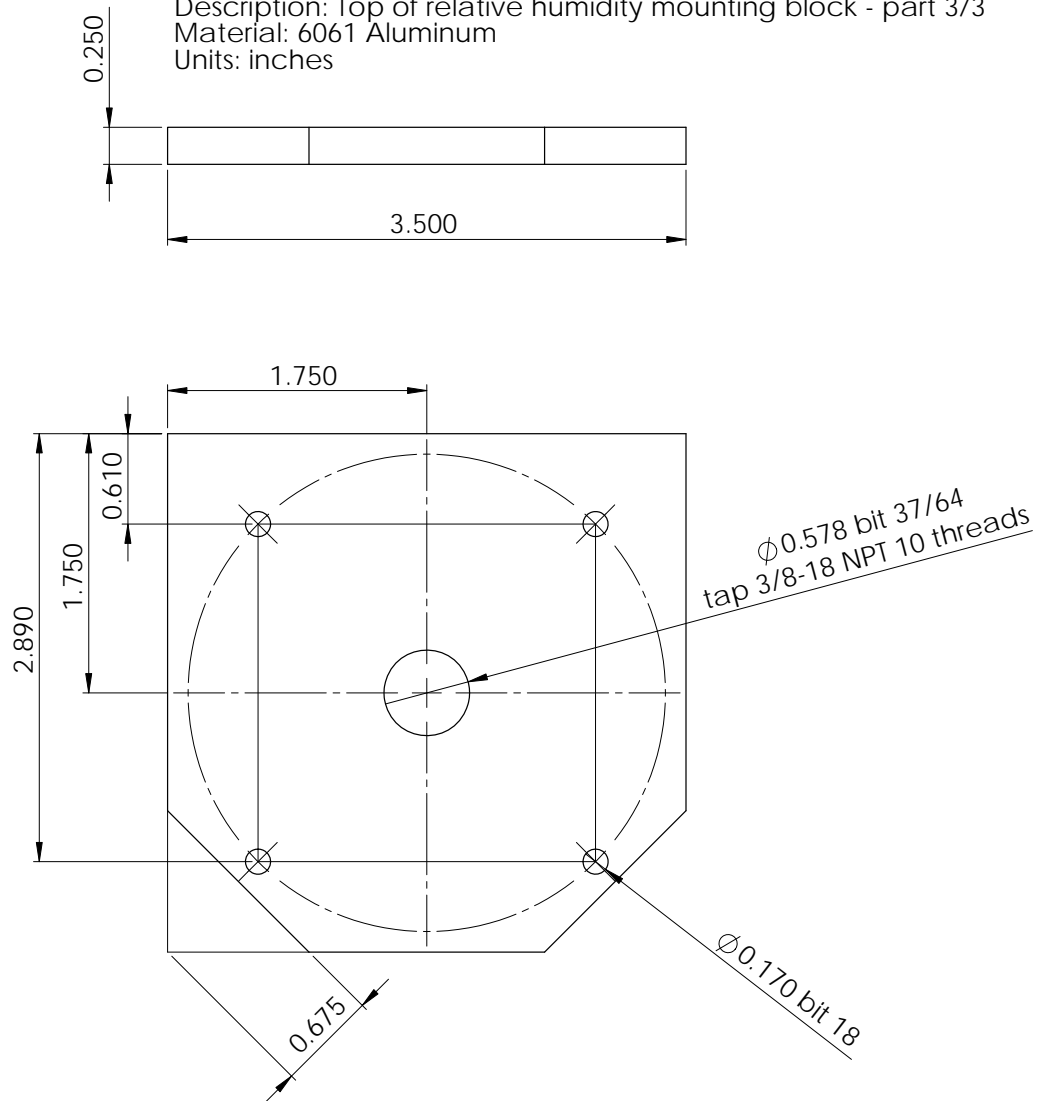
Main body

Nick Cappello
3/11/2013
Description: Relative
humidity mounting
block - part 1/3
Material: 6061
Aluminum
Units: inches



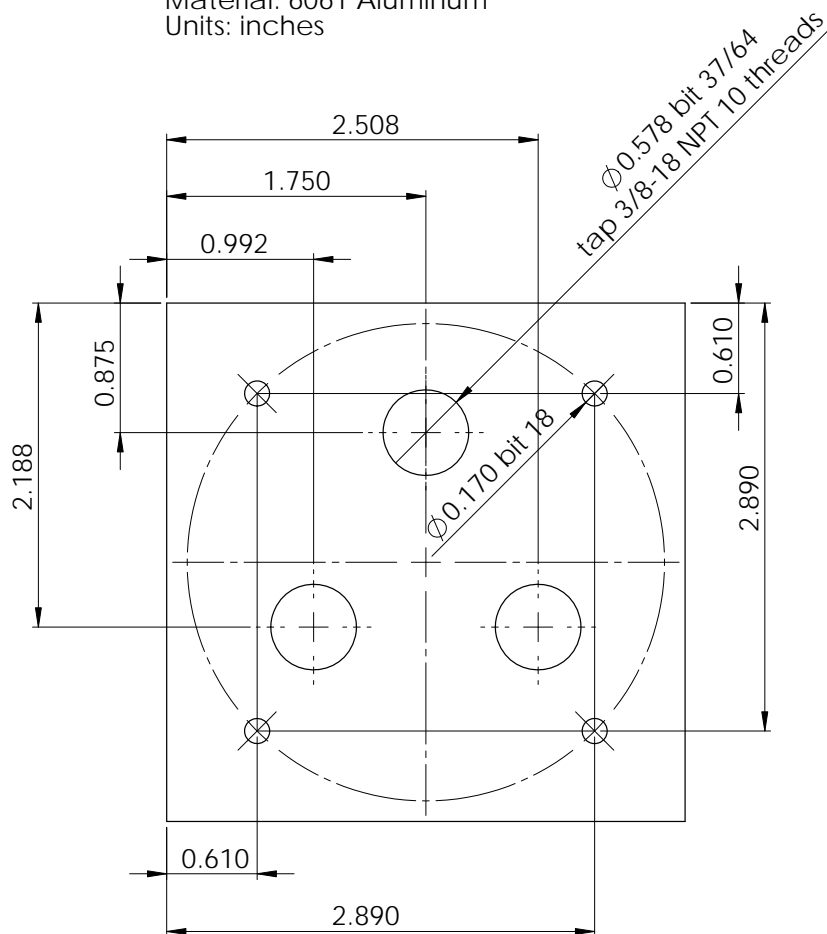
Sensor mounting plate

Description: Top of relative humidity mounting block - part 3/3
Material: 6061 Aluminum
Units: inches



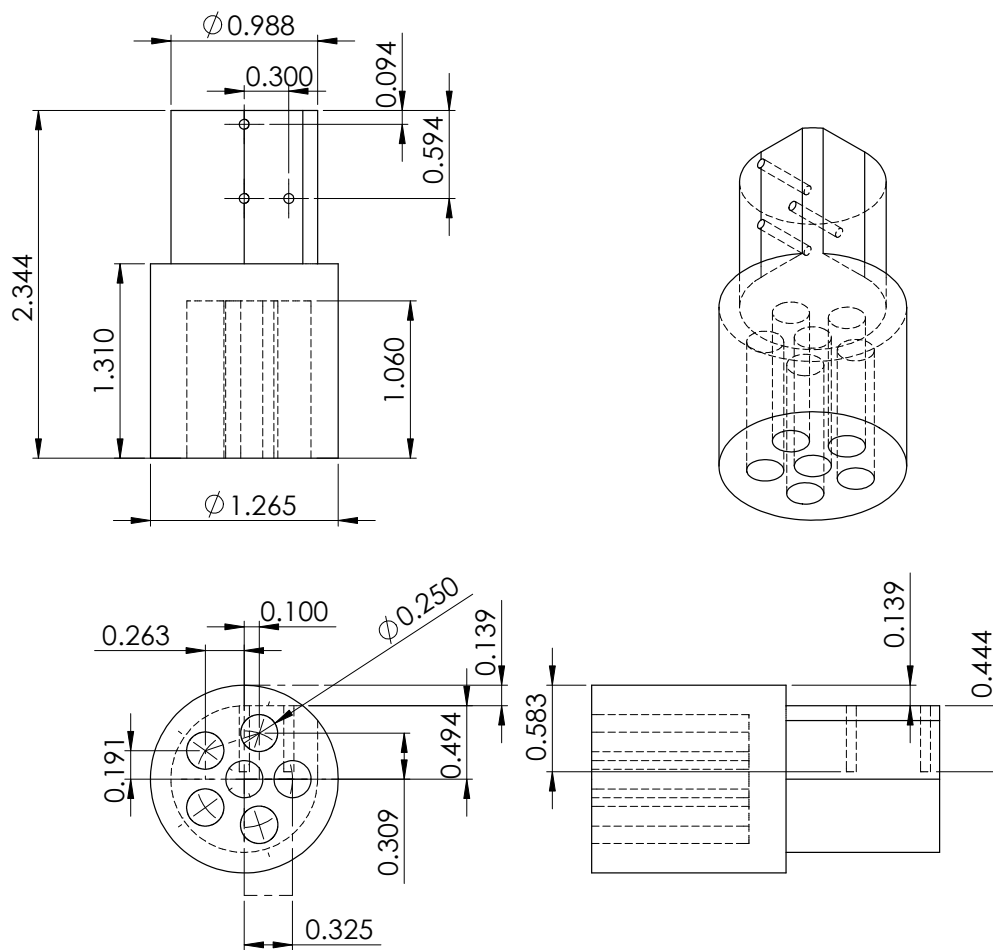
Calibration plate

Description: Calibrating plate for relative humidity sensors, use center tube with capped ports
Material: 6061 Aluminum
Units: inches



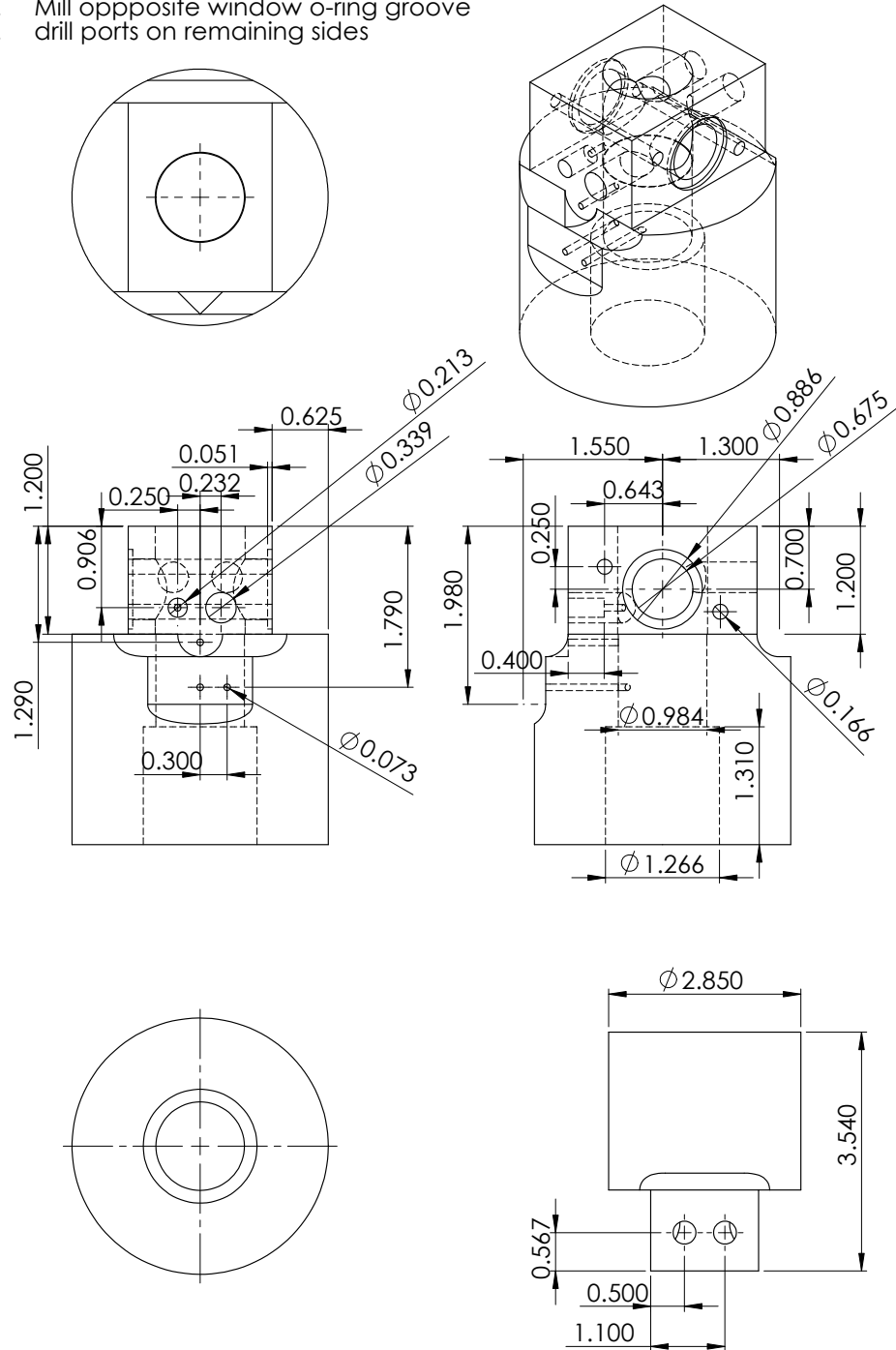
Liquid-vapor device

Heater block (flat is for thermocouple holes, turned round)

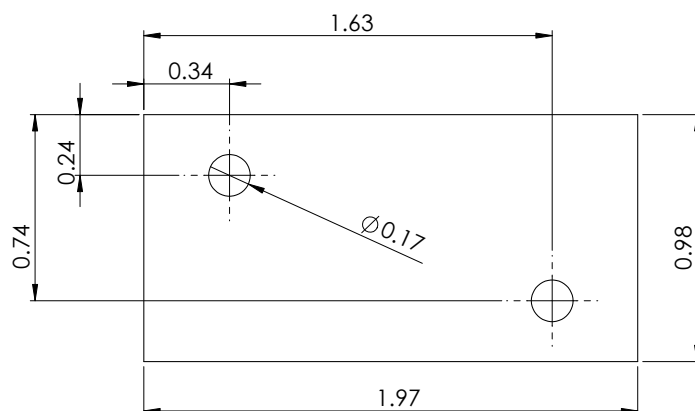


1/15/13 Teflon Permeability Testing Device for Liq/Vap. mixture

1. turn HB housing & precision fit for PEEK
2. On rotary table, mill window side as seen in middle right (1/2" end mill), all holes thru except window o-ring mount
3. Mill opposite window o-ring groove
4. drill ports on remaining sides



Liquid-vapor windows, back window for liquid-air



Single-phase devices

Inlet plenum - compression fitting threads into 1/4-28 hole, diameter of pass-through hole is 3/32 in

